STOKESIAN DYNAMIC SIMULATIONS AND ANALYSES OF INTERFACIAL AND BULK COLLOIDAL FLUIDS

A Dissertation

by

SAMARTHA GUHA ANEKAL

Submitted to the Office of Graduate Studies of
Texas A&M University
in partial fulfillment of the requirements for the degree of

DOCTOR OF PHILOSOPHY

May 2006

Major Subject: Chemical Engineering

STOKESIAN DYNAMIC SIMULATIONS AND ANALYSES OF INTERFACIAL AND BULK COLLOIDAL FLUIDS

A Dissertation

by

SAMARTHA GUHA ANEKAL

Submitted to the Office of Graduate Studies of
Texas A&M University
in partial fulfillment of the requirements for the degree of

DOCTOR OF PHILOSOPHY

Approved by:

Chair of Committee,	Michael A. Bevan
Committee Members,	David M. Ford
	Tahir Cagin
	Paul S. Cremer
Head of Department,	Kenneth R. Hall

May 2006

Major Subject: Chemical Engineering

ABSTRACT

Stokesian Dynamic Simulations and Analyses of

Interfacial and Bulk Colloidal Fluids. (May 2006)

Samartha Guha Anekal, B.E., Mangalore University

Chair of Advisory Committee: Dr. Michael A. Bevan

Understanding dynamics of colloidal dispersions is important for several applications ranging from coatings such as paints to growing colloidal crystals for photonic bandgap materials. The research outlined in this dissertation describes the use of Monte Carlo and Stokesian Dynamic simulations to model colloidal dispersions, and the development of theoretical expressions to quantify and predict dynamics of colloidal dispersions. The emphasis is on accurately modeling conservative, Brownian, and hydrodynamic forces to model dynamics of colloidal dispersions. In addition, we develop theoretical expressions for quantifying self-diffusion in colloids interacting via different particle-particle and particle-wall potentials. Specifically, we have used simulations to quantitatively explain the observation of anomalous attraction between like-charged colloids, develop a new criterion for percolation in attractive colloidal fluids, and validate the use of analytical expressions for quantifying diffusion in interfacial colloidal fluids. The results of this work contribute to understanding dynamics in interfacial and bulk colloidal fluids.

To my parents and my late grandfather

ACKNOWLEDGMENTS

Firstly, I thank Dr. Bevan for playing a central role in my research efforts through his constant input of ideas and attention to detail. The knowledge I have received from him has been broad, ranging from colloidal science to anecdotes on scientists to making slick presentations. Our numerous meetings in particular, have been extremely informative and educational. I have no doubt that a lot of what I have picked up from him will stick with me for a long time to come.

I thank my committee members for being a part of this research effort. In particular, I thank Dr. Ford, for his help during the early stages of this work, and not to mention the several discussions he has so willingly been a part of. He is quite easily one of the best teachers I have ever had, and I have greatly benefited from his classes on Statistical Mechanics.

Research, at any level, is a group effort. I express my gratitude to current and past members of the Bevan research group: Wu, Pradip, Neil, Greg, Richard, Sumit, Shannon, and Todd. It's not always easy being the only simulation person in an experimental group, but they have made me feel right at home. The several discussions we have had over the years have contributed significantly to my development as a researcher.

I cannot miss on out on thanking the wonderful support staff in the department. Towanna, Missy, Ninette, and Valerie, made sure that the only thing I had to worry

about was research. The past four and a half years would not have been as smooth without their help.

I take this opportunity to thank my teachers and peers during my undergraduate days for giving me an excellent platform for graduate school. In particular, I would like to thank Dr. Giridhar Madras, at the Indian Institute of Science, for giving me my first experience of university research.

My parents, in their own right, have been significant contributors to my education. I thank my mom for her enormous patience throughout my early years. I thank my dad for not only being the first person to introduce me to science, but also for constantly reminding me to live life the “scientific way”.

Lastly, I express my gratitude to Asha, a dear friend for almost eight years, who very recently, became my wife. Her confidence and encouragement, ever since my college days, have been invaluable.

TABLE OF CONTENTS

Page

Page

LIST OF FIGURES

FIGURE Page

FIGURE Page

1. INTRODUCTION

1.1. Objectives and Significance

One of the greatest pursuits of nanotechnology is the ability to fabricate large, single-domain colloidal crystals on templates for synthesizing photonic bandgap materials.[1] This involves carefully controlling interactions on the order of the thermal energy, kT. The two parts of this problem include (1) being able to measure and monitor particle-particle and particle-wall potentials, and (2) controlling these interactions to assemble colloids on a patterned substrate. To achieve these two objectives, we require a thorough understanding of the thermodynamics and kinetics of these systems.

Unlike atoms and molecules, colloidal particles experience continuum-level viscous forces, whose effect is to slow down dynamics which frequently results in the formation of kinetically hindered states like glasses and gels. This is the main reason why large-scale manufacturing of colloidal crystals is still mostly fiction. While the thermodynamics of these systems is fairly well known, the dynamics are very poorly understood. Even for the simplest case of isotropic attractive particles, there are several dynamically arrested states such as gels, aggregates, repulsive glasses, and attractive glasses. The ability to accurately model dynamics in these systems is thus critical in designing a process for colloidal assembly. It is therefore useful to develop tools to quantify dynamics in colloidal systems.

This dissertation follows the style of The Journal of Chemical Physics.

The research outlined in this dissertation describes the use of numerical simulations to accurately describe colloidal systems under interacting through colloidal, hydrodynamic, and Brownian forces. These include both traditional Monte Carlo to predict equilibrium behavior, and Stokesian Dynamics[2] simulations to model dynamics. Coupling these simulation techniques with useful equilibrium and dynamic analyses provides valuable information about the system under study. This knowledge can then be used to design and test feasibility of real experiments.

Our objectives in using numerical simulations for modeling colloidal dispersions are broadly two-fold. First, we have used numerical simulations to interpret experimental observations to obtain information about the system under study. Secondly, we have used simulations to predict dynamic behavior of colloids under different conditions. Also falling under the second category is verifying the validity of expressions to quantify dynamics in colloidal dispersions. These tools are being used synergistically with real experiments to gain valuable information on colloidal dynamics.

1.2. Background

Colloidal dispersions are perfect systems for applying so called meso-scale simulation techniques. In meso-scale simulations, the colloidal particles are treated at the particle-level, while the surrounding solvent is treated as a continuum. The fundamental assumption in these systems is that the time for momentum relaxation of the larger particle is negligible compared to the time for change in particle configuration. The theory of Brownian motion developed by Einstein,[3] Smoluchowski,[4,5] Langevin,[6]

Fokker,[7,8] and Planck[9] is thus applicable for these systems. According to the theory of Brownian motion, the frequent collisions of the solvent molecules with the colloidal particles impart a random thermal motion, termed Brownian motion. The colloidal particles are also big enough to be influenced by continuum forces due to the solvent. These are called hydrodynamic interactions, arising due to solvent viscous forces, and are very important in determining the dynamic behavior of colloidal dispersions. Thus, in simulating systems belonging to the colloidal regime, both particle-level and continuum forces have to be considered.[2]

The pioneering work in developing a method for simulating colloidal dispersions was that of Ermak and McCammon,[10] where they started from the Langevin and Fokker-Planck descriptions of the colloidal dispersion and arrived at an expression for time evolution of particle configuration. In this work, the hydrodynamic interactions between particles were treated using approximate functions such as the Oseen[11] and Rotne-Prager[12] tensors. This method, along with other modifications,[13-17] is called as Brownian dynamics, and are only valid for low particle concentrations, due to the incomplete treatment of hydrodynamics.[2]

Bossis and Brady[18] developed a general molecular-dynamics type method for simulating dynamics of hydrodynamically interacting particles. They found that lubrication forces, which operate at small particle-particle separations could only be preserved by a pairwise addition of forces, as opposed to velocities.[18] Durlofsky and Brady[19] developed a method for finite systems, where the hydrodynamic resistance tensor was split into far-field and near-field parts. This was later extended to simulating

infinite systems,[20] using Beenakker's[21] expression for Ewald summation of the Rotne-Prager tensor. The method of Durlofsky and Brady and its extension to infinite systems is known as Stokesian Dynamics,[2] so called because of the use of Stokes's equations for the hydrodynamic interactions. Bossis et al.[22] used Blake's[23] image representation for the Stokeslet of a particle near a plane wall and developed a method of simulating finite systems of particles near a plane wall. Nott and Brady[24] and Singh and Nott[25] developed a formalism for simulating infinite systems near a plane wall by discretizing the wall into an array of touching spheres.

Theoretical expressions for self-diffusion in colloidal dispersions have been reported in literature. Short-time self-diffusion coefficients as a function of the Peclet number calculated using Stokesian Dynamics have been reported in literature.[26] Expressions for the long-time self-diffusion coefficient for concentrated colloidal dispersions based on the short-time self-diffusion coefficient have also been formulated.[27,28]

1.3. Dissertation Outline

This dissertation is organized as follows: Section 2 describes the theory behind Stokesian Dynamics. This is mainly meant to be a review of well-established theoretical methods. Section 3 deals with some of the practical issues of using the Stokesian Dynamics code. Details about variables, subroutines, and adjustable parameters are described in this section. Sections 4-6 contain the results this research work. These sections are (or will be) individually published. Finally, section 7 summarizes the

conclusions of this work and introduces some current and future work related to this dissertation.

Section 4 describes a simulation study of two negatively charged Brownian particles near one or two negatively charged walls, based on earlier experiments reported in literature[29,30]. Using Stokesian Dynamics simulations to accurately capture multi-body hydrodynamic interactions, we were able to fully account for observations of anomalous attraction between charged colloidal particles near a charged surface. We also proposed new experiments where the same effect was observed, and derived effective potentials which quantitatively account for the anomalous observations. By comparing our results to an earlier simulation study,[31] we demonstrate the importance of accurately constructing the multi-body mobility tensor and its gradient.

In Section 5 we describe a new dynamic signature for equilibrium percolation in attractive colloidal fluids. The percolation threshold in attractive colloidal fluids is the only identifiable structural feature in the equilibrium fluid phase and is an important precursor for kinetically arrested states such as gels. Since the percolation threshold does not correspond to a thermodynamic transition, equilibrium distribution functions change smoothly across it. Previous definitions for the percolation threshold are based on a definition of connectedness and clustering of particles, which is arbitrary for particles interacting via continuous attractive potentials. In this section, we show that the percolation threshold corresponds to an abrupt change in the short-time self-diffusion coefficient, D_S^S, which we calculate from equilibrium particle configurations. Since D_S^S is also related to viscoelastic properties, this also offers a physical definition to the

percolation threshold. Our simulation results act as a verification of a previous rheological measurement.[32]

In section 6, we report methods to quantify and predict self-diffusion in concentrated interfacial confined fluids. Expression for self-diffusion in three dimensions which are based on multi-body hydrodynamic interactions, are extended to two dimensions and tested using Monte Carlo and Stokesian Dynamics simulations. This section presents a thorough analysis of self-diffusion in interfacial fluids, and validates the extension of theoretical expressions for self-diffusion to interfacial fluids. This forms a robust test case before using these expressions on experimental data.

2. THEORY

2.1. Synopsis

This section describes the theory behind Stokesian Dynamics, which is the method used in this work for simulating colloidal dispersions. Stokesian Dynamics is a molecular-dynamics type approach for simulating the dynamic behavior of particles dispersed in a fluid. One of the earliest formulation for simulating Brownian particles dispersed in a fluid was developed in the pioneering work of Ermak and Mccammon,[10] who, starting from the Langevin equation of motion for particles experiencing a random force, arrived at a forward-time step equation of motion for Brownian particles. This work, along with other developments is generally called *Brownian Dynamics*. These are valid only in the dilute particle concentration regime, because of incomplete treatment of hydrodynamics. A more general method, incorporating all hydrodynamic interactions, and thus valid for all particle concentrations, was developed by Durlofsky and Brady[19] and Brady and Bossis,[2] which was termed *Stokesian Dynamics*. The following section describes the development of the governing equations of motion for the particles in a fluid medium.

2.2. Particle Equation of Motion

Consider N rigid particles of radius a dispersed in a Newtonian fluid of density ρ and viscosity μ. The fluid velocity is governed by the Navier-Stokes equations for an

incompressible, isotropic fluid, while the equation of motion for the particles are represented by the coupled *N*-body Langevin equation, which can be written as[2,10]

$$\mathbf{m}\cdot\frac{\partial\mathbf{U}}{\partial t}=\mathbf{F}^{H}+\mathbf{F}^{P}+\mathbf{F}^{B} \tag{2.1}$$

where **m** is the mass/moment of inertia tensor of dimension $6N\times6N$, **U** is the particle translational/rotational velocity vector of dimension $6N$, and the force/torque vectors of dimension $6N$ can be broken into three parts: (a) the hydrodynamic forces $\mathbf{F}^{H}$, (b) the deterministic conservative forces $\mathbf{F}^{P}$, and (c) the stochastic Brownian forces, $\mathbf{F}^{B}$. When the motion of the particles is such that the particle Reynolds number is small, the Navier-Stokes equations which describe the motion of the fluid reduce to linear Stokes equations, and the hydrodynamic forces exerted on the particles by a bulk linear shear flow is[2]

$$\mathbf{F}^{H}=-\mathbf{R}_{FU}\cdot\left(\mathbf{U}-\mathbf{U}^{\infty}\right)+\mathbf{R}_{FE}:\mathbf{E}^{\infty} \tag{2.2}$$

Where $\mathbf{U}^{\infty}$ is the bulk shear flow velocity, $\mathbf{E}^{\infty}$ is the symmetric part of the velocity gradient tensor, also called the stresslet, and $\mathbf{R}_{FU}$ and $\mathbf{R}_{FE}$ are the configuration-dependent hydrodynamic resistance tensors which relate the hydrodynamic force/torque on the particles with the particle velocity and stresslets. Under the absence of external shear or bulk flow, eq. (2.2) reduces to

$$\mathbf{F}^{H}=-\mathbf{R}_{FU}\cdot\mathbf{U} \tag{2.3}$$

The deterministic, conservative forces $\mathbf{F}^{P}$ include interparticle and external forces and will be discussed later. The stochastic Brownian force $\mathbf{F}^{B}$ arises due to thermal

fluctuations in the fluid. The statistical properties of the Brownian force are characterized by a mean and variance given by

$$\begin{aligned} \left\langle \mathbf{F}^B \right\rangle &= 0 \\ \left\langle \mathbf{F}^B(0)\mathbf{F}^B(t) \right\rangle &= 2k_B T \mathbf{R}\delta(t) \end{aligned} \tag{2.4}$$

Here, k_B is Boltzmann constant, T is the absolute temperature, and $\delta(t)$ is the Dirac delta function. The angle brackets denote an ensemble average over independent configurations. On the time scale of particle motion, the fluctuating forces can be considered instantaneous. The fluctuation-dissipation theorem requires the Brownian contribution to be weighted by the hydrodynamic resistance tensor as shown in eq. (2.4).

The Langevin equation (eq. (2.1)) is valid provided the configuration of the particles does not change significantly during the time scale of Brownian motion, $\tau = m/6\pi\mu a$, which is also the time scale for momentum relaxation.[2,10] This condition is satisfied for most colloidal dispersions. Under these conditions, eq. (2.1) can be integrated over a time interval Δt, larger than the momentum relaxation time scale τ, but smaller than the time over which the forces change significantly. Integrating eq. (2.1) twice gives the evolution equation for particle configurations as

$$\begin{aligned} \mathbf{r} &= \mathbf{r}^0 + k_B T\left(\nabla\cdot\left(\mathbf{R}^0\right)^{-1}\right)\Delta t + \left(\mathbf{R}^0\right)^{-1}\cdot\mathbf{F}^{P,0}\Delta t + \mathbf{X}^0(\Delta t) \\ \left\langle \mathbf{X}(\Delta t)\right\rangle &= 0, \left\langle \mathbf{X}(\Delta t)\mathbf{X}(\Delta t)\right\rangle = 2\mathbf{R}^{-1}\Delta t \end{aligned} \tag{2.5}$$

where $\mathbf{r}$ is a vector of particle positions, $\mathbf{R}$ is the hydrodynamic resistance tensor, $\mathbf{X}(\Delta t)$ is the Brownian contribution to particle displacements, and the superscript "0" indicates

that each quantity is computed at the beginning of the time interval. Eq. (2.5) can be directly used in dynamic simulations. From a given initial configuration, the particle trajectory can be obtained, provided the conservative forces are specified.

For creeping flow, we recall that the hydrodynamic force, $\mathbf{F}^H$, is linearly related to the particle velocities, through Stokes equations

$$\mathbf{F}^H = -\mathbf{R}(\mathbf{r}) \cdot \mathbf{U} \tag{2.6}$$

where $\mathbf{R}$ is the $3N \times 3N$ resistance tensor that depends only on the instantaneous particle position vector, $\mathbf{r}$, which is of order $3N$. Note that the subscript "*FU*" has been dropped from eq. (2.3) since we are interested only in the force-velocity part of the hydrodynamic resistance tensor. To accurately consider both far-field, multi-body and near-field hydrodynamic interactions in an N particle system, Durlofsky and Brady,[19] and Brady and Bossis,[2] developed a general method to construct the resistance and mobility matrices. In their method, hydrodynamic interactions are separated into a far-field part, which incorporates the multi-body interactions and a near-field lubrication correction. The steps for constructing the resistance tensor, $\mathbf{R}$ are briefly outlined here. However, the reader is referred to the original references[2,19] for a more thorough treatment. The total resistance tensor, $\mathbf{R}$, which incorporates far-field multi-body interactions and near-field lubrication corrections, is calculated as

$$\mathbf{R} = \mathbf{R}^{\infty} + \mathbf{R}_{2B} - \mathbf{R}_{2B}^{\infty} \tag{2.7}$$

The far-field, multi-body hydrodynamic interactions are captured by the first term, $\mathbf{R}^{\infty}$. The far-field resistance tensor is evaluated by inverting a far-field mobility tensor, $\mathbf{M}^{\infty}$ as,

$$\mathbf{R}^{\infty} = \left(\mathbf{M}^{\infty}\right)^{-1} \tag{2.8}$$

Under assumption of Stokes flow, **M** and **R** have some important properties. Both tensors depend only on the instantaneous configuration and not on particle velocities. Also, both tensors are symmetric, as shown by the reciprocal theorem and positive definite, due to the dissipative nature of the system.[19] The construction of these tensors for different cases will be discussed in the following sections.

2.3. Hydrodynamics

Colloidal particles are generally surrounded by a viscous fluid. The behavior of the dispersion is hence strongly influenced by hydrodynamic forces generated by relative motion of the particles and the fluid. They are extremely important in dynamic simulations because of their long-range ($1/r$), and multi-body interactions can be neglected only under very dilute particle concentrations.

2.3.1. Stokes equations

In the dynamic simulation of a colloidal dispersion, the fluid between particles is considered as a continuum and the classical Newtonian laws, *i.e.* the momentum conservation principle, is applied to a stationary control volume through which the fluid passes. A balance yields the familiar momentum transport equation,[33,34]

$$\frac{\partial(\rho\mathbf{u})}{\partial t}+\nabla\cdot(\rho\mathbf{u}\mathbf{u})=\rho\mathbf{g}+\nabla\cdot\boldsymbol{\sigma} \tag{2.9}$$

where ρ is the density of the medium, $\mathbf{u}$ is the fluid velocity, $\mathbf{g}$ is the body force per unit mass due to gravity, and $\boldsymbol{\sigma}$ is the stress tensor. A mass balance across the control volume gives

$$\frac{\partial\rho}{\partial t}+\nabla\cdot(\rho\mathbf{u})=0 \tag{2.10}$$

Under assumptions of constant fluid density, eq. (2.10) reduces to

$$\nabla\cdot\mathbf{u}=0 \tag{2.11}$$

The stress tensor $\boldsymbol{\sigma}$, for a Newtonian fluid can be represented as[33]

$$\boldsymbol{\sigma}=-P\mathbf{I}+\mu\left[\nabla\mathbf{u}+(\nabla\mathbf{u})^{T}\right] \tag{2.12}$$

Where P is the dynamic pressure and $\mathbf{I}$ is the identity tensor. Combining eqs. (2.9), (2.11), and (2.12), writing $p = P + \varphi$, where $\rho\mathbf{g} = -\nabla\varphi$, and assuming constant viscosity, μ, we arrive at,

$$\rho\left(\frac{\partial\mathbf{u}}{\partial t}+\mathbf{u}\cdot\nabla\mathbf{u}\right)=-\nabla p+\mu\nabla^{2}\mathbf{u} \tag{2.13}$$

This is the *Navier-Stokes* equation for describing the conservation of momentum in a continuum fluid. The above equation can be written in a non-dimensional form. Defining characteristic quantities as velocity (U), length (L), time (L/U), and denoting dimensionless quantities by over bars gives,[34]

$$\mathrm{Re}\left(\frac{\partial \bar{\mathbf{u}}}{\partial \bar{t}} + \bar{\mathbf{u}} \cdot \nabla \bar{\mathbf{u}}\right) = -\bar{\nabla} \bar{p} + \bar{\nabla}^2 \bar{\mathbf{u}} \tag{2.14}$$

where

$$\begin{aligned} \bar{p} &\equiv \frac{pL}{\mu U} \\ \mathrm{Re} &\equiv \frac{\rho U L}{\mu} \end{aligned} \tag{2.15}$$

The dimensionless Reynolds number (Re) indicates the relative importance of inertial to viscous forces.

In many problems in colloid science, the Reynolds number is small. Under such circumstances, to a good approximation, the flow is governed by the *Stokes* equations, where the inertial terms in eq. (2.14) are neglected, and the governing equations for fluid motion reduce to

$$\begin{aligned} \nabla \cdot \mathbf{u} &= 0 \\ \nabla p &= \mu \nabla^2 \mathbf{u} \end{aligned} \tag{2.16}$$

The Stokes equations are linear, implying that a solution to a complicated problem can often be arrived at by the superposition of solutions to simpler problems.[34]

The motion of spherical particles in a fluid can be described by the Stokes equations. The velocity at a point on the surface of the sphere, **U**, the force on the sphere **F** and the torque about the sphere center **L**, can be calculated from the equations[34]

$$\mathbf{U} = \mathbf{U_0} + \Omega \times \left(\mathbf{x} - \mathbf{x_0} \right)$$
$$\mathbf{F} = \int_S \sigma \bullet \mathbf{n} \, dS \qquad (2.17)$$
$$\mathbf{L} = \int_S \left(\mathbf{x} - \mathbf{x_0} \right) \times \sigma \bullet \mathbf{n} \, dS$$

Here Ω is the angular velocity of the sphere about its center $\mathbf{x_0}$, S is the sphere surface and $\mathbf{n}$ is the outward positive unit normal. The problem of solving for the velocity $\mathbf{U}$, given the forces and torques, is called the *mobility* problem, while the problem of calculating the forces and torques given the motion of the sphere is called the *resistance* problem.[34]

There are several methods to solve the Stokes equations for spheres moving in a Newtonian fluid. Separation of variables leads to a general solution in which the velocity and pressure fields are represented by spherical harmonics.[35] An alternate approach is to use the solutions of Stokes equations generated by a point force, a force dipole, etc. These solutions are *fundamental* or *singular* solutions. Based on the linearity of the Stokes equations, these solutions can be combined so as to satisfy the boundary conditions of the problem at hand. This approach is widely used in colloid science and is adopted in the Stokesian Dynamics method.

2.3.2. Singular solutions to Stokes equations

One of the most important solutions to the Stokes equation is that which describes the flow caused by a sphere moving due to an applied force **f** through an unbounded quiescent fluid.[34] If the sphere is far away from the source, the velocity and pressure fields are similar to that due to a point force of equal magnitude. Thus the

point-force solution provides a far-field approximation and forms the basis of the superposition method described before.[34]

Using the Dirac delta function to represent the point force, **f**, the singularly forced Stokes equations can be written as

$$\begin{aligned} \nabla \cdot \mathbf{u} &= 0 \\ \nabla p &= \mu \nabla^2 \mathbf{u} + \delta(\mathbf{x})\mathbf{f} \end{aligned} \tag{2.18}$$

Oseen[11] solved the above equations using Green's functions. An alternate solution is by taking advantage of the relation between the Dirac delta function and Fourier transforms.[36] By writing the Fourier representation of the Dirac delta function and solving the singular equations, the solution to the point force problem can be obtained as

$$\mathbf{u}(\mathbf{x}) = \frac{1}{8\pi\mu}\left(\frac{\mathbf{I}}{x} + \frac{\mathbf{xx}}{x^3}\right)\cdot \mathbf{f} \tag{2.19}$$

Where **I** is the identity tensor and $x = |\mathbf{x}|$. The multiplier of **f** in eq. (2.19) is the solution to the singularly forced Stokes equation known by names such as *Stokeslet*, *Green's function*, *fundamental solution*, *propagator function,* and *Oseen tensor*. It is important to note that the derivatives of the Stokeslet are also fundamental solutions to the Stokes equations.

2.3.3. General solutions to creeping flow equations

The creeping flow or Stokes equations can be solved by two methods. The first method involves dividing each particle surface into elements and then resolving the linear system of equations for the force densities subject to the total force and torque

conditions. At close proximities, the number of surface elements required to resolve the singular force distributions becomes large. This becomes computationally expensive and hence impractical for dynamic simulations.

The alternative to describing the flow in terms of a surface distribution of point forces is to describe it in terms of a distribution of higher order singularities. This is the multipole expansion method for solving the Stokes equations. The starting point is the integral representation for the velocity field in Stokes flow, given by[37,38]

$$\mathbf{u}(\mathbf{x}) - \mathbf{u}^{\infty}(\mathbf{x}) = -\frac{1}{8\pi\mu}\int_{S_y} \mathbf{G}(\mathbf{x}-\mathbf{y})\cdot\mathbf{f}(\mathbf{y})\, dS_y \tag{2.20}$$

The integration is performed over **y** and **G** is the Oseen tensor, a Green's function and is given by,

$$\mathbf{G}(\mathbf{x}) = \frac{\mathbf{I}}{x} + \frac{\mathbf{xx}}{x^3} \tag{2.21}$$

f(**y**) is the force density at the point **y** on the surface of the particle and $\mathbf{u}^{\infty}(\mathbf{x})$ is the velocity field in the absence of any particles. Expanding the Green's function in a Taylor series about the center of the particle α,[37]

$$\begin{aligned} G_{ij}(\mathbf{x}-\mathbf{y}) = \sum_{n=0}^{\infty} \frac{(-1)^n}{n!} \left(y_{k_1} - \alpha_{k_1}\right)\left(y_{k_2} - \alpha_{k_2}\right)\cdots \\ \left(y_{k_n} - \alpha_{k_n}\right)\left(\frac{\partial^n G_{ij}(\mathbf{x}-\mathbf{y})}{\partial y_{k_1}\partial y_{k_2}\cdots\partial y_{k_n}}\right)_{y=\alpha} \end{aligned} \tag{2.22}$$

In the above equation, *i, j*, and *k*s are indices representing coordinates. The integer *n* determines the order of the multipole expansion. Using the notation,

$$G_{ij,k_1,k_2,\ldots,k_n}(\mathbf{x}) = \left(\frac{\partial^n G_{ij}(\mathbf{x})}{\partial x_{k_1} \partial x_{k_2} \cdots \partial x_{k_n}} \right) \tag{2.23}$$

and combining eqs. (2.20) and (2.22),

$$\begin{aligned} u_i(\mathbf{x}) - u_i^{\infty}(\mathbf{x}) = & -\frac{1}{8\pi\mu} \sum_{n=0}^{\infty} \frac{(-1)^n}{n!} G_{ij,k_1,k_2,\ldots,k_n}(\mathbf{x}) \\ & \int_{S_y} f_j(\mathbf{y}) \left\{ \left(y_{k_1} - \alpha_{k_1}\right)\left(y_{k_2} - \alpha_{k_2}\right) \ldots \left(y_{k_n} - \alpha_{k_n}\right) \right\} dS_y \end{aligned} \tag{2.24}$$

This is the multipole expansion for the Stokes flow about a solid boundary in terms of higher order singularities. Note that all the contributions automatically satisfy continuity since the Stokeslet and its derivatives are solutions to the Stokes equations. The multipole expansion can also be written as[37]

$$u_i(\mathbf{x}) - u_i^{\infty}(\mathbf{x}) = -\frac{1}{8\pi\mu} G_{ij}(\mathbf{x}) F_j + \frac{1}{8\pi\mu} G_{ij,k}(\mathbf{x}) D_{jk} - \ldots \tag{2.25}$$

where the first term ($n = 0$) is the monopole contribution, the second term ($n = 1$) is the dipole contribution, the next term ($n = 2$) is the quadrapole contribution, etc. The monopole contribution or *Stokeslet* is due to a point force,

$$F_j = \int_{S_y} f_j \, dS_y \sim \frac{1}{x} \tag{2.26}$$

The dipole or *Stokes dipole* is due to a force dipole,

$$D_{jk} = \int_{S_y} f_j \left(y_k - \alpha_k\right) dS_y \sim \frac{1}{x^3} \tag{2.27}$$

The difference between the net dipole and its isotropic part can be represented as a sum of symmetric and asymmetric contributions as

$$D_{jk} - \frac{1}{3} D_{ii} \delta_{jk} = S_{jk} + T_{jk} \tag{2.28}$$

The symmetric part S_{jk} is known as the *stresslet*, and is given by

$$S_{jk} = \frac{1}{2} \int_{S_y} \left(f_j \left(y_k - \alpha_k \right) + f_k \left(y_j - \alpha_j \right) \right) \, dS_y - \frac{1}{3} \int_{S_y} f_i \left(y_i - \alpha_i \right) \delta_{jk} \, dS_y \tag{2.29}$$

The asymmetric part T_{jk} is known as the *rolet*, and is given by

$$T_{jk} = \frac{1}{2} \int_{S_y} \left(f_j \left(y_k - \alpha_k \right) - f_k \left(y_j - \alpha_j \right) \right) \, dS_y \tag{2.30}$$

The stresslet causes a straining motion at a point while the rolet results in a point torque. The velocity contributions from the different singularities are summarized below. The Stokeslet solution for flow due to a point force F_i at the origin is

$$u_i^s \left(\mathbf{x} \right) = \frac{1}{8\pi\mu} G_{ij} \left(\mathbf{x} \right) F_j \tag{2.31}$$

For a stresslet,

$$u_i^{ss} \left(\mathbf{x} \right) = \frac{1}{8\pi\mu} G_{ij,k} \left(\mathbf{x} \right) S_{kj} \tag{2.32}$$

and for a rolet,

$$u_i^r \left(\mathbf{x} \right) = \frac{1}{8\pi\mu} G_{ij,k} \left(\mathbf{x} \right) T_{kj} \tag{2.33}$$

A few examples of the velocity contributions will be shown below. These velocity contributions can be added together because of the linearity of the Stokes equations. Now, the Oseen tensor or Stokeslet,

$$G_{ij} = \frac{\delta_{ij}}{x} + \frac{x_i x_j}{x^3} \sim \frac{1}{x} \tag{2.34}$$

The derivative of the Stokeslet,

$$G_{ij,k} = \frac{\partial G_{ij}}{\partial x_k} = -\frac{x_k \delta_{ij}}{x^3} + \frac{x_j \delta_{ik}}{x^3} + \frac{x_i \delta_{jk}}{x^3} - \frac{3 x_i x_j x_k}{x^5} \sim \frac{1}{x^2} \tag{2.35}$$

The quadrapole solutions are more complicated, but one part of the quadrapole known as the *source dipole* is simple and useful and has the form[37]

$$\begin{aligned} u_i^{dp}(\mathbf{x}) &= -\frac{1}{2}\nabla^2 u_i^s(\mathbf{x}) = \frac{1}{8\pi\mu} G_{ij,kk} m_j \\ G_{ij,kk} &= \frac{\partial^2 G_{ij}}{\partial x_k \partial x_x} = -\frac{\delta_{ij}}{x^3} + \frac{3 x_i x_j}{x^5} \sim \frac{1}{x^3} \end{aligned} \tag{2.36}$$

2.3.4. Singularity representation for a sphere translating in an unbounded quiescent fluid

The expressions described earlier can be used to calculate the velocity of a sphere in a fluid, by adding up different singularities. A single isolated sphere of radius *a* with center at $\mathbf{x_0}$ translating in an unbounded quiescent fluid creates a velocity disturbance, which can be written as

$$u_i'(\mathbf{x}) = \frac{1}{8\pi\mu}\left(1 + \frac{1}{6}a^2 \nabla_{\mathbf{x_0}}^2\right) G_{ij}(\mathbf{x} - \mathbf{x_0}) F_j \tag{2.37}$$

The sphere acts as a point force **G**. There is also a quadrapole contribution to the velocity due to the finite size of the particle.[19] The quadrapole term is also needed to satisfy the no-slip condition on the surface of the particle.[19] It is worth mentioning here that the source dipole term conveniently reduces to the Laplacian of the Stokeslet only for a sphere.[19] The expansion in eq. (2.37) is sufficient to describe a sphere in a quiescent fluid. For cases where the fluid induces other kinds of motion in the sphere, such as torques and stresses, higher order singularities should be considered. Since most of the experiments we wish to simulate lie under the quiescent fluid case, we use eq. (2.37) to describe the velocity disturbance of a sphere. In the presence of multiple particles, this description is only adequate when the particle-particle separation is large compared to the radius of the particle. In other words, this expression for the velocity disturbance is the so called *far-field* assumption for the velocity. In order to describe the motion of the particles when they come close together, higher moments are required. These higher terms are incorporated in the so called *lubrication corrections*.[2,19] This is explained in detail in following sections.

Once we obtain the velocity field $\mathbf{u}'(\mathbf{x})$, the velocity of the particles can be computed by using Faxen's relations.[19] The velocity for a sphere in an unbounded fluid can be summarized as

$$\begin{aligned} u_i(\mathbf{x}) &= u_i^{\infty}(\mathbf{x}) + \left[1 + \frac{1}{6}a^2\nabla_{\mathbf{x}}^2\right]u_i'(\mathbf{x}) \\ u_i(\mathbf{x}) &= \frac{F_i}{6\pi\mu a} + \frac{1}{8\pi\mu}\left(1 + \frac{1}{6}a^2\nabla_{\mathbf{x}}^2\right)\left(1 + \frac{1}{6}a^2\nabla_{\mathbf{x_0}}^2\right)G_{ij}(\mathbf{x} - \mathbf{x_0})F_j \end{aligned} \tag{2.38}$$

In the following sections, we describe the construction of the hydrodynamic resistance tensor **R**. Two main situations will be considered, one for finite number of particles and another for infinite dispersions.

2.3.5. Finite particle systems in unbounded media

For the case of particles far from any surfaces, the far-field mobility tensor, $\mathbf{M}^{\infty}$, is constructed by summing all two-body far field interactions as

$$M^{\infty}_{\alpha i \beta j} = \delta_{\alpha\beta}\delta_{ij} + \left(1-\delta_{\alpha\beta}\right)\left[1+\left(a^2/6\right)\nabla^2_{\alpha}\right]\left[1+\left(a^2/6\right)\nabla^2_{\beta}\right]G_{ij}\left(\mathbf{r}_{\alpha}-\mathbf{r}_{\beta}\right) \qquad (2.39)$$

where $M_{\alpha i \beta j}$ is the mobility term of particle α in the i^{th} direction due to a force on particle β in the j^{th} direction, and G is the Green's function.[19,38] The mobility tensor, $\mathbf{M}^{\infty}$ is a far-field approximation to the true mobility tensor. It has two basic limitations. Firstly, the far-field tensor breaks down when two bodies get close to each other as it contains only second-order terms in the expansion of the Stokeslet (eq. (2.38)). The multipole expansion converges to the true solution only if a very large number of terms are considered.[19] Secondly, the mobility tensor contains only pair-wise interactions. Due to the long range of hydrodynamic interactions, many body interactions are extremely important and have to be considered. These two issues are resolved in the method of Stokesian Dynamics, where by eq. (2.7), the hydrodynamic interactions are separated into far-field and near-field parts. According to this method, first, the mobility tensor is inverted to obtain the far-field approximation for the resistance tensor. Although the mobility tensor, $\mathbf{M}^{\infty}$, is constructed based on a pair-wise approximation, inverting it has the effect of reflecting all force-velocity interactions among all particles.[19] Thus, the

inverse of the far-field mobility tensor, $\mathbf{R}^{\infty} = (\mathbf{M}^{\infty})^{-1}$, is a true far-field approximation to the many-body resistance matrix.[19]

This many body approximation to the resistance matrix still only describes the far-field hydrodynamics. To account for the near-field part, lubrication corrections are needed. There are some advantages in separating the far-field and near-field interactions. Unlike the far-field hydrodynamic interactions, the near-field interactions are mainly two-body interactions, and hence, lubrication can be added to the far-field resistance matrix in a pair-wise fashion.[2,19] To properly account for near-field lubrication forces, first a known exact two-body resistance tensor, $\mathbf{R}_{2B}$, is added to the far-field resistance tensor $\mathbf{R}^{\infty}$. The exact two-body problem has been solved by Jeffrey and Onishi,[39] who report the hydrodynamic resistance tensor in the notation of Batchelor[40]

$$\begin{aligned} R_{2B\alpha i\beta j} = {} & A_{\alpha\beta}\left(\left|\mathbf{r}_{\alpha}-\mathbf{r}_{\beta}\right|\right)\left(\frac{\left(\mathbf{r}_{\alpha}-\mathbf{r}_{\beta}\right)_i\left(\mathbf{r}_{\alpha}-\mathbf{r}_{\beta}\right)_j}{\left|\mathbf{r}_{\alpha}-\mathbf{r}_{\beta}\right|^2}\right) \\ & + B_{\alpha\beta}\left(\left|\mathbf{r}_{\alpha}-\mathbf{r}_{\beta}\right|\right)\left(\delta_{ij}-\frac{\left(\mathbf{r}_{\alpha}-\mathbf{r}_{\beta}\right)_i\left(\mathbf{r}_{\alpha}-\mathbf{r}_{\beta}\right)_j}{\left|\mathbf{r}_{\alpha}-\mathbf{r}_{\beta}\right|^2}\right) \end{aligned} \tag{2.40}$$

where the coefficients $A_{\alpha\beta}(r)$ and $B_{\alpha\beta}(r)$ are calculated by solving the exact two-body hydrodynamic problem.[33,39] The functional forms are given in terms of a normalized surface-to-surface separation, $s = r/a$. The A functions are calculated using the following expressions[39]

$$
\begin{aligned}
A_{\alpha\alpha}(r) = A_{\beta\beta}(r) &= g_1\left(1-4s^{-2}\right)^{-1} - g_2\ln\left(1-4s^{-2}\right)^{-1} \\
&\quad - g_3\left(1-4s^{-2}\right)^{-1}\ln\left(1-4s^{-2}\right)^{-1} + f_0 - g_1 \\
&\quad + \sum_{\substack{m=2 \\ m\text{even}}}^{\infty}\left\{2^{-2m}f_m - g_1 - 2m^{-1}g_2 + 4m^{-1}m_1^{-1}g_3\right\}\left(\frac{2}{s}\right)^m \\
-A_{\alpha\beta}(r) = -A_{\beta\alpha}(r) &= 2s^{-1}g_1\left(1-4s^{-2}\right)^{-1} \\
&\quad + g_2\ln\frac{s+2}{s-2} + g_3\left(1-4s^{-2}\right)^{-1} + 4g_3s^{-1} \\
&\quad + \sum_{\substack{m=1 \\ m\text{odd}}}^{\infty}\left\{2^{-2m}f_m - g_1 - 2m^{-1}g_2 + 4m^{-1}m_1^{-1}g_3\right\}\left(\frac{2}{s}\right)^m
\end{aligned}
\tag{2.41}
$$

where the different constants are given by

$$
\begin{aligned}
m_1 &= -2\delta_{m2} + (m-2)(1-\delta_{m2}) \\
g_1 &= 0.25, g_2 = 0.225, g_3 = 0.0268 \\
f_k &= 2^k\sum_{q=0}^{k} P_{1(k-q)q}
\end{aligned}
\tag{2.42}
$$

The P functions are based on recursive solutions, are given by[39]

$$
\begin{aligned}
P_{n00} &= V_{n00} = \delta_{1n} \\
V_{npq} &= P_{npq} - \frac{2n}{(n+1)(2n+3)}\sum_{i=1}^{q}\binom{n+i}{n}P_{i(q-i)(p-n-1)} \\
P_{npq} &= \sum_{i=1}^{q}\binom{n+i}{n}\left[\frac{n(2n+1)(2ni-n-i+2)}{2(n+1)(2i-1)(n+i)}P_{i(q-i)(p-n+1)}\right. \\
&\quad \left. - \frac{n(2n-1)}{2(n+1)}P_{i(q-i)(p-n-1)} - \frac{n(4n^2-1)}{2(n+1)(2i+1)}V_{i(q-i-2)(p-n+1)}\right]
\end{aligned}
\tag{2.43}
$$

The B functions are given by

$$
\begin{aligned}
B_{\alpha\alpha}(r) = B_{\beta\beta}(r) &= -\frac{1}{6}\ln\left(1-4s^{-2}\right)^{-1} + f_0 + \sum_{\substack{m=2 \\ m\text{even}}}^{\infty}\left\{2^{-2m}f_m - \frac{1}{3}m^{-1}\right\}\left(\frac{2}{s}\right)^m \\
-B_{\alpha\beta}(r) = -B_{\beta\alpha}(r) &= \frac{1}{6}\ln\frac{s+2}{s-2} + \sum_{\substack{m=1 \\ m\text{odd}}}^{\infty}\left\{2^{-2m}f_m - \frac{1}{3}m^{-1}\right\}\left(\frac{2}{s}\right)^m
\end{aligned}
\tag{2.44}
$$

and the functions f are calculated using eq. (2.42) with P functions calculated using the recursive functions

$$
\begin{aligned}
&P_{n00} = V_{n00} = \delta_{1n}, Q_{n00} = 0 \\
&V_{npq} = P_{npq} + \frac{2n}{(n+1)(2n+3)}\sum_{i=1}^{q}\binom{n+i}{n}P_{i(q-i)(p-n+1)} \\
&P_{npq} = \sum_{i=1}^{q}\binom{n+i}{n}\left[\frac{2n+1}{2(n+1)}\times\frac{3(n+i)-(ni+1)(2ni-n-i+2)}{i(n+i)(2i-1)}P_{i(q-i)(p-n+1)}\right. \\
&\quad + \frac{n(2n-1)}{2(n+1)}P_{i(q-i)(p-n-1)} + \frac{n(4n^2-1)}{2(n+1)(2i+1)}V_{i(q-i-2)(p-n+1)} \\
&\quad \left. - \frac{2(4n^2-1)}{3(n+1)}Q_{i(q-i-2)(p-n+1)}\right] \\
&Q_{npq} = \sum_{i=1}^{q}\binom{n+i}{n}\left[\frac{i}{n+1}Q_{i(q-i-1)(p-n)} - \frac{3}{2ni(n+1)}P_{i(q-i)(p-n)}\right]
\end{aligned}
\tag{2.45}
$$

However, because $\mathbf{R}_{2B}$ includes two-body resistances already accounted for in the construction of $\mathbf{R}^{\infty}$, a resistance tensor $\mathbf{R}_{2B}{}^{\infty}$ containing two-body interactions at the same order of approximation included in $\mathbf{R}^{\infty}$ is subtracted to avoid double counting. The far-field, two-body resistance tensor, $\mathbf{R}_{2B}{}^{\infty}$, is computed by summing up the inverse of far-field, two-body mobility tensors, $\mathbf{M}^{\infty}$, containing terms to the same order as $\mathbf{R}^{\infty}$

$$
M^{\infty}_{\alpha i\beta j} = \delta_{\alpha\beta}\delta_{ij} + (1-\delta_{\alpha\beta})\left[1+\left(a^2/6\right)\nabla^2_{\alpha}\right]\left[1+\left(a^2/6\right)\nabla^2_{\beta}\right]G_{ij}(\mathbf{r}_{\alpha}-\mathbf{r}_{\beta}) \tag{2.46}
$$

$$R_{2B,ij}^{\infty} = \left(\sum_{\substack{\alpha,\beta=1 \\ \beta>\alpha}}^{N} \left(\mathbf{M}_{\alpha\beta}^{\infty} \right)^{-1} \right)_{ij} \tag{2.47}$$

2.3.6. Finite particle systems near a plane wall

For the case of particles near a stationary plane wall, Bossis et al.[22] adapted the method outlined above to consider hydrodynamic interactions with the wall in a multi-body resistance tensor. Similar to eq. (2.6), the hydrodynamic force, $\mathbf{F}_{\alpha}^{H}$, on a particle α in the presence of other particles and a plane wall is linearly related to the particle velocities through Stokes equations. The resistance tensor, **R**, is now a function of particle-particle and particle-wall separations. The total resistance tensor can again be calculated using eq. (2.7) by summing separate far-field, multi-body and near-field lubrication parts. In the same notation used above for unbounded particles, the expression for the far-field mobility tensor is written as,[22]

$$\begin{aligned} M_{\alpha i \beta j}^{\infty} = \delta_{\alpha\beta} \Big(\delta_{ij} + \left[1 + \left(a^2/6 \right) \nabla_{\alpha}^2 \right] \left[1 + \left(a^2/6 \right) \nabla_{\alpha'}^2 \right] G_{w,ij} \left(\mathbf{r}_{\alpha} - \mathbf{r}_{\alpha}' \right) \Big) \\ + \left(1 - \delta_{\alpha\beta} \right) \left[1 + \left(a^2/6 \right) \nabla_{\alpha}^2 \right] \left[1 + \left(a^2/6 \right) \nabla_{\beta}^2 \right] \\ \times \left[G_{ij} \left(\mathbf{r}_{\alpha} - \mathbf{r}_{\beta} \right) + G_{w,ij} \left(\mathbf{r}_{\alpha} - \mathbf{r}_{\beta}' \right) \right] \end{aligned} \tag{2.48}$$

where, $\mathbf{r}_{\alpha}'$ is the vector representing the image of particle α with respect to the wall and G_w is the Green's function due to the presence of the wall, constructed using the image representation of a particle near a plane surface.[23] The primes denote the position of the particle images with respect to the plane surface. The far-field multi-body resistance tensor is again obtained by inversion of the far-field mobility tensor (eq. (2.8)).

Lubrication corrections are to be added to the far-field resistance tensor as described earlier. In addition to particle-particle lubrication corrections, particle-wall lubrication must also be added to accurately represent the wall's no-slip boundary condition. The expression for the exact particle-particle resistance tensor is given in eq. (2.40), and the exact particle-wall resistance tensor is given by,

$$R_{\alpha wij} = C\left(\left|\mathbf{z}_\alpha - \mathbf{z}_w\right|\right)\delta_{ij}\delta_{i3} + D\left(\left|\mathbf{z}_\alpha - \mathbf{z}_w\right|\right)\delta_{ij}\left(1-\delta_{i3}\right) \tag{2.49}$$

where $\mathbf{z}$ denotes the coordinate normal to the plane surface, the subscripts α and w denote the particle and wall, and the coefficients $C(h)$ and $D(h)$ are reported in literature[41] as solutions of the particle-wall hydrodynamic problem. These solutions are conveniently expressed in terms of the particle-wall separation, h, by rational fits (with less than ±0.001 relative error) as

$$\begin{aligned} C(h) &= \frac{12420\gamma\left(h\right)^2 + 12233\gamma\left(h\right) + 431}{12420\gamma\left(h\right)^2 + 5654\gamma\left(h\right) + 100} \\ D\left(h\right) &= \frac{6\gamma\left(h\right)^2 + 9\gamma\left(h\right) + 2}{6\gamma\left(h\right)^2 + 2\gamma\left(h\right)} \end{aligned} \tag{2.50}$$

where, $\gamma(h) = (h\text{-}a) / a$. The exact two-body resistance tensor is evaluated by adding exact two-body particle-particle (eq. (2.40)) and particle-wall (eq. (2.49)) resistance tensors

$$R_{2B,ij} = \left(\sum_{\alpha,\beta=1}^{N} \left(\delta_{\alpha\beta}\mathbf{R}_{\alpha w} + \left(1-\delta_{\alpha\beta}\right)\mathbf{R}_{\alpha\beta} \right) \right)_{ij} \tag{2.51}$$

Similar to the particle-particle case, since $\mathbf{R}_{2B}$ contains the far-field part, which is already accounted for in $\mathbf{R}^{\infty}$, a far-field two-body resistance tensor, $\mathbf{R}_{2B}{}^{\infty}$, containing two-body interactions at the same order of approximation as $\mathbf{R}^{\infty}$ is subtracted to avoid double counting. This far-field approximation is the sum of particle-particle and particle-wall resistance tensors given by,

$$\begin{aligned} M^{\infty}_{w,\alpha i\alpha j} &= \delta_{ij} + \left[1+\left(a^2/6\right)\nabla^2_{\alpha}\right]\left[1+\left(a^2/6\right)\nabla^2_{\alpha'}\right] G_{w,ij}\left(\mathbf{r}_{\alpha}-\mathbf{r}_{\alpha}{}'\right) \\ M^{\infty}_{\alpha i\beta j} &= \delta_{\alpha\beta}\delta_{ij} + \left(1-\delta_{\alpha\beta}\right)\left[1+\left(a^2/6\right)\nabla^2_{\alpha}\right]\left[1+\left(a^2/6\right)\nabla^2_{\beta}\right] \\ &\quad \times\left[G_{ij}\left(\mathbf{r}_{\alpha}-\mathbf{r}_{\beta}\right)+G_{w,ij}\left(\mathbf{r}_{\alpha}-\mathbf{r}_{\beta}{}'\right)\right] \\ R^{\infty}_{2B,ij} &= \left(\sum_{\alpha,\beta=1}^{N}\left(\delta_{\alpha\beta}\left(\mathbf{M}^{\infty}_{\alpha w}\right)^{-1}+\left(1-\delta_{\alpha\beta}\right)\left(\mathbf{M}^{\infty}_{\alpha\beta}\right)^{-1}\right)\right)_{ij} \end{aligned} \tag{2.52}$$

In problems involving colloids confined between two planar surfaces at small separations, dominant near-field contributions allow the resistance tensor to be constructed using a simple superposition of effects due to the two walls. The net effect of the two walls can be represented by writing a net resistance tensor as,

$$\mathbf{R} = \sum_{\alpha=1}^{N}\sum_{\beta=1}^{N}\left[\left(\delta_{\alpha\beta}\mathbf{R}_{\alpha}+\mathbf{R}_{\alpha\beta}\right)_{w1}+\left(\delta_{\alpha\beta}\mathbf{R}_{\alpha}+\mathbf{R}_{\alpha\beta}\right)_{w2}\right] \tag{2.53}$$

where $w1$ and $w2$ denote the two walls. This approach has been shown previously to yield fairly accurate results for the case of dilute confined colloidal dispersions in comparison to more rigorous treatments.[42]

2.3.7. Infinite particle dispersions in unbounded media

Simulations involving infinite dispersions via periodic boundary conditions warrant a different approach for constructing the hydrodynamic resistance tensor, due to the long-range ($1/r$) nature of hydrodynamic interactions. Brady and Bossis[2] formulated a method combining O'Brien's approach of an integral representation of the solution of Stokes equations for the fluid velocity field with Ewald's summation technique. This method will be briefly described here. For details, the reader is referred to the original references.[2,20,43]

For simulating infinite dispersions, the simulation box with a finite number of particles is periodically replicated in three dimensions to mimic an infinite system. The key step in Stokesian Dynamics, of separating the hydrodynamic interactions into a far-field multi-boy and near-field lubrication forces remains unchanged, i.e., eq. (2.7) is used to calculate the hydrodynamic resistance tensor. The far-field mobility tensor for a periodically replicated system is constructed by using the expression for the Ewald-summed far-field mobility tensor as derived by Beenakker.[21] The mobility tensor in eq. (2.8) is now calculated using

$$\begin{aligned}\left(6\pi\mu a\right)M_{\alpha i\beta j} = &\left(1-6\pi^{-1/2}\xi a+\frac{40}{3}\pi^{-1/2}\xi^3 a^3\right)\delta_{\alpha\beta}\delta_{ij}\\ &+\sum_{l,\mathbf{r}_{\alpha l}\neq\mathbf{r}_{\alpha l_0}}\sum_{\beta=1}^{N}M_{ij}^{1}\left(\mathbf{r}_{\alpha l}-\mathbf{r}_{\beta l_0}\right)\\ &+V^{-1}\sum_{\lambda,\mathbf{k}_\lambda\neq 0}\sum_{\beta=1}^{N}M_{ij}^{2}\left(\mathbf{k}_\lambda\right)\cos\left\{\mathbf{k}_\lambda\cdot\left(\mathbf{r}_{\alpha l}-\mathbf{r}_{\beta l_0}\right)\right\}\end{aligned} \tag{2.54}$$

where $M_{\alpha i\beta j}$ is the mobility of particle α in the i^{th} direction due to a force on particle β in

the j^{th} direction and μ is the continuous medium viscosity. The lattice points in real space are given by the vectors r_l, and the particles have position vectors $r_{\alpha l} = r_\alpha + r_l$. The reciprocal space lattice vectors are denoted by k_λ, satisfying the condition $\exp(ik_\lambda \cdot r_l) = 1$ for all l. The first sum represents summation over real space and the second over reciprocal space. The paper by Beenakker[21] provides explicit expressions for the functions M^1 and M^2 as

$$\begin{aligned}
\mathbf{M}^1(\mathbf{r}) = \mathbf{I}\Bigg\{&\left(\frac{3}{4}ar^{-1} + \frac{1}{2}a^3r^{-3}\right)erfc(\xi r) + \Big(4\xi^7a^3r^4 + 3\xi^3ar^2 \\
&-20\xi^5a^3r^2 - \frac{9}{2}\xi a + 14\xi^3a^3 + \xi a^3r^{-2}\Big)\pi^{-1/2}\exp\left(-\xi^2r^2\right)\Bigg\} \\
&+\frac{\mathbf{rr}}{r^2}\Bigg\{\left(\frac{3}{4}ar^{-1} - \frac{3}{2}a^3r^{-3}\right)erfc(\xi r) + \Big(-4\xi^7a^3r^4 - 3\xi^3ar^2 \\
&+16\xi^5a^3r^2 + \frac{3}{2}\xi a - 2\xi^3a^3 - 3\xi a^3r^{-2}\Big)\pi^{-1/2}\exp\left(-\xi^2r^2\right)\Bigg\} \\
\mathbf{M}^2(\mathbf{k}) = &\left(\mathbf{I} - \frac{\mathbf{kk}}{k^2}\right)\left(a - \frac{1}{3}a^3k^2\right)\left(1 + \frac{1}{4}\xi^{-2}k^2 + \frac{1}{8}\xi^{-4}k^4\right) \\
&\times 6\pi k^{-2}\exp\left(-\frac{1}{4}\xi^{-2}k^2\right)
\end{aligned} \tag{2.55}$$

Where **r** and **k** are the real-space and lattice vectors, with $r = |\mathbf{r}|$ and $k = |\mathbf{k}|$, and **I** is the identity tensor. Beenakker suggests an optimal value of the split parameter as given by $\xi = \pi^{1/2}V^{-1/3}$, where V is the volume of the simulation box.

The far-field resistance tensor still lacks lubrication corrections. To account for this, lubrication forces are added as near-field lubrication forces are added in a manner as described in section 2.3.1. by first adding an exact two-body resistance tensor, $\mathbf{R}_{2B}$

(eq. (2.40)), is and subtracting off the far-field part of the two-body resistance tensor, $\mathbf{R}_{2B}^{\infty}$ (eqs. (2.46) and (2.47)).

2.3.8. Infinite particle dispersions in bounded media

In case of interfacial colloids, the resistance tensor also depends on the position of particles relative to the wall. Nott and Brady[24] and Singh and Nott[25] further extended this method for including the effect of a wall. In presence of a wall, the resistance tensor must be constructed to include the effects of the boundary conditions at the wall. To incorporate this, the wall is discretized into an array of N_w spheres of radius equal to the radius of the dispersed particles, a.[24,25] A far-field mobility tensor is constructed, in pairwise manner, for $N = N_p + N_w$ particles, resulting in a $3N \times 3N$ far-field mobility tensor. The far-field mobility interactions are calculated in the usual manner by using the expression for the Ewald-summed Rotne-Prager tensor as derived by Beenakker for a 3D periodically replicating simulation cell. A schematic of the simulation cell is shown in fig. 2.1.

To properly account for near-field lubrication forces, first an exact two-body resistance tensor, $\mathbf{R}_{2B}$, is added to the far-field resistance tensor $\mathbf{R}^{\infty}$. The exact 6×6 two-body resistance tensor is a sum of an exact particle-particle resistance tensor and an exact particle wall resistance tensor. The exact particle-particle (eq. (2.40)) and particle-wall (eq. (2.49)) tensors have been discussed in earlier sections. However, because $\mathbf{R}_{2B}$ includes two-body resistances already accounted for in the construction of the far-field resistance tensor, $\mathbf{R}^{\infty}$, a resistance tensor $\mathbf{R}_{2B}^{\infty}$ containing far-field two-body interactions

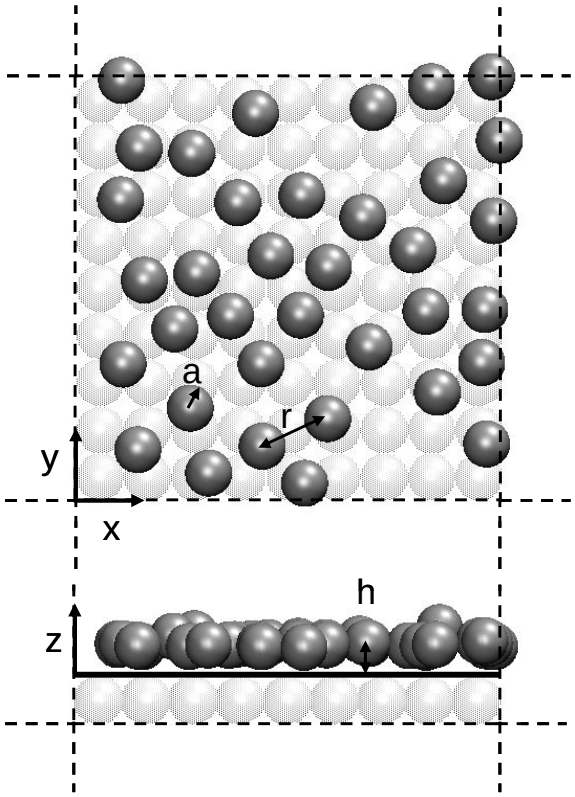

Figure 2.1. Schematic representation of the simulation cell showing the free particles (gray spheres) and wall patches (white spheres) in top view (top) and side view (bottom). The side view (bottom) also shows the position of the wall for near-field calculations.

at the same order of approximation included in $\mathbf{R}^{\infty}$ is subtracted to avoid double counting.[2] $\mathbf{R}_{2B}^{\infty}$ is calculated by constructing two-body particle-particle and particle-wall mobility tensors and inverting them.

The particle-particle mobility tensor is calculated for free particle pairs as described in previous sections. For the particle-wall two body resistance tensor, a mobility tensor is calculated using eq. (2.46) for each particle with all the wall "particles" to give a mobility tensor of size $3(N_w+1)$.[25] This far-field mobility tensor is

inverted to give a far-field resistance tensor for a free particle with all the wall patches. This is done for all the free particles. These two tensors are added to yield a two-body far-field resistance tensor. The total resistance tensor, after construction, is of size $3(N_p+N_w)$. However, since the wall particles are fixed, we know their velocities ($\mathbf{U}_w = 0$), and we assume that they do not experience Brownian motion. This allows us to use a subset of the resistance tensor containing only free particles of size $3N_p$ in the time evolution equation for the free particle trajectories (eq. (2.5)).

2.4. Colloidal and External Forces

Colloidal and external conservative forces are calculated as the gradient of a scalar potential energy function. The conservative forces included in this work include interaction potential between particle-particle and particle-wall pairs and the external force is gravity. All colloidal forces are assumed to be pairwise additive. The forces are expressed as

$$\mathbf{F}^P = \mathbf{F}^{pp} + \mathbf{F}^{pw} + \mathbf{F}^{grav} \tag{2.56}$$

where $\mathbf{F}^{pp}$ is the force due to particle-particle interaction, F^{pw} is the force due to particle wall interaction and $\mathbf{F}^{ext}$ is the external force. The particle-particle and particle-wall forces are calculated as the derivative of their respective potential energy functions $u_{pp}(r)$ and $u_{pw}(h)$, and are given by

$$\begin{aligned} \mathbf{F}^{pp} &= -\nabla u_{pp}(r) \\ \mathbf{F}^{pw} &= -\nabla u_{pw}(h) \end{aligned} \tag{2.57}$$

where r is the particle-particle separation and h is the particle-wall separation. The colloidal forces considered in this work include electrostatic, van der Waals, and steric forces. The net particle-particle and particle-wall potentials are represented as the superposition of these relevant potentials as

$$\begin{aligned} u_{pp}(r) &= u_{pp}^{elec}(r) + u_{pp}^{vdw}(r) + u_{pp}^{steric}(r) \\ u_{pw}(h) &= u_{pw}^{elec}(h) + u_{pw}^{vdw}(h) + u_{pw}^{steric}(h) \end{aligned} \tag{2.58}$$

The electrostatic particle-particle and particle-wall pair potentials for these conditions are well represented by[34]

$$\begin{aligned} u_{pp}(r) &= B_{pp} \exp\left[-\kappa(r-2a)\right] \\ u_{pw}(h) &= B_{pw} \exp\left[-\kappa(h-a)\right] \end{aligned} \tag{2.59}$$

The B parameters are related to the particle size and surface potentials as

$$\begin{aligned} B_{pp} &= 32\pi\varepsilon a\left(\frac{k_B T}{ze}\right)^2 \tanh\left(\frac{ze\psi_p}{4kT}\right)\tanh\left(\frac{ze\psi_p}{4kT}\right) \\ B_{pw} &= 2B_{pp} \end{aligned} \tag{2.60}$$

where ε is the absolute permittivity, z is the charge number of the ions in the solvent, and κ is the Debye screening length given by

$$\kappa = \left(\frac{2CN_A e^2}{\varepsilon k_B T}\right) \tag{2.61}$$

Here, C is the bulk electrolyte concentration, N_A is Avogadro's constant, and e is the charge on an electron.

The van der Waals forces arise due to a mismatch in the particle and medium dielectric properties and are well represented by a non-integer power-law decay fit to Lifshitz theory by[44]

$$u_{pp}^{vdw}(r) = -aA(r-2a)^{-p}$$
$$u_{pw}^{vdw}(h) = -2aA(h-a)^{-p} \tag{2.62}$$

where a is the particle radius and A and p are non-integer fitting parameters.

Substrates with adsorbed polymer layers experience a steric force, which can be represented by a "hard wall" interaction having the mathematical form,

$$u^{steric}(x) = \begin{cases} 0 & x > x_{ref} \\ \infty & x \le x_{ref} \end{cases} \tag{2.63}$$

which is suitable for either the particle or the wall by substituing center-to-center seperation, r, or center-to-surface separation, h, for x, and x_{ref} is reference for zero surface separation corresponding to hard wall contact.

The only external force considered is the gravitational or buoyant force. The gravitational force is given by

$$\mathbf{F}^{grav} = -\frac{4}{3}\pi a^3 \left(\rho_p - \rho_f\right) g \tag{2.64}$$

where ρ_p and ρ_f are the densities of the particle and the fluid respectively, and g is the force per unit mass due to gravity.

3. STOKESIAN DYNAMICS CODE IMPLEMENTATION

3.1. Synopsis

This section describes the algorithmic and implementation details of the Stokesian Dynamics code for simulating Brownian particles dispersed in a viscous fluid medium under the influence of interparticle and external forces in both unbounded and bounded systems. First, the mid-point algorithm for the evolution equation of particle trajectories is described. The remainder of this section is a summary of some of the practical aspects of the construction and execution of the code.

3.2. Mid-Point Algorithm

Before we discuss the mechanics of the simulations, we recall the propagation equation for particle trajectories from the theory section.

$$\begin{gathered}\mathbf{r} = \mathbf{r}^0 + k_B T\left(\nabla\cdot\left(\mathbf{R}^0\right)^{-1}\right)\Delta t + \left(\mathbf{R}^0\right)^{-1}\cdot\mathbf{F}^{P,0}\Delta t + \mathbf{X}^0\left(\Delta t\right) \\ \left\langle\mathbf{X}\left(\Delta t\right)\right\rangle = 0, \left\langle\mathbf{X}\left(\Delta t\right)\mathbf{X}\left(\Delta t\right)\right\rangle = 2\mathbf{R}^{-1}\Delta t\end{gathered} \tag{3.1}$$

Although eq. (2.5) can be numerically solved to obtain particle trajectories, the second term, the spatial gradient of the resistance tensor, is expensive to compute explicitly. To avoid this expensive computation, Banchio and Brady[45] suggested the use of a method based on Fixman's[46,47] original mid-point scheme. To illustrate this method, the Brownian displacement in eq. (2.5) is first re-written in terms of the Brownian force as,

$$\begin{aligned}\mathbf{r} &= \mathbf{r}^0 + k_B T\left(\nabla\cdot\left(\mathbf{R}^0\right)^{-1}\right)\Delta t + \left(\mathbf{R}^0\right)^{-1}\cdot\left(\mathbf{F}^{P,0}+\mathbf{F}^{B,0}\right)\Delta t \\ \left\langle \mathbf{F}^B\right\rangle &= 0, \left\langle \mathbf{F}^B(0)\mathbf{F}^B(t)\right\rangle = 2k_B T\mathbf{R}\delta(t)\end{aligned} \tag{3.2}$$

From an initial particle configuration $\mathbf{r}^0$, the velocity is calculated as

$$\mathbf{U}^0 = \left(\mathbf{R}^0\right)^{-1}\cdot\left(\mathbf{F}^{P,0}+\mathbf{F}^{B,0}\right) \tag{3.3}$$

The particles are "moved" by a small fraction of the time step to an intermediate position by

$$\mathbf{r}' = \mathbf{r}^0 + \frac{\Delta t}{m}\mathbf{U}^0 \tag{3.4}$$

where m is usually in order of 100. A new velocity is computed at the intermediate particle configuration

$$\mathbf{U}' = \left(\mathbf{R}'\right)^{-1}\cdot\left(\mathbf{F}^{P,0}+\mathbf{F}^{B,0}\right) \tag{3.5}$$

Note that the premultiplying resistance tensor is now computed using the new coordinates, $\mathbf{r}'$, while the forces remain constant. The drift velocity, calculated via the modified mid-point scheme is

$$\mathbf{U}^{drift} = \frac{m}{2}\left(\mathbf{U}' - \mathbf{U}^0\right) \tag{3.6}$$

The new configuration, for a time step of Δt is finally calculated as

$$\mathbf{r} = \mathbf{r}^0 + \left(\mathbf{U}^0 + \mathbf{U}^{drift}\right)\Delta t \tag{3.7}$$

Eqs. (3.3)-(3.7) are used to obtain the new configuration after a time interval Δt. The calculations of different terms in the above equations will be described in the remainder of this section.

3.3. Instruction Flow and Code Details

The general idea in Stokesian Dynamics is to start with a given particle configuration, from which the conservative forces, Brownian forces, and the hydrodynamic resistance tensor can be calculated. Using these, particle coordinates are advanced in time based on eq. (3.2) using the modified mid-point algorithm described earlier. The different steps are described in detail below, and are graphically represented by a flow chart.

3.3.1. Input parameters

The input parameters are read into the code from an input file titled *run.txt*. The different inputs to be specified, dimensions where applicable, and variable names are summarized below:

Number of particles: *n*/*np*

Number of wall patches: *nw* (only for infinite unbounded systems)

Number of walls: *nw* (only for finite bounded systems)

Spacing between walls (nm): *boxlenz*

Particle radius (nm): *a*

Number of simulation steps: *nstep*

Number of initial steps to be ignored: *istart*

Interval for data output: *iprint*

Temperature (°C): *tempr*

Time step for driving simulation (ms): *dt*

File name containing initial particle configuration: *par_in*

File name containing coordinates for wall patches: *wall_in* (only for infinite bounded systems)

File name for outputting particle coordinates: *par_out*

Particle concentration (area fraction/volume fraction): *phi* (only for infinite systems)

Numerical simulations in this work were done to complement real experiments done in the group, and were formulated to receive inputs such as physical constants and force expressions, directly from experiments. This is why variables are expressed in absolute dimensions instead of the more common non-dimensional representation. The physical parameters such as particle and medium density, medium viscosity are not required as inputs to the dynamic simulation. Instead, they are specified in a MATHCAD® document where particle-particle and particle-wall potential functions are calculated. From this, expressions for conservative forces are extracted, which is hard-wired in the dynamic simulation code in the subroutine *forces.f*. This, allows a seamless integration between potentials measured experimentally and numerical simulations, enabling a close collaboration between simulation and experiment.

3.3.2. Initial particle configuration

The initial particle configuration needs to be specified before starting the simulation. This is specified through a text file with all particle coordinates (in units of nm). Almost always, the initial configuration needs to be an equilibrium configuration based on the specified interaction potentials. Equilibrium particle configurations can be obtained by simple NVT Monte Carlo simulations, based on the algorithm of Allen and Tildesley,[48] which can be used as inputs to the more expensive dynamic simulation. For bounded infinite systems, an input containing coordinates of "patches" making up the wall is also required. For hydrodynamic calculations, the wall is replaced by an array of touching spheres. The coordinates of these spheres needs to be specified as input to the code. These can be generated externally by another routine, *wall_patch.f*.

3.3.3. Different steps in the dynamic simulation

The sequential order of calculations in the Stokesian Dynamic code is presented below. These are also represented graphically in the flow sheet (fig. 3.1).

Step 1.

Input parameters are read by the main program *main.f* and initial particle configurations are read by the subroutine *readcn.f*. The code is set up to receive initial particle coordinates normalized by the particle radius (instead of nm), since the Monte Carlo code outputs particle coordinates in this format. However, *readcn.f* can be changed to read in coordinates in other formats.

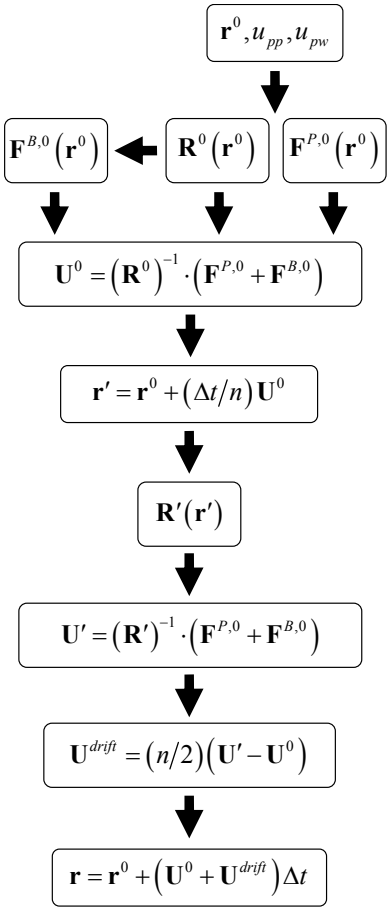

Figure 3.1. Flow chart for Stokesian Dynamics code showing different steps in the time evolution equation.

Step 2.

The hydrodynamic resistance tensor is calculated by adding a far-field multi-body resistance tensor and near-field lubrication corrections as described in the theory section. These are handled in the subroutine *grndrm.f* and other subroutines invoked inside *grndrm.f*. The far-field part of the resistance tensor only changes if the particle

configuration changes significantly. Hence, a new calculation is done only if the average particle displacement, $\langle \mathbf{r}(t+\Delta t) - \mathbf{r}(t) \rangle$, is greater than a specified quantity. In the code, this is set to $0.1a$. The lubrication correction has to be calculated at every step. This however, is computationally less expensive. In the case of infinite (periodic) systems, the other adjustable parameter is the number of wave vectors for the real and imaginary space sums in the calculation of Ewald sum for the far-field mobility tensor. These are specified by variables *rwald* and *kwald* and are hard-wired in the *main.f* program. These variables are both set to be equal to 3, although in case of highly confined systems, the value may have to be increased to 5. It is recommended, however, that these variables remain hard-wired instead of being user inputs. In computing the singular lubrication forces, particle-overlaps are handled in the method of Phung, et al.[43] According to this method, when overlap occurs, the lubrication forces are computed at a very small surface-surface separation ($10^{-8}a$), and the rest of the calculations proceed as usual. This has been shown to reproduce the right equilibrium microstructure[26].

Step 3.

The conservative forces are calculated using the particle configuration in the subroutine *forces.f*. The expression for forces is pre-computed in a MATHCAD® document, and input in the subroutine. The forces are expressed in units of nN (10^{-9}N).

Step 4.

The random (Brownian) contribution to the displacement is calculated by passing the hydrodynamic resistance tensor into the Cholesky decomposition subroutines, *choldc.f*

and *random.f*. These routines output a $3N_p$ vector of random displacements. The generation of random particle displacements requires the use of a standard long-period random number generator, *ran2.f*[49]. This random number generator requires an initial seed as a starting point[49]. The seed for the random number generator in the Stokesian Dynamics code is a negative integer which is specified in *main.f* under the variable name *idummy*. It is set at a value of -7. This can be changed if desired, provided it remains a negative integer.

Step 5.

Using these forces, the initial velocity, **U**, is calculated as in eq. (3.3). The inversion of the resistance tensor, done in the subroutine *invert.f* is computationally the most expensive step, which scales with the number of particles as N^3.

Step 6.

The particles are moved by a small fraction of the time step, Δt to a new position as described by eq. (3.4). The time step, Δt, is an input parameter and is chosen such that the change in particle configuration within that time step does not alter the forces significantly. A good estimate for Δt is $10^{-4}\tau - 10^{-5}\tau$, where $\tau = 6\pi\mu a^3/kT$ is the diffusive time scale. The fraction of the time step, *m*, is declared in *main.f*, and has a value of 100.

Step 7.

A new velocity is calculated by recomputing the hydrodynamic resistance tensor for the new particle configuration (eq. (3.5)).

Step 8.

The new particle positions after a time step Δt are obtained using eqs. (3.6) and (3.7). Output coordinates are written to the output file in specified time intervals through the subroutine *writcn.f*. The output format is in accordance with the standard Bevan group coordinate output format.

Steps 2-8 are repeated for the specified total number of steps to obtain particle trajectories. At each time step, the short-time self-diffusion coefficient is also outputted into a file "*d.txt*". For the case of bounded systems, separate lateral and normal diffusion coefficients can also be outputted. These modifications are done in *main.f*. The schematic representation of the different steps is shown below in fig. 3.1.

3.3.4. Description of subroutines – Finite systems

The different subroutines in the code for simulating a finite system are described below, and the information flow between them is represented schematically in fig. 3.2.

main.f: This is the main program. It reads in user inputs and outputs data. Other subroutines are connected to this as represented in fig. 3.2.

forces.f: Subroutine to calculate forces for a given configuration. The force expressions are calculated externally in a MATHCAD document. Forces are output as a vector of size $3N_p$ and have units of nN.

choldc.f: Subroutine to calculate the Cholesky decomposition of a tensor. Cholesky decomposition is the factorization of a symmetric and positive definite matrix into the

product of a lower triangular matrix and its transpose. If **A** is a symmetric, positive definite matrix, it can be decomposed as

$$\mathbf{A} = \mathbf{L} \cdot \mathbf{L}^T \tag{3.8}$$

where **L** is a lower triangle matrix, and $\mathbf{L}^T$ is its transpose. The subroutine is based on an implementation In Numerical Recipes.[49] The subroutine receives the hydrodynamic resistance tensor and outputs its Cholesky decomposition.

random.f: Subroutine to calculate the Brownian contribution to the particle displacement. The subroutine takes a set of normally distributed random numbers between 0 and 1 and weighs it by the Cholesky decomposed resistance tensor. The output is a vector of size $3N_p$ containing random particle displacements.

gasdev.f: Converts a set of uniformly distributed random numbers between 0 and 1 into a set of normally distributed random numbers with 0 mean and unit varaince. The subroutine is based on an implementation in Numerical Recipes.[49]

ran2.f: Long-period random number generator[49], which outputs uniformly distributed random numbers between 0 and 1. The generator requires a negative integer input which acts as a seed. This is specified by the variable *idummy* in *main.f*.

invert.f: Subroutine to invert a matrix based on LU decomposition. The decomposition is done in two connected subroutines, *ludcmp.f* and *lubksb.f*. The algorithm is based on implementation given in Numerical Recipes.[49]

dtensor.f: Subroutine to calculate the hydrodynamic resistance/mobility tensor. The hydrodynamic resistance tensor is calculated as the sum of far-field and near-field terms[2].

greenact.f: The far-field, multi body mobility tensor is calculated in this subroutine, and passed on to *dtensor.f*.

ppexact.f: The particle-particle exact hydrodynamic resistance is computed based on exact solutions to the two-particle problem reported in literature.[39]

pwexact.f: Calculates the particle-wall exact hydrodynamic resistance tensor based on the exact solutions reported by Brenner.[41]

greenpp.f: Computes the far-field particle-particle resistance tensor.

greenpw: Computes the far-field particle-wall resistance tensor.

3.3.5. Description of subroutines – Infinite systems

The different subroutines in the code for simulating infinite systems are presented below. The information flow is presented in fig. 3.3.

main.f: Main program which reads in input parameters and writes outputs.

readcn.f: Reads in input particle coordinates.

writcn.f: Writes particle coordinates into output file. The output is in the standard Bevan group format, including headers.

forces.f, *random.f*, *choldc.f*, *gasdev.f*, *ran2.f*, *invert.f*, *ludcmp.f*, *lubksb.f*: Subroutines described in the previous section.

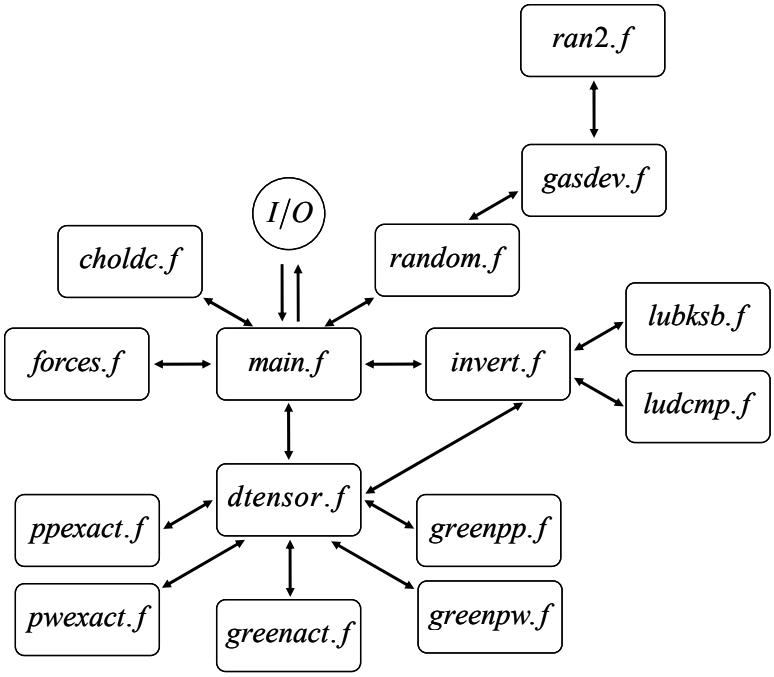

Figure 3.2. Flow chart showing information flow in the SD code for finite systems.

grndrm.f: Subroutine to calculate the grand resistance tensor.

farfldres.f: Subroutine to calculate the far-field, multi-body resistance tensor.

selftm.f: Subroutine to calculate the self-term in the Ewald sum for the hydrodynamic resistance tensor.

ffwall.f: Subroutine to calculate the far-field contribution from the wall patches to the multi-body hydrodynamic mobility tensor.

ffw2b.f: Subroutine to calculate the far-field contribution from the wall patches to the far-field two body hydrodynamic mobility tensor.

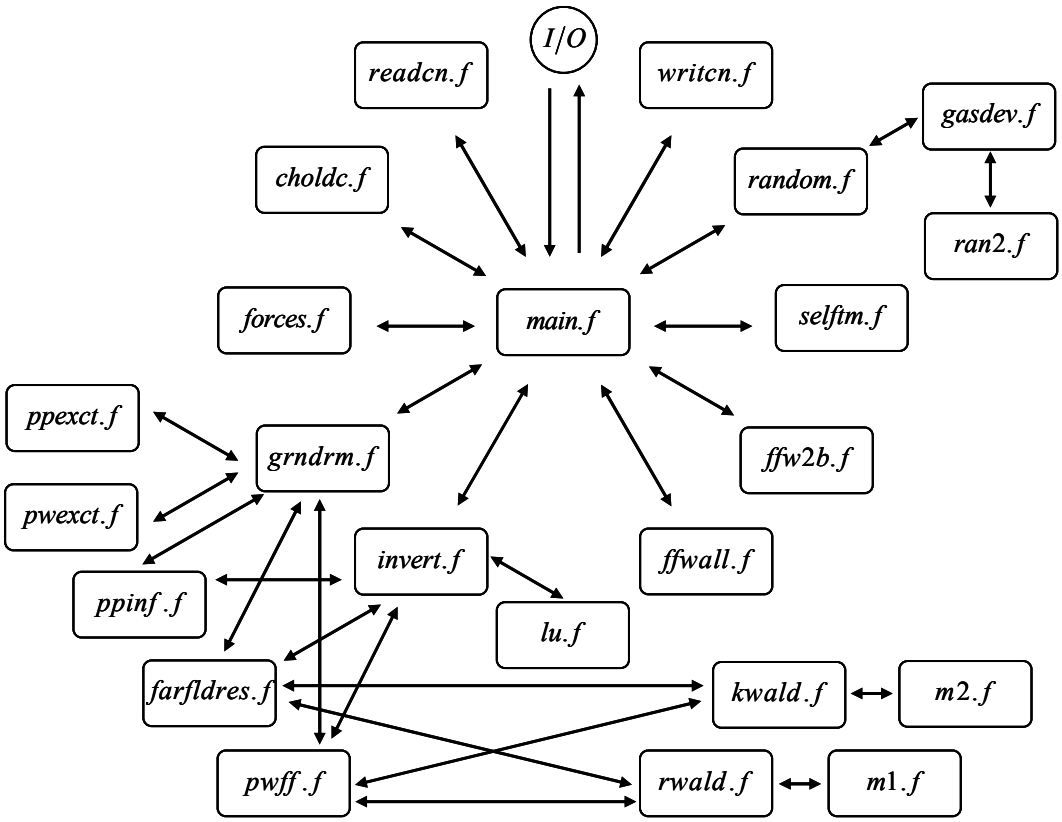

Figure 3.3. Flow chart showing information flow in the SD code for infinite systems.

ppexct.f, *pwexct.f*: Subroutines to calculate exact two body particle-particle and particle resistance tensors.

ppinf.f, *pwff.f*: Subroutines to calculate far-field two body particle-particle and particle resistance tensors.

rwald.f: Subroutine to calculate the real-space part of the Ewald sum for the far-field resistance tensor using the method of Beenakker.[21]

kwald.f: Subroutine to calculate the Fourier-space part of the Ewald sum for the far-field resistance tensor using the method of Beenakker.[21]

m1.f, *m2.f*: Subroutines to calculate constants for the Ewald sum.

4. INTERPRETATION OF CONSERVATIVE POTENTIALS FROM STOKESIAN DYNAMIC SIMULATIONS OF INTERFACIAL AND CONFINED COLLOIDS

4.1. Synopsis

This section presents Stokesian Dynamics simulations of experiments involving one or two charged colloids near either a single charged wall or confined between parallel charged walls. Equilibrium particle-particle and particle-wall interactions are interpreted from dynamic particle trajectories in simulations involving: (1) a single particle levitated above a wall, (2) two particles below a wall, and (3) two particles confined between two parallel walls. By specifying only repulsive electrostatic DLVO (Derjaguin-Landau-Verwey-Overbeek) potentials and including multi-body hydrodynamics, we successfully recover expected potentials in some cases, while anomalous attraction is observed in other cases. Attraction inferred in the latter simulations displays quantitative agreement with literature measurements when particle dynamics are interpreted using reported analyses. Because anomalous attraction is reproduced in simulations using only electrostatic repulsive DLVO potentials, our results reveal the one-dimensional analyses to be invalid for configurations that are inherently multi-dimensional via multi-body hydrodynamics. Parameters related to experimental sampling of particle dynamics are also found to be critical for obtaining accurate potentials. We explain the anomalous attraction in each experiment using effective potentials, which can be employed in an *a priori* fashion to assist the confident design of

future experiments involving interfacial and confined colloids. Ultimately, our findings reveal the importance of dimensionality and multi-body hydrodynamics for understanding non-equilibrium dynamics of colloids near surfaces.

4.2. Introduction

In this section, we report results from Stokesian Dynamics simulations of experiments involving either one or two colloids near a single wall or confined between two parallel walls. By considering multi-body hydrodynamic interactions in interfacial and confined colloidal systems, we are able to fully account for observations of anomalous attraction in both previously reported[50] and newly proposed experiments involving colloidal pairs near a single wall. In experiments involving like charged particle pairs confined between like charged walls,[30] we capture some features of previously reported anomalous potentials, but fall short of quantitatively reproducing experimental measurements. In each case, we reproduce anomalous attraction by considering only repulsive electrostatic DLVO (Derjaguin-Landau-Verwey-Overbeek)[51] potentials and multi-body hydrodynamics in our simulations of particle dynamics, which we interpret using analyses identical to the original references.[52] We derive effective potentials to quantitatively account for the anomalous attraction in each simulation using an approach analogous to that used in previous work by Squires and Brenner.[31,53] Our modified potentials provide some qualitatively new conclusions and a clarification of anomalous attraction. From both our simulated and analytical results, we show that accurate treatment of the multi-body mobility tensor and its gradient is essential for

interpreting conservative colloidal potentials from non-equilibrium particle dynamics near boundaries.

Understanding multi-body hydrodynamics and colloidal potentials in interfacial and confined geometries is crucial to numerous scientific and technological applications involving nano- and micro- particles. Colloidal force measurement techniques such as Total Internal Reflection Microscopy[54] depend on the ability to rigorously interpret both equilibrium interactions due to conservative potential fields and non-equilibrium interactions due to dissipative hydrodynamic forces.[55] Development of new colloidal force measurement techniques requires expanding our understanding from single particle-wall measurements to interpret interactions in increasingly concentrated, multi-dimensional colloidal systems.[56] Interfacial self assembly requires the ability to simultaneously manipulate colloidal forces and hydrodynamic interactions that control the thermodynamics and kinetics of structure formation on surfaces.[57] Colloidal epitaxy on templated substrates[58,59] is a specific case where both particle-particle and particle-wall conservative and dissipative interactions need to be manipulated to design robust colloidal crystal fabrication processes. Understanding interfacial particle and substrate interactions is crucial to complex fluid and advanced material technologies that involve, for example, film formation,[60] particle deposition in porous media, and protein interactions at cell surfaces.

Our results in this section are aimed at addressing the long standing controversy surrounding anomalous attraction between like-charged particles near like-charged interfaces. To the authors' knowledge, the paper of Ise et.al.[61] was one of the first to

report stable voids in dispersions of like charged particles near a like charged interface *and* attribute their formation to long range attraction between like charged particles. Anomalous attraction has more recently been inferred from measurements of the equilibrium structure of low density interfacial ensembles[62,63] and non-equilibrium trajectories of particles periodically trapped and released by blinking optical tweezers near one or two walls.[30,50] Recent inferences of attraction in equilibrium measurements of non-aqueous charged colloids may represent yet another case due to the importance of multi-body electrostatic interactions.[64,65] These observations are often collectively interpreted to suggest a lack of universality of the classic DLVO theory when applied to charged colloids near interfaces and in confinement. Although Squires and Brenner[31,53] previously identified the role of multi-body hydrodynamics in the apparent attraction between two like charged particles falling below a nearby wall, many inferences of anomalous interactions from both equilibrium and non-equilibrium measurements remain unexplained.

In the following, we investigate the validity of a one-dimensional transition probability analysis for interpreting conservative colloidal potentials from Stokesian Dynamics simulations of particle trajectories near wall surfaces. Using only DLVO potentials[51] and established models for multi-body hydrodynamics,[2,22,42] we present particle-particle and particle-wall potentials interpreted from particle dynamics in simulations involving: (1) a single particle levitated above a wall, (2) two particles below a wall, and (3) two particles confined between two parallel walls. After verifying the one-dimensional analysis for interpreting interactions between a single levitated

particle and wall, we demonstrate the validity of the analysis for particle pairs far from any walls. We then show that for particle pairs near a single wall the correct particle-wall interaction appears to be obtained, but an anomalous particle-particle attraction is inferred that is indistinguishable from literature measurements. The one-dimensional analysis fails in this case because it does not properly consider multi-body hydrodynamics that are inherently multi-dimensional. By deriving effective potentials that rigorously consider the multi-body mobility tensor *and* its gradient, we quantitatively predict anomalous attraction in several new interfacial colloid experiments that are unexplained by previous analyses. In particular, we describe and explain anomalous attraction inferred for both (1) like charged particles interacting adjacent to an uncharged wall, and (2) like charged particles interacting with a like charged wall in the presence of a nearby like charged particle. We also discuss how effective potentials can be used in an *a priori* fashion to confidently interpret colloidal dynamics in future experiments. Finally, we report anomalous interactions for like charged pairs confined between like charged parallel walls, which exhibit some features of previously reported experimental potentials[30] but also fail to capture several important characteristics. Ultimately, these results allow us to discuss both the validity of the DLVO theory and the importance of multi-body hydrodynamics for understanding non-equilibrium dynamics of interfacial and confined colloids.

4.3. Equation of Motion

To compute particle trajectories as a function of time, we recall the configuration propagation equation from Section 2 as

$$\mathbf{r} = \mathbf{r}^0 + k_B T\left(\nabla\cdot\left(\mathbf{R}^0\right)^{-1}\right)\Delta t + \left(\mathbf{R}^0\right)^{-1}\cdot\mathbf{F}^{P,0}\Delta t + \mathbf{X}^0\left(\Delta t\right) \tag{4.1}$$

where the different variables have been defined earlier. Eq. (4.1) is used to generate particle configurations as a function of time.

4.4. Colloidal and External Force Fields

For the experiments investigated in this section (see fig. 4.1), the net force due to conservative potential fields includes interactions between electrostatic double layers on charged particles and surfaces and the gravitational body force acting on each particle given as,

$$\mathbf{F}^P = \mathbf{F}_{edl}^{pp} + \mathbf{F}_{edl}^{pw} + \mathbf{F}^{grav} \tag{4.2}$$

For particle-particle surface separations larger than the Debye length (h-a>κ^{-1}), but smaller than the sphere radius (h-a<a), the interaction of electrostatic double layers on adjacent particles, $F_{edl}(r)$, for 1:1 electrolytes is given using the superposition and Derjaguin approximations as,[34]

$$F_{edl}^{pp}\left(r\right) = 32\pi\varepsilon\kappa a\left(\frac{k_B T}{e}\right)^2 \tanh\left(\frac{e\psi_{p1}}{4k_B T}\right)\tanh\left(\frac{e\psi_{p2}}{4k_B T}\right)\exp\left[-\kappa\left(r-2a\right)\right] \tag{4.3}$$

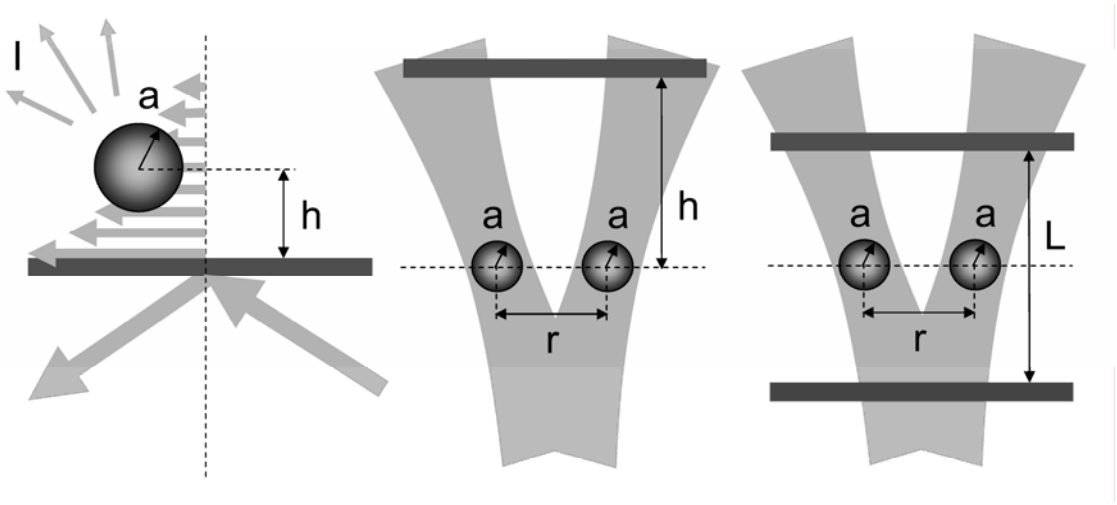

(a) (b) (c)

Figure 4.1. Schematic representations of experiments involving: (a) a single levitated colloidal particle interacting with a wall as in typical TIRM measurements, (b) intermittent sedimentation of colloidal pairs below a wall using a blinking optical tweezer,[50] and (c) two colloidal particles confined between two parallel walls using blinking optical tweezers.[30]

whereas, for particle-particle surface separations greater than the Debye length (h-a>κ^{-1}), but also greater than the sphere radius (h-a>a), the interaction of electrostatic double layers, $F_{edl}(r)$, is given for 1:1 electrolytes by the linear superposition approximation as,[34]

$$F_{edl}^{pp}(r) = 4\pi\varepsilon a^2 \left(\frac{k_B T}{e}\right)^2 \left(\frac{e\psi_{p1}}{k_B T}\right)\left(\frac{e\psi_{p2}}{k_B T}\right)\left(\frac{1+\kappa r}{r^2}\right)\exp\left[-\kappa\left(r-2a\right)\right] \qquad (4.4)$$

where ε is the dielectric permittivity of water, a is particle radius, k_B is Boltzmann's constant, T is absolute temperature, e is the elemental charge, values of ψ are the Stern potentials of the particles or wall, and r is center-to-center particle separation. The

particle-wall electrostatic interaction is given for each case by multiplying the particle-particle interaction by 2, which results from using the Derjaguin approximation. The Debye screening length, κ, is,

$$\kappa = \sqrt{\frac{2CN_A e^2}{\varepsilon k_B T}} \tag{4.5}$$

where C is the bulk solution ionic strength. The gravitational body force acting on each particle is given in terms of the buoyant particle mass, m, which can be expressed in terms of particle and fluid densities, ρ_p and ρ_f, and the acceleration due to gravity, g, as,

$$F^{grav} = mg = (4/3)\pi a^3(\rho_p - \rho_f)g \tag{4.6}$$

4.5. Equilibrium Pair Interactions from Transition Probability Analysis

The configuration of the N-particle colloidal system can be represented by the N-particle configuration-space distribution function, $g(\mathbf{r})$. The evolution of the N-particle distribution function is given by the N-body Smoluchowski equation,[66]

$$\frac{\partial g(\mathbf{r})}{\partial t} - \nabla \cdot \left[\left(\mathbf{R}^{-1} \right) \cdot \left(k_B T \nabla - \mathbf{F}^P \right) g(\mathbf{r}) \right] = 0 \tag{4.7}$$

where $\mathbf{R}$ is the hydrodynamic resistance tensor, and $\mathbf{F}^P$ is the total conservative force. For equilibrium conditions, eq. (4.7) can be solved to obtain an equilibrium distribution function related to particle pair interactions in dilute systems given by Boltzmann's equation as,

$$g(\mathbf{r}) = \exp\left(-\phi(\mathbf{r}) / k_B T \right) \tag{4.8}$$

For a one-dimensional system, equation (4.7) can be written as,[67]

$$\frac{\partial g(r)}{\partial t} - \frac{\partial}{\partial r}\left[M(r)\left(\phi'(r) + k_B T \frac{\partial}{\partial r} \right) g(r) \right] = 0 \tag{4.9}$$

where $M(r)$ is the hydrodynamic mobility coefficient. Propagation of the one-dimensional distribution function can be written using a transition probability tensor as,

$$g(r + \Delta r, t + \Delta t) = \int P(r + \Delta r, t + \Delta t \mid r, t)\, g(r, t)\, dr \tag{4.10}$$

The equilibrium distribution function can be obtained as a stationary solution of eq. (4.10) even for non-equilibrium conditions.

Particle trajectories obtained from simulations in this study are analyzed using the method of Crocker and Grier,[52] which we briefly summarize here. Pairs of particle coordinates are monitored at a specified time interval, Δt, and their projected one-dimensional center-to-center distance, r, is determined. In consecutive time steps, the separation vector of the sphere pair changes from an initial vector $\mathbf{r}_0$ to a final vector $\mathbf{r}_f$. The final separation vector is projected onto the initial separation vector. The initial separation $|\mathbf{r}_0|$ and the projected final separation $|\mathbf{r}_0 \cdot \mathbf{r}_f|$ are distributed into a transition probability tensor, P. The tensor P is constructed such that columns indicate initial separations and rows indicate final projected separations, i.e. P_{ij} denotes the probability of a transition in particle separation from r_j to r_i in a time step Δt. The transition tensor is related to the equilibrium pair distribution function $g(r)$ by,[67]

$$g_i^{eq} = \sum_j P_{ij} g_j^{eq} \tag{4.11}$$

Table 4.1. Simulation and sampling parameters for constructing the transition probability tensor in each experiment.

	TIRM	LG	CG
simulation step (ms)	0.1	0.1	0.1
frame interval (ms)	16.67	16.67	16.67
total cycles	na	5000	10000
frames/cycle	na	6	6
total points	250000	20000	40000
total time (min)	69.5	11.1	22.2

which is a discretized version of eq. (4.10). Eq. (4.11) is an eigenvalue problem where the eigenvector corresponding to an eigenvalue of 1 is the equilibrium pair correlation function g^{eq}. Once the pair correlation function is known, the pair potential $\phi(r)$ is obtained using Boltzmann's equation in eq. (4.8).

4.6. Results and Discussion

4.6.1. Levitation of a single charged colloid above a charged wall

The simplest interfacial particle experiment that we investigate is for a single colloid of radius, a, levitated above a flat wall with a one-dimensional center-to-wall distance, h, as shown in fig. 4.1a. This is the arrangement used in the Total Internal Reflection Microscopy (TIRM) technique developed by Prieve and co-workers[54] for measuring particle-wall interactions on the order of k_BT. In a typical TIRM experiment, particle surface-to-wall separation, h-a, is dynamically measured from particle scattering intensity, I, in an evanescent wave. To model height excursions of a single levitated colloid in a typical TIRM experiment, three dimensional Stokesian Dynamic (SD)

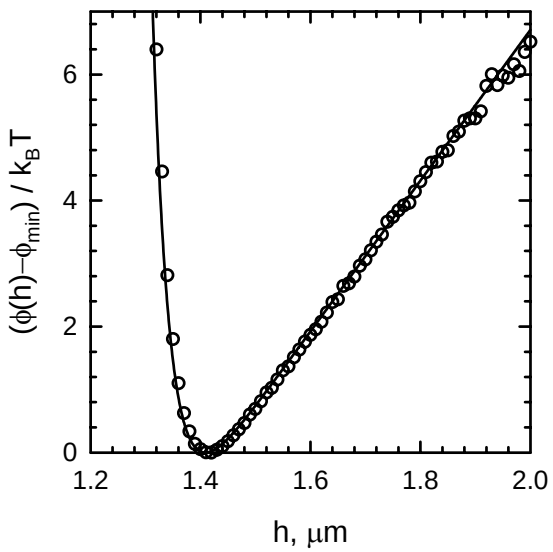

Figure 4.2. Particle-wall potential energy profile for a single 2.2 μm silica colloid (ρ_p=2150 kg/m^3, ψ_p=-50 mV) electrostatically levitated above a glass microscope slide (ψ_w=-50 mV) in a 0.1 mM (κ^{-1}=30 nm) 1:1 aqueous electrolyte solution (ρ_f = 1000 kg/m^3) (see fig. 4.1a). The solid line is the total potential specified in the simulation.

simulations were implemented to include coupled hydrodynamic and Brownian forces in addition to conservative electrostatic (eq. (4.3)) and gravitational forces. A simulation time step of 0.1 ms was used in the equation of motion (eq. (4.1)) as reported in Table 4.1. To interpret particle-wall interactions, we use a non-equilibrium transition probability analysis,[68] which contrasts the standard TIRM analysis of equilibrium height distributions.[54] This experiment demonstrates the measurement of single particle-wall interactions from dynamic height excursions, which we use in all subsequent experiments.

Fig. 4.2 shows a potential energy profile for a single 2.2 μm silica colloid (ρ_p=2150 kg/m^3, ψ_p=-50 mV) electrostatically levitated above a glass microscope slide

(ψ_w=-50 mV) in 0.1 mM (κ^{-1}=30 nm) ionic strength aqueous media (ρ_f=1000 kg/m^3). Open circles in fig. 4.2 were obtained by analyzing the particle's height excursions above the glass surface using the transition probability analysis in eqs. (4.8) and (4.11). The transition probability tensor was constructed from data acquired with the sampling parameters summarized in Table 4.1 which are comparable to typical values used in TIRM experiments[69] and a previous Brownian Dynamics simulation.[70] The solid line in fig. 4.2 is the theoretical potential energy profile corresponding to the net electrostatic and gravitational potentials specified in the SD simulation (eq. (4.2)).

Excellent agreement is observed in fig. 4.2 between the potential energy profile obtained using the transition probability analysis and the potential energy profile originally specified in the SD simulation. In addition, an autocorrelation function and mean squared displacement of the single particle's normal and lateral fluctuations indicate the correct average hindered particle diffusion coefficients ($D_\perp/D_0$=0.23, $D_\parallel/D_0$=0.56).[55] Agreement between simulated and interpreted equilibrium potential profiles and particle dynamics verifies the accurate and consistent treatment of the single particle-wall TIRM experiment in our SD simulation. The results in fig. 4.2 also demonstrate the utility of the transition probability analysis for quantitatively recovering the particle-wall potential from a single particle's dynamic trajectory adjacent to a wall. This result provides an important foundation before proceeding to characterize both particle-wall and particle-particle interactions in experiments involving more than one particle.

4.6.2. Intermittent sedimentation of two charged colloids below a charged wall

To incrementally increase both experimental and theoretical complexity, fig. 4.1b shows two particles of radius, a, held below a plane wall at a center-to-wall distance, h, and a projected one-dimensional center-to-center distance, r, by a pair of optical traps periodically blocked by a beam chopper. Particle separation, r, is continuously adjusted during the experiment via the optical tweezer to evenly sample a specified range. Values of h correspond to the "trapped" state (unblocked tweezers), while trajectory data are examined only during the "released" state (blocked tweezers) during which time all three dimensions are sampled via Brownian motion. This experimental configuration was previously reported by Larsen & Grier (LG) to measure lateral interactions between negatively charged colloids below a negatively charged wall.[50] In the original LG experiment, the projected center-to-center separation, r, was dynamically measured using video microscopy,[71] while particle center-to-wall separation, h, was not monitored. As in the TIRM experiment in fig. 4.2, SD simulations of the LG experiment were implemented to include coupled hydrodynamic and Brownian forces in addition to conservative electrostatic (eq. (4.4)) and gravitational forces. An important contribution in the three-body LG experiment is the multi-body resistance tensor, $\mathbf{R}$, which occurs in the SD equation of motion (eq. (4.1)).

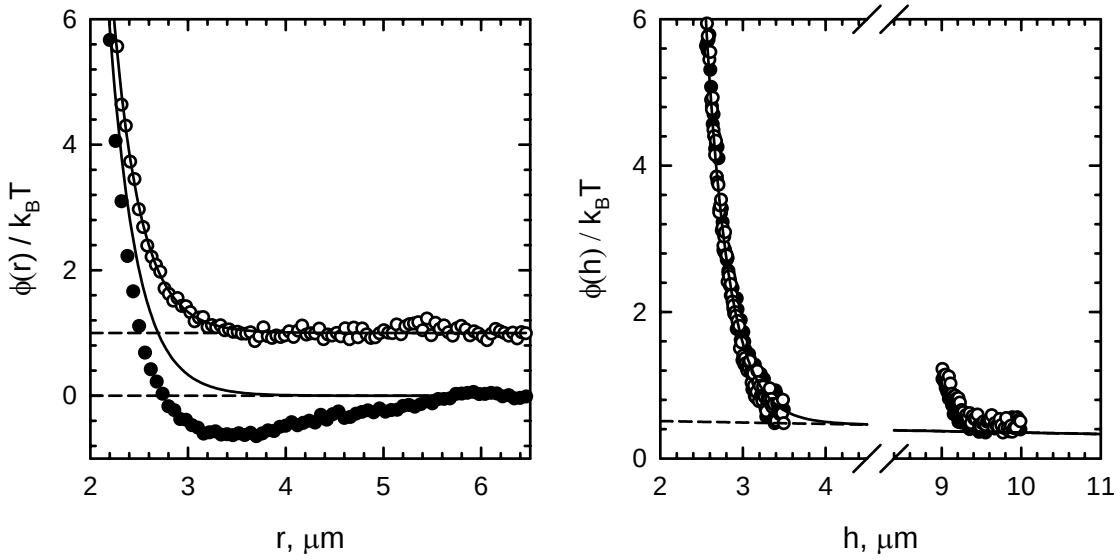

Figure 4.3. Potential energy profiles for the interaction of two 652 nm polystyrene (PS) colloids (ρ_p=1055 kg/m^3, ψ_p=-178 mV) below a glass microscope slide (ψ_w=-71 mV) in a 0.0012 mM (κ^{-1}=275 nm) 1:1 aqueous electrolyte solution (ρ_f = 1000 kg/m^3) (see fig. 4.1b). Particle-particle interactions are reported in (a) where filled circles correspond to h=2.5 μm and open circles correspond to h=9.5 μm. Particle-wall interactions are reported in (b) where filled circles correspond to particle 1 and open circles correspond to particle 2. The solid lines are the DLVO interactions specified in the simulation.

Fig. 4.3a shows potential energy profiles for the interaction of two 652 nm polystyrene (PS) colloids (ρ_p=1055 kg/m^3, ψ_p=-178 mV) below a glass microscope slide (ψ_w=-71 mV) in 0.0012 mM (κ^{-1}=275 nm) ionic strength aqueous media (ρ_f =1000 kg/m^3). Data in fig. 4.3a are determined from a transition probability analysis of projected particle separations, r, in planes at either h = 9.5 μm (open circles) or h = 2.5 μm (closed circles) parallel to the glass slide surface. The transition probability tensor in each case was constructed using data acquired with the same parameters as the original

LG experiment,[50] which are summarized in Table 4.1. The two profiles are intentionally offset by 1 k_BT for clarity. The solid lines in fig. 4.3a are the particle-particle electrostatic repulsion specified in the SD simulation (eq. (4.2)).

While excellent agreement is observed in fig. 4.3a between the specified theoretical profile and the particle pair interaction for h = 9.5 μm, an apparently anomalous attractive well of ~0.75 k_BT at $r \approx 10a$ is observed for the experiment at h = 2.5 μm. Both results in fig. 4.3a are essentially identical to the experimental LG results.[31,50] Of course, the apparent attraction is unexpected because all particle and wall surfaces bear negative charges. The observed attraction is particularly surprising in this work since only repulsive electrostatic DLVO pair interactions are specified in the SD simulation. Because the transition analysis which worked for the TIRM experiment in fig. 4.2 now fails to recover the known interactions specified in the simulation, an immediate conclusion is that the analysis is either inappropriate or incorrectly applied in the experiment in fig. 4.3.

Before further discussing the anomalous particle-particle attraction in fig. 4.3a, we also report particle-wall interactions from our simulation of the LG experiment in fig. 4.3b. Profiles in fig. 4.3b were constructed using the same trajectory data as in fig. 4.3a, except each particle's height excursions normal to the glass surface were interpreted in an analysis identical to the TIRM experiment in fig. 4.2. Circles in fig. 4.3b represent the interpreted interaction potential for each particle with the wall, and the solid line is the electrostatic repulsion specified in the simulation (eq. (4.2)). Excellent agreement is observed in fig. 4.3b between measured and specified profiles for both h = 2.5 μm and h

= 9.5 μm. A small upturn in the particle-wall interaction for h <9.2 μm is probably due to poor statistical sampling of the transition probability tensor, which we discuss later in more detail. Because the specified particle-wall potentials are successfully recovered in fig. 4.3b, it appears the transition probability analysis is at least approximately valid in the particle-wall case despite its apparent failure to recover particle-particle interactions from the same trajectory data in fig. 4.3a.

To fully understand all relevant interactions in the LG experiment, it is clear that a consistent explanation of the potentials in fig. 4.3 must simultaneously account for both the apparent particle-particle attraction and the DLVO particle-wall repulsion. Because the expected DLVO particle-particle potential is recovered for the h = 9.5 μm case in fig. 4.3a, which is consistent with previous measurements far from boundaries,[52] simple reasoning suggests the anomalous attraction in the h = 2.5 μm case is induced by the nearby wall.[50] The role of the wall was indeed identified as the primary cause of the apparent attraction by Squires & Brenner (SB) using a "non-equilibrium hydrodynamic" explanation, as opposed to a novel conservative potential field.[31] Although SB identified the importance of hydrodynamic phenomena in the LG experiment, we demonstrate in the following that more rigorous computation of the multi-body mobility tensor *and* inclusion of its gradient results in a modified explanation of the LG experimental results. In addition, we provide some qualitatively new conclusions with regards to inferences of anomalous attraction in several new experiments involving non-equilibrium measurements of interfacial colloidal dynamics.

Before proceeding with a quantitative analysis, we first offer a clarification concerning the nature of the anomalous attraction inferred in fig. 4.3a. The fundamental explanation for the anomalous attraction in the LG experiment is that the one-dimensional analysis in eqs. (4.8) and (4.11) is not valid for the conditions of this particular experimental configuration (see fig. 4.1b). Analyzing projected one-dimensional particle displacements, Δr, during a time interval, Δt, based on the one-dimensional Smoluchowski equation (eq. (4.9))[72] does not correctly treat *multi-body* hydrodynamic interactions that are also inherently *multi-dimensional*. In other words, particle excursions in the LG experiment are affected by three-dimensional dissipative interactions that are not consistently treated using a one-dimensional transition probability analysis. Although correct interactions might be obtained by considering propagation of the three dimensional distribution function, $g(\mathbf{r})$, in the general N-particle Smoluchowski equation (eq. (4.7))[66] using a transition probability approach,[73] such an analysis is beyond the scope of this work. The underlying problem with using the one-dimensional analysis in the LG experiment is that it does not consistently treat one-dimensional, pairwise conservative and multi-dimensional, multi-body dissipative forces.

4.6.3. Effective potential for the interaction of two charged colloids below a charged wall

By recognizing the importance of dimensionality in problems involving multi-body hydrodynamics, it is possible to develop *a priori* criteria for determining the applicability of the one-dimensional transition probability analysis for interpreting non-

equilibrium particle dynamics at interfaces. By deriving "effective potentials" that quantitatively capture the anomalous attraction in our simulated results, we obtain a general and reliable method for predicting the validity of the one-dimensional analysis for interpreting "true" particle potentials from measured particle dynamics without their prior knowledge.

Here we essentially follow the framework for deriving effective potentials developed by SB,[31,53] except we consider a more rigorous mobility tensor and include the spatial gradient of the mobility tensor in our equations of motion. The importance of the gradient of the mobility tensor in Brownian dynamics simulations is reported in the classic work of Ermak and McCammon,[74] and is discussed in detail by Grassia et. al.[47] To quantitatively predict the anomalous attraction in fig. 4.3a, we begin by writing a one-dimensional, two-body equation of motion that would describe the projected one-dimensional displacements observed in our simulations if multi-body, multi-dimensional hydrodynamic interactions were not important. This can be written using an effective particle-particle force, F^{eff}, as,

$$\Delta r = 2\left(M^{2B}_{x_1x_1} - M^{2B}_{x_1x_2}\right)F^{eff}\frac{\Delta t}{k_BT} + 2\left(\frac{\partial M^{2B}_{x_1x_1}}{\partial r} - \frac{\partial M^{2B}_{x_1x_2}}{\partial r}\right)\Delta t \qquad (4.12)$$

where M's are components of the two-body mobility tensor, $\mathbf{M}^{2B}$, which were calculated using the exact expression.[40] The subscripts on the mobility terms indicate how each coefficient relates particle hydrodynamics and forces; M_{x1x1} is the mobility of particle 1 in the x direction due to forces on particle 1 in the x direction, and M_{x1x2} is the mobility of particle 1 in the x direction due to forces on particle 2 in the x direction. The

Brownian term is excluded from eq. (4.12) because it produces no net displacement on average. We include the gradient of the mobility tensor from eq. (4.1), which has not been previously considered with regard to the LG experiment. The factor of "2" in eq. (4.12) accounts for both particle displacements (see fig. 4.1b).

However, the three-dimensional equation of motion in eq. (4.1) used in our SD simulations, can also be simplified to write an approximate equation of motion for projected one-dimensional displacements in terms of DLVO particle-particle, F^{pp}, and particle-wall, F^{pw}, interactions, and the multi-body diffusion tensor as,

$$\Delta r = 2\left(M_{x_1x_1} - M_{x_1x_2}\right)F^{pp}\frac{\Delta t}{k_BT} + 2M_{x_1z_2}\left\langle F^{pw}\right\rangle\frac{\Delta t}{k_BT} + 2\left(\frac{\partial M_{x_1x_1}}{\partial r} - \frac{\partial M_{x_1x_2}}{\partial r}\right)\Delta t \quad (4.13)$$

where M's are now components of the multi-body mobility tensor, $\mathbf{M} = \mathbf{R}^{-1}$, which were calculated using the method of Brady and Bossis[2] as summarized in section 2. The multi-body term M_{x1z2} is the mobility of particle 1 in the x direction due to forces on particle 2 in the z direction, which accounts for three-body hydrodynamic interactions. This term is calculated more rigorously compared to previous approximate treatments.[75] Because particles experience Brownian excursions normal to the wall, the average particle-wall interaction is used in eq. (4.13) as denoted by the brackets. Because eqs.. (4.12) and (4.13) are expected to both produce the same projected one-dimensional particle displacements, which was confirmed in one-dimensional dynamic simulations, it is reasonable to equate them and integrate to obtain an effective potential as,

$$U_{eff}^{pp}(r,h) = -\int_r^\infty \left(\frac{M_{x_1x_1} - M_{x_1x_2}}{M_{x_1x_1}^{2B} - M_{x_1x_2}^{2B}} \right) F^{pp}(r)\,dr - \left\langle F^{pw}(h) \right\rangle \int_r^\infty \left(\frac{M_{x_1z_2}}{M_{x_1x_1}^{2B} - M_{x_1x_2}^{2B}} \right) dr$$
$$- k_B T \int_r^\infty \frac{\left(\frac{\partial M_{x_1x_1}}{\partial r} - \frac{\partial M_{x_1x_2}}{\partial r} \right) - \left(\frac{\partial M_{x_1x_1}^{2B}}{\partial r} - \frac{\partial M_{x_1x_2}^{2B}}{\partial r} \right)}{M_{x_1x_1}^{2B} - M_{x_1x_2}^{2B}} dr \qquad (4.14)$$

where the relative magnitude of particle-wall interactions, F^{pw}, and multi-body mobility terms and their gradients determine the degree to which relative one-dimensional particle motion is perturbed by the wall, which accounts for the resulting apparent deviation from the DLVO particle-particle potential.

Fig. 4.4a replots our simulated potential for h=2.5 μm from fig. 4.3a along with the effective potential predicted by eq. (4.14) as the dashed line. Excellent agreement is obtained between predicted and measured potentials both in magnitude and range. Eq.. (4.14) also predicts the simulated potential in fig. 4.3a for h=9.5 μm with equal accuracy because the second and third terms vanish, and the first coefficient is unity, so the effective potential reduces to the predicted DLVO interaction. These results illustrate that eq. (4.14) quantitatively describes particle pair interactions both near and far from walls by including the rigorous many-body mobility tensor *and* its gradient in the equation of motions in eqs. (4.12) and (4.13). By determining whether relevant terms have non-zero or non-unity values, the effective potential in eq. (4.14) can also be used in an *a priori* fashion to predict whether a one-dimensional analysis is expected to yield the correct pair interactions in experiments involving interfacial and confined colloids. This knowledge is essential for confidently designing and interpreting experiments,

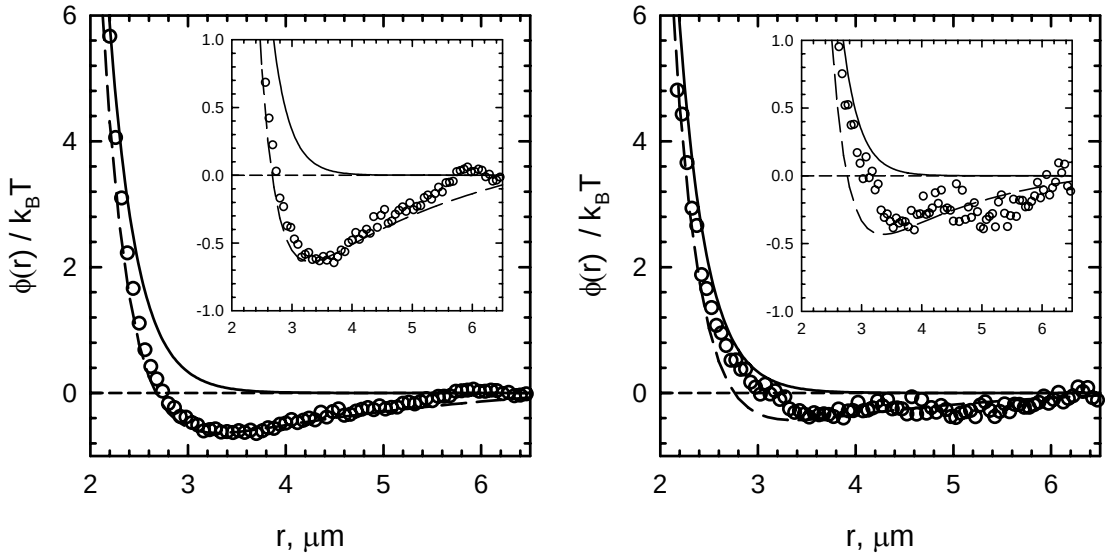

Figure 4.4. (a) Particle-particle potential energy profile replotted from fig. 4.3a for h=2.5 μm. (b) Particle-particle potential energy profile for the interaction of two 652 nm polystyrene (PS) colloids (ρ_p=1055 kg/m^3, ψ_p=-178 mV) below an uncharged wall (ψ_w=0 mV) in a 0.0012 mM (κ^{-1}=275 nm) 1:1 H_2O/D_2O electrolyte solution (ρ_f = 1055 kg/m^3) (see fig. 4.1b). Circles correspond to interpreted simulation data, the solid line is the DLVO particle interaction specified in the simulation, and the dashed lines are analytical effective potentials given by eq. (4.14). Insets show magnification of each potential energy profile's minimum region.

particularly if the one dimensional analysis is intended as a reliable measurement tool in poorly understood systems.

The expression in eq. (4.14) is different from the effective potential derived by SB. Different terms are present in our effective potential because we distinguish between two-body and multi-body mobility tensors in eqs. (4.12) and (4.13) and include the gradient of the mobility tensor (see eq. (4.1)). The net attraction in Fig 4a is quantitatively captured only when all these terms are included in eq. (4.14). The

additional terms in our effective potential predict qualitatively different results in several new illustrative experiments described in the following sections.

4.6.4. Intermittent sedimentation of two charged colloids below an uncharged wall

To demonstrate the importance of the terms in eq. (4.14) in addition to the one involving repulsive particle-wall interactions, we present simulations of an experiment similar to the LG experiment except the wall is uncharged and the particles are neutrally buoyant (see fig. 4.1b). This arrangement is a good approximation of experiments involving non-ionic polymer films with negligible surface potentials and polystyrene particles density matched in H_2O/D_2O media. Fig. 4.4b shows a potential energy profile for the interaction of two 652 nm PS colloids (ρ_p=1055 kg/m^3, ψ_p=-178 mV) below an uncharged wall (ψ_w=0 mV) in 0.0012 mM (κ^{-1}=275 nm) ionic strength H_2O/D_2O media (ρ_f=1055 kg/m^3). Our SD simulations of this experiment include coupled hydrodynamic and Brownian forces and conservative electrostatic forces.

Data in fig. 4.4b are from a transition probability analysis of one-dimensional particle separations, r, in a plane at h = 2.5 μm parallel to the wall surface using identical parameters to the LG experiment in Table 4.1. As in fig. 4.4a, the solid line shown in fig. 4.4b is the electrostatic repulsion specified in the SD simulation (eq. (4.2)), which is the same for both experiments. An anomalous attractive well of ~0.4 k_BT is observed at $r \approx 10a$ in fig. 4.4b, which is similar in range to the LG experiment in fig. 4.4a, but approximately half the depth. Because the particle-wall interaction is identically zero for separations sampled in the vicinity of the trapped position at h = 2.5 μm, the anomalous

attraction in fig. 4.4b cannot be accounted for by the spheres' net drift away from the wall and their "coupling" via three-body hydrodynamics.[31] The particles were made neutrally buoyant (F_g=0) so that gravitational forces normal to the wall are not present (although gravitational forces were also found to be insignificant in this experiment without density matching).

The anomalous attraction in fig. 4.4a is well described by the dashed line given by eq. (4.14), with contributions only from the terms involving the gradient of the mobility tensor and differences in two- and three- body mobility tensor terms. Because this experiment is nearly identical to the LG experiment except for the uncharged wall, it is clear that these additional terms account for approximately half of the anomalous attraction in the LG experiment in fig. 4.4a. Both of the results in fig. 4.4 together illustrate that even in a simple two particle-wall experiment, only a rigorous treatment of multi-body hydrodynamics in conjunction with an accurate equation of motion including the gradient of the mobility tensor is sufficient to generate quantitative agreement between theoretical predictions and experimental measurements.

4.6.5. Effective potentials for charged colloids interacting with a charged wall

Although the anomalous particle-particle attraction in the LG experiment in fig. 4.3a is now fully accounted for, it is less obvious why the correct particle-wall interaction was obtained in the same experiment in fig. 4.3b. To examine in more detail the influence of multi-body hydrodynamics on the interpretation of particle-wall interactions, we present simulations of yet another variation of the LG experiment involving two 652 nm PS particles held below a charged wall at h = 2.5 μm and r = 2.5

μm by a pair of optical traps periodically blocked by a beam chopper (see fig. 4.1b). By maintaining the particle pair at both relatively small particle and wall separations, multi-body hydrodynamics are expected to have a greater effect on particle-wall interactions compared to the experiment in fig. 4.3b in which particle separation was continuously adjusted between r = 2.0-6.5 μm. This experimental arrangement could be realized in future measurements of particle-wall interactions involving two or more particles in a multi-trap optical tweezer.

Fig. 4.5 shows a potential energy profile for the interaction of two 652 nm PS colloids (ρ_p=1055 kg/m^3, ψ_p=-178 mV) below a charged wall (ψ_w=-71 mV) in 0.0012 mM (κ^{-1}=275 nm) ionic strength aqueous media (ρ_f=1000 kg/m^3). Because the optical trap position is unchanged during the experiment, height excursions used to construct the transition probability tensor arise only from Brownian motion about the trapped position at h = 2.5 μm and r = 2.5 when the particle pair is periodically released from the optical tweezer. Data in fig. 4.5 are determined from a transition probability analysis of one-dimensional particle-wall separation, h, as in the TIRM experiment in fig. 4.2. The transition probability tensor in each case was constructed using the same parameters as the LG experiment listed in Table 4.1. The solid line in fig. 4.5 is the particle-wall electrostatic and gravitational interaction specified in the SD simulation (eq. (4.2)).

When using the same analysis as in the TIRM experiment in fig. 4.2, the data in fig. 4.5 display an anomalous attractive well of ~1 k_BT at $h \approx 10a$, which is of course unexpected. We again explain this anomalous attraction in terms of an effective potential. In a derivation paralleling our analysis of particle-particle interactions near a

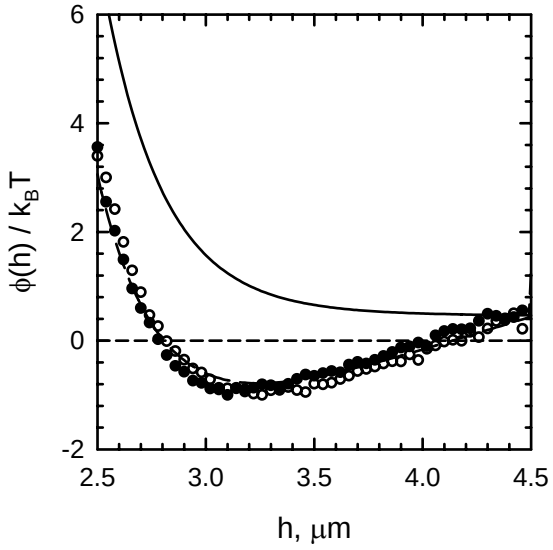

Figure 4.5. Particle-wall potential energy profiles for two 652 nm PS colloids (ρ_p=1055 kg/m^3, ψ_p=-178 mV) held at h=2.5 μm and r=2.5 μm below a negatively charged wall (ψ_w=-71 mV) in a 0.0012 mM (κ^{-1}=275 nm) 1:1 aqueous electrolyte solution (ρ_f = 1000 kg/m^3) (see fig. 4.1b). Filled circles correspond to particle 1 and open circles correspond to particle 2. The solid line is the DLVO particle interaction specified in the simulation, and the dashed line is the analytical effective potential given by eq. (4.15).

wall in eqs. (4.12)-(4.14), and similar to the method originally implemented by SB, it is easy to show the effective potential for the particle-wall interaction is given by,

$$U_{eff}^{pw}(h,r) = -\int_h^\infty \frac{M_{z_1z_1} + M_{z_1z_2}}{M_{z_1z_1}^{2B}} F^{pw}(h)\,dh - \left\langle F^{pp}(r)\right\rangle \int_h^\infty \frac{M_{z_1x_1} - M_{z_1x_2}}{M_{z_1z_1}^{2B}} dh$$
$$- k_B T \int_h^\infty \frac{\left(\frac{\partial M_{z_1z_1}}{\partial h} + \frac{\partial M_{z_1z_2}}{\partial h}\right) - \frac{\partial M_{z_1z_1}^{2B}}{\partial h}}{M_{z_1z_1}^{2B}} dh \qquad (4.15)$$

where M's are components of two- and many- body mobility tensors calculated using the rigorous expressions described in section 2. M_{z1z1} is the mobility of particle 1 in the z

direction due to forces on particle 1 in the z direction, M_{z1z2} is the mobility of particle 1 in the z direction due to forces on particle 2 in the z direction, and M_{z1x2} is the mobility of particle 1 in the z direction due to forces on particle 2 in the x direction. Because particles experience Brownian excursions parallel to the wall, an average particle-particle interaction is used in eq. (4.15) as denoted by the brackets.

Excellent agreement is displayed in fig. 4.5 between the dashed line predicted by eq. (4.15) and the interpreted particle-wall potentials. Eq. (4.15) also predicts the simulated potential for the TIRM experiment in fig. 4.2 with equal accuracy, which illustrates the generality of this expression for understanding charged particles near charged surfaces for conditions when another charged particle is either nearby or far away. As in eq. (4.14), the success of eq. (4.15) originates from consideration of the rigorous many-body mobility tensor, the gradient of the mobility tensor, and the relative importance of multi-body hydrodynamics compared to two-body interactions. Again, by quantifying in eq. (4.15) whether relevant terms have non-zero or non-unity values, this expression can be used in an *a priori* fashion to predict whether the one dimensional transition probability analysis can be confidently used as an objective measurement tool in colloidal systems where potentials are unknown.

It is also important to clarify the apparent discrepancy between the particle-wall interactions reported for the similar experiments in figs. 4.3b and 4.5. While an anomalous attractive particle-wall potential was inferred in fig. 4.5, the expected DLVO particle-wall potential was recovered in fig. 4.3b, which suggests an important dependence on data sampling and averaging parameters when constructing transition

probability tensors. In fig. 4.5, particle and wall separations are essentially fixed at h = 2.5 μm and r = 2.5 μm, however, in fig. 4.3b, only particle-wall separation was fixed at h = 2.5 μm, but particle-particle separation was adjusted continuously between r = 2.0-6.5 μm. These results suggest that if particle dynamics were sampled only for r < 3.0 μm when constructing the transition probability tensor in fig. 4.3b, an anomalous particle-wall attraction would have been obtained similar to fig. 4.5. Because a significant portion of the measurement in fig. 4.3b was averaged over separations where particle-particle electrostatic and multi-body hydrodynamic interactions are not significant as determined from eq. (4.15), the average potential inferred in fig. 4.3b agrees well with the expected DLVO particle-wall interaction. These results indicate the importance of sampling statistics and averaging when constructing the transition probability tensor from measured particle dynamics. Although eqs. (4.14) and (4.15) capture deviations from DLVO potentials when the one-dimensional transition probability analysis is inappropriately applied to multi-dimensional dynamic data, the combined results in figs. 4.2, 4.3b, and 4.5 suggest that additional care must be taken when analyzing measurements averaged over different dynamic conditions.

4.6.6. Colloidal pairs confined at the mid-plane between parallel charged walls

So far we have considered interfacial colloids in close proximity to one wall, but have yet to examine confined colloidal systems. In this section, we build on our understanding of particle pairs near one wall to investigate the anomalous attraction inferred from non-equilibrium measurements of like-charged particle pairs confined at the mid-plane between parallel like-charged walls (see fig. 4.1c). Anomalous attraction

was originally reported for this particular experimental configuration by Crocker & Grier (CG) in 1996, but has eluded satisfactory explanation.[30,31] The experimental arrangement and procedure are similar to the LG experiment in fig. 4.1b, except that a second charged wall is added below the particle pair at a spacing L from the top wall as shown in fig. 4.1c. In the original CG experiment, projected center-to-center separation, r, was dynamically measured using video microscopy,[71] while particle center-to-wall separation, h, was not monitored. Our SD simulations of the CG experiment treat conservative and dissipative interactions similar to all previous experiments reported in this section (see eq. (4.1)).

Fig. 4.6a shows potential energy profiles for the interaction of two 652 nm PS colloids (ρ_p=1055 kg/m^3, ψ_p=-145 mV) at the mid plane between two charged walls (ψ_w=-58 mV) in 0.0012 mM (κ^{-1}=275 nm) ionic strength aqueous media (ρ_f =1000 kg/m^3). The walls are positioned at distances of L=6.5, 4.0, 3.0, and 2.5 μm as reported in a review article by Grier,[76] while all other parameters are the same as reported by CG.[30] Fig. 4.7 shows the particle-wall interaction for each of the four wall spacings investigated in fig. 4.6a. All particle-particle and particle-wall profiles in figs. 4.6a and 4.7 were constructed using the same particle trajectory data and the one-dimensional transition probability analysis in eqs. (4.8) and (4.11). Circles represent interpreted profiles, and solid lines are the electrostatic repulsion specified in the simulation (eq. (4.2)). Each potential profile in fig. 4.6a is intentionally offset by 2 or 3 k_BT for clarity, and the separation scale in fig. 4.7 is normalized by the wall spacing, L, for each

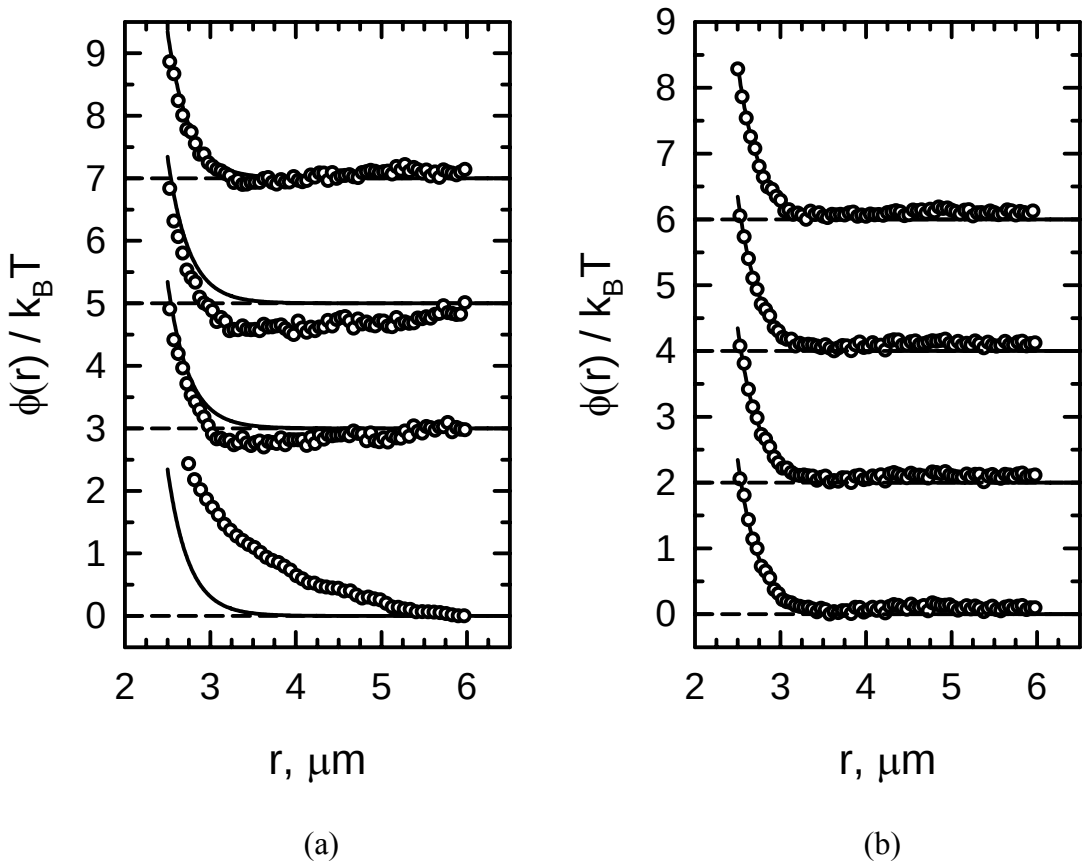

Figure 4.6. Particle-particle potential energy profiles for two 652 nm polystyrene (PS) colloids (ρ_p=1055 kg/m^3, ψ_p=-145 mV) at the mid plane between two charged walls (ψ_w=-58 mV) in a 0.0012 mM (κ^{-1}=275 nm) 1:1 aqueous electrolyte solution (ρ_f = 1000 kg/m^3) (see fig. 4.1c). Circles correspond to interpreted simulation data using either (a) 40,000 or (b) 80,000 sampled separations (see Table 4.1). From top to bottom in both (a) and (b), the wall separation as defined in fig. 4.1c is L=6.5, 4.0, 3.0, and 2.5 μm. Solid lines are the DLVO particle-particle interactions specified in the simulation.

experiment. The transition probability tensor was constructed using data acquired with the parameters reported in Table 4.1.

Excellent agreement is observed in fig. 4.7 between measured and specified particle-wall interactions at each wall separation. In addition, excellent agreement

between measured and specified particle-particle interactions is also obtained in fig. 4.6a for a wall spacing of L=6.5 μm. Because the expected potentials are recovered, the one-dimensional transition probability analysis appears to be at least approximately valid for interpreting particle-particle interactions for relatively large wall spacings (L/a = 6.5 μm/0.326 μm ≅ 20) and particle-wall interactions for all wall spacings examined here (L/a = 2.5-6.5 μm/0.326 μm ≅ 8-20). Although particle-wall interactions inferred at small particle-particle separations could be expected to predict anomalous attraction from eq. (4.15), no attraction is observed probably due to sampling and averaging effects similar to the particle-wall interaction obtained in the LG experiment in fig. 4.3b.

Results in fig. 4.6a also indicate anomalous attractive wells of ~0.4 k_BT and ~0.2 k_BT for L=4.0 and L=3.0 μm, while an anomalous long range repulsion is observed for L=2.5 μm. As in the previous experiments for particle pairs adjacent to a single wall in figs. 4.3-4.5, the apparent attraction is unexpected because all surfaces bear negative charges. The anomalous long range repulsion for L=2.5 μm, which was not observed in any other experiments, is also not expected from DLVO theory (eq. (4.4)). Similar to the results of the CG experiment,[30,76] DLVO electrostatic repulsion is observed for L=6.5 μm, anomalous attraction is observed for L=4.0 and L=3.0 μm, and anomalous repulsion is observed for L=2.5 μm. Our observations of anomalous interactions similar to the CG experimental results are quite surprising given that only standard DLVO repulsive electrostatic pair interactions were specified our SD simulations.

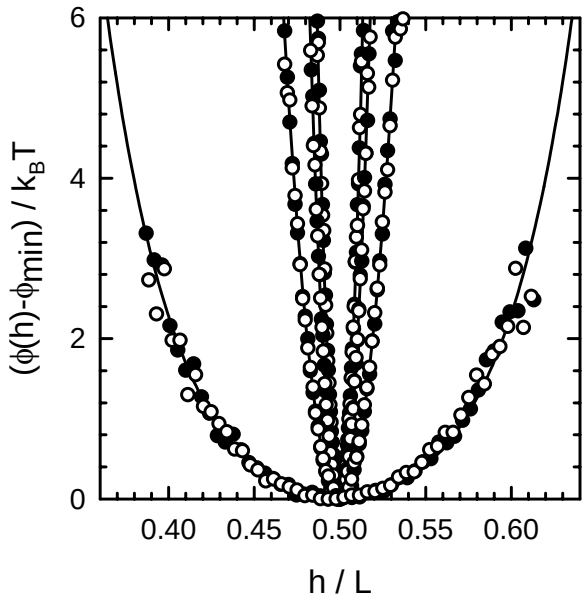

Figure 4.7. Particle-wall potential energy profiles for two 652 nm polystyrene (PS) colloids (ρ_p=1055 kg/m^3, ψ_p=-145 mV) at the mid plane between two charged walls (ψ_w=-58 mV) in a 0.0012 mM (κ^{-1}=275 nm) 1:1 aqueous electrolyte solution (ρ_f = 1000 kg/m^3) (see fig. 4.1c). The wall separations as defined in fig. 4.1c correspond to L=6.5, 4.0, 3.0, and 2.5 μm. Open circles correspond to particle 1, closed circles correspond to particle 2, and solid lines are the DLVO particle potentials specified in the simulations.

While the potential profiles interpreted from our SD simulations in fig. 4.6a have qualitative similarities with the original findings in the CG experiment, important quantitative differences exist. For instance, the apparent range of the potentials in the CG experiment were originally observed to shift to shorter separations by ~1 μm compared to nearly identical measurements for the same 652 nm PS colloids far from any boundaries. Our interpreted potentials in fig. 4.6a do not display this inward shift. In addition, the CG data exhibit more complex separation dependent potential profiles with either greater anomalous attraction or repulsion at relatively short separations. The

discrepancies between our findings in fig. 4.6a and the reported CG results suggest our SD simulations including electrostatic DLVO potentials (eq. (4.4)) do not completely capture the behavior of like-charged colloidal pairs confined between parallel like-charged walls.

Although we do not quantitatively duplicate the potentials found in the CG experiment, we attempt to understand the anomalous interactions inferred from our dynamic simulations in which only repulsive electrostatic DLVO pair interactions were specified between the particles and walls. Because the one-dimensional transition probability analysis fails to recover known input interactions for L=4.0, 3.0 μm, and 2.5 μm in fig. 4.6a, it might be expected that the analysis in eqs. (4.8) and (4.11) is also invalid for the CG experiment due to multi-dimensional dissipative interactions similar to our explanations of results in figs. 4.3-4.5. However, the effective potential in eq.. (4.14) predicts successful recovery of the repulsive DLVO particle-particle potential for all wall spacings in fig. 4.6a. In particular, the term in eq. (4.14) involving the particle-wall interaction is identically zero due to symmetry (see fig. 4.7), and the first and third terms, while deviating slightly from unity and zero, produce negligible contributions for the particle and wall separations in fig. 4.6a. The terms in eq. (4.14) cannot account for the anomalous repulsion in the L=2.5 μm case. Because the anomalous interactions in fig. 4.6a, which are interpreted from simulations using only repulsive potentials, are not explained by multi-dimensional hydrodynamics, another factor must be responsible for the discrepancy between the simulated particle-particle potentials and the potentials inferred from non-equilibrium particle dynamics.

From insights gained in figs. 4.2-4.5, we explored several modifications to the CG experimental protocol that allowed us to ultimately recover the simulated DLVO potentials for each value of L as shown in fig. 4.6b. All parameters in fig. 4.6b were identical to those in fig. 4.6a with the single exception that 80,000 images were acquired instead of the 40,000 images in the original CG experiment. This result suggests that at least part of the anomalous behavior inferred in the CG experiment using the one-dimensional transition probability analysis may be due to insufficient statistical sampling of particle dynamics when constructing the transition probability tensor. Although a significantly smaller number of points (6502) allowed successful recovery of particle interactions in a similar experiment in bulk media[52] and even the 6.5 μm case in fig. 4.6a, it appears that hydrodynamic hindrance in confined geometries may affect the sampling parameters necessary to obtain a statistically significant set of independent points when constructing the transition probability tensor. Details concerning proper statistical sampling of the transition probability tensor are beyond the scope of this work, but given their apparent influence on the results in figs. 4.3, 4.5 and 4.6, they appear to be an issue worthy of further investigation.

A final issue worth addressing is the speculation by SB that repeated displacement of the particle pair away from the mid-plane in the CG experiment could also produce anomalous attraction via hydrodynamic effects. In SD simulations where we intentionally offset particles from the mid-plane by up to 300 nm in the CG experiment (beyond the 150 nm uncertainty suggested by CG[30]), no anomalous attraction was observed as long as 80,000 images were acquired. From our simulation

data, particles move back to the mid-plane much faster than the 1/60s image capture time such that multi-dimensional dissipative effects appear insignificant. It is also important to note that offsetting the particles from the mid-plane in eq. (4.14) cannot account for the anomalous repulsion depicted in fig. 4.6a for L=2.5 μm. Because increasing the number of points used to construct the experimental transition probability tensor consistently corrects both the anomalous attraction and repulsion in our results in fig. 4.6, it may partially explain the anomalous interactions in the CG experiment.

Because we do not observe an inward shift or quantitative agreement with the magnitudes of anomalous interactions in our simulated results in fig. 4.6 compared to the CG experiment, our findings do not appear to fully account for the non-equilibrium behavior of confined colloidal pairs. However, by identifying possible issues related to experimental sampling of particle dynamics when constructing the transition probability tensor, we are able to account for some qualitative features of the anomalous CG potentials. Despite our imperfect reproduction of the CG experimental results, our findings provide some new insights into anomalous attraction using only DLVO conservative potentials and multi-body resistance tensors calculated using the methods of Brady and Bossis.[2] By at least partially reproducing features observed in the CG experiment and also considering particle-wall interactions, our results in figs. 4.6 and 4.7 provide a basis for future refinements to better understand the origin of anomalous potentials inferred from non-equilibrium measurements of confined colloidal pairs.

4.7. Conclusions

To summarize and conclude our findings, we initially verified the ability of the one-dimensional transition probability analysis to measure particle-wall interactions in a typical TIRM experiment. We demonstrated this same analysis to be suitable for recovering particle-particle and particle-wall interactions for particle pairs held in a blinking optical tweezer far below a single charged wall ($h \approx 30a$). For the same experiment conducted closer ($h \approx 10a$) to either charged or uncharged walls, an anomalous particle-particle attraction was inferred from relative projected particle displacements in agreement with reported measurements. The one-dimensional transition probability analysis fails in this case because it does not consistently treat multi-body hydrodynamics that are also inherently multi-dimensional.

By deriving effective potentials that consider the multi-body mobility tensor and its gradient, we were able to quantitatively predict anomalous attraction in previous and several new illustrative experiments involving particle pairs near one wall. Our effective potentials were derived using an approach similar to that originally reported by Squires and Brenner. By including a more rigorous mobility tensor and its gradient, we recover quantitative predictions of the net anomalous attraction between charged particles near a single charged wall with different relative contributions from new and previously reported effects. Our effective potentials also predict the anomalous attraction between charged particles adjacent to an uncharged wall, which is not captured by previous explanations. A different effective potential expression was derived to capture anomalous attraction between a particle and wall when one additional particle is nearby.

Our capabilities for interpreting conservative potentials from non-equilibrium colloidal dynamics are thus expanded from bulk particle pairs and single particle-wall interactions (fig. 4.2) to include particle-particle and particle-wall interactions for charged colloidal pairs near single charged and uncharged walls (figs. 4.3-4.5). For particle pairs confined between parallel walls (figs. 4.6, 4.7), we obtain evidence suggesting the anomalous attraction may be partially accounted for by statistical sampling effects. While data sampling issues appear to explain some of the features in experimentally measured anomalous potentials, other important characteristics are not captured by our SD simulations. These results demonstrate that accurate treatment of the multi-body mobility tensor and its gradient can fully account for anomalous attraction inferred from particle dynamics near a single wall and appear to partially explain anomalous interactions for particle pairs between parallel confining walls.

Our findings reported here are not expected to explain recent inferences of anomalous attraction from equilibrium measurements of confined ensembles,[63] where dissipative effects are inherently unimportant, or in small κa systems,[64,65] where many-body electrostatic interactions may be important. The analytical and simulation results presented in this section are intended to provide a constructive basis for self-consistently interpreting equilibrium and dynamic interactions in interfacial and confined colloidal systems. Ultimately, our goal is to assist the robust design and interpretation of increasingly complex future experiments.

5. DYNAMIC SIGNATURE FOR THE EQUILIBRIUM PERCOLATION THRESHOLD OF WEAKLY ATTRACTIVE COLLOIDAL FLUIDS

5.1. Synopsis

Short time self diffusivities, D_S^S, are computed for attractive colloidal fluids with van der Waals potentials to identify their percolation threshold and a previously unexplained dynamic transition. Our results show a discontinuous change in the slope of D_S^S vs. temperature as the percolation threshold is crossed. Because D_S^S depends only on multi-body hydrodynamic interactions, the percolation threshold of attractive colloidal fluids is shown to correspond to a transition in a dynamic property consistent with the linear viscoelastic measurements of Woutersen, et al.[32]

5.2. Introduction

Attractive colloidal particles form equilibrium and non-equilibrium microstructures determined by their concentration and the magnitude and range of their attraction. For weak attraction, single phase fluids and coexisting gas-liquid and liquid-solid phases are observed, whereas strong attraction produces irreversible fractal gels[34]. Elevated attraction and concentration can also produce dynamically arrested microstructures.[77] Whether colloidal attraction originates from van der Waals, depletion, or biomolecular interactions, controlled assembly of attractive colloids into useful microstructures requires the ability to intelligently manipulate particle interactions and dynamics to navigate free energy landscapes in such systems.

To begin to understand the importance of multi-body hydrodynamic interactions in colloidal assembly processes, here we investigate dynamical changes as the equilibrium percolation threshold (PT) is crossed, which is one of the simplest structural transitions of weakly attractive colloids. The equilibrium PT is defined to occur when attractive colloids produce system spanning clusters in half of all configurations. The PT is not a phase transition since it is not accompanied by discontinuous changes in thermodynamic quantities or their derivatives, but is a distinctive feature in an otherwise barren landscape of single phase fluid configurations with insufficient concentration or attraction to produce coexisting equilibrium phases, arrested glasses, or irreversible gels.

Although the PT is one of few notable features on kinetic pathways from initially hard sphere fluids towards gel, glass, and crystal structures at higher particle attractions and concentrations, changes in relaxation mechanisms and frequency dependent properties of colloidal fluids across the PT are not yet fully understood. Numerous studies have investigated attraction and concentration dependent rheological transitions in colloidal fluids with temperature dependent pair potentials but have focused primarily on the fluid-gel transition beyond the PT.[78-80] Experimental studies of dynamical changes across the PT are generally complicated by having to measure linear viscoelastic properties and also having an independent measurement of the percentage of system spanning clusters averaged over space and time. Although much theoretical work has been dedicated to consistently treating thermodynamic and hydrodynamic relaxation mechanisms in repulsive colloidal fluids,[81] similar approaches have not been extended to attractive colloidal fluids in the vicinity of their PT.

Here we report evidence of a dynamic signature of the equilibrium PT of attractive colloid fluids that is dominated by multi-body hydrodynamic interactions. In particular, we observe a discontinuous rate of change in the short time self diffusivity, D_S^S, vs. temperature, T, for polymer coated colloids with realistic van der Waals (vdW) potentials at a locus of conditions nearly identical to the PT of adhesive spheres (AS) with equivalent second virial coefficients, B_2. This dynamic signature serves as a criterion for the equilibrium PT of attractive colloids and provides new insights into the role of multi-body, dissipative hydrodynamic interactions in the structural evolution of attractive, single phase, equilibrium colloidal fluids. The predicted change in D_S^S across the percolation threshold is consistent with, and can be used to explain, the linear viscoelastic measurements of attractive colloidal fluids by Woutersen, et al.[32]

5.3. Phase Diagram of Polystyrene Particles with Adsorbed Polymer

This investigation is motivated by our previous measurements of a T and concentration dependent transition of polystyrene (PS) colloids (radius, a = 180 nm) with adsorbed PEO-PPO-PEO (thickness at 25 C, δ = 20 nm) in aqueous 0.5 M NaCl[82] for which the potential is well known.[83] Fig. 5.1 shows a phase diagram for such polymer coated particles as a function of T and PS core particle volume fraction, ϕ_{core}. With increasing T, the net attraction is mediated by diminishing solvent quality for the PEO moieties. The pair potential between such particles (hereafter referred to as the vdW potential) can be modeled to include a hard wall repulsion that collapses with increasing T and a van der Waals attraction between core particles and solvated

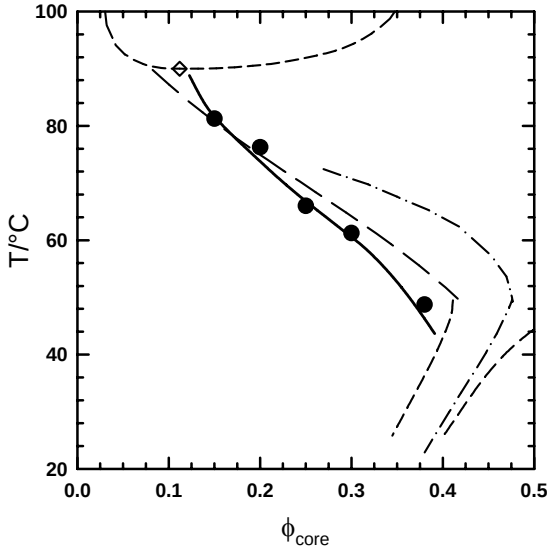

Figure 5.1. Phase diagram showing gas-liquid and liquid-solid coexistence (--) and critical point (◊); percolation thresholds from MC simulations (▬),[85] theory (—),[86] and transitions in short time self diffusivity (●); glass lines (— ··).[77]

copolymer coatings. By equating B_2's for the vdW and AS potentials (to link T and the AS parameter τ), fig. 5.1 is constructed to show AS predictions for gas-liquid coexistence and the critical point,[82] liquid-solid coexistence,[84] the PT,[85,86] and glass lines.[77] The phase diagram appears inverted due to the lower critical solution temperature of the adsorbed copolymer in aqueous media.

5.4. Results and Discussion

To understand how structural relaxations change as the PT is approached and traversed with increasing attraction in equilibrium colloidal fluids, we performed standard canonical (NVT) Monte Carlo (MC) simulations for copolymer coated particles

interacting via the vdW potential. Equilibrium configurations for 108 and 256 particles were generated for a range of T and ϕ_{core} values bounding the AS PT in fig. 5.1.

Before examining dynamic quantities, we first establish that the MC simulated equilibrium fluid configurations display the expected continuous changes in thermodynamic properties via the pair distribution function at contact, $g(2a,\phi)$, in fig. 5.2. Results are shown for the five MC simulated ϕ_{core} values on a temperature scale relative to the equivalent AS PT temperature, T-T_{pt}. The MC simulated values of $g(2a,\phi)$ are well represented by the solid lines in fig. 5.2 given by

$$g\left(2a_{eff},\phi_{eff}\right)=g_{HS}\left(2a_{eff},\phi_{eff}\right)\exp\left(-u_{vdW}\left(2a_{eff}\right)\big/kT\right) \tag{5.1}$$

which is the hard sphere radial distribution function at contact [87] times a Boltzmann factor for the vdW potential at contact based on effective radii ($a_{\text{eff}}=a+\delta$) and volume fractions ($\phi_{\text{eff}}=\phi_{\text{core}}(a_{eff}/a)^3$). The data and fits in fig. 5.2 display smooth changes in $g(2a,\phi)$, confirming the absence of any thermodynamic transitions across the equivalent AS PT.

Next, we compute short time, D_S^S, and long time, D_S^L, self diffusivities for the MC simulated fluid configurations in fig. 5.2. Values of D_S^S are computed from the trace of the N-particle diffusion tensor, **D**, as

$$D_S^S=\frac{1}{3N}\left\langle\sum_{i=1}^{3N}D_{ii}\right\rangle \tag{5.2}$$

where the brackets indicate an average over all configurations for each set of T, ϕ_{core}

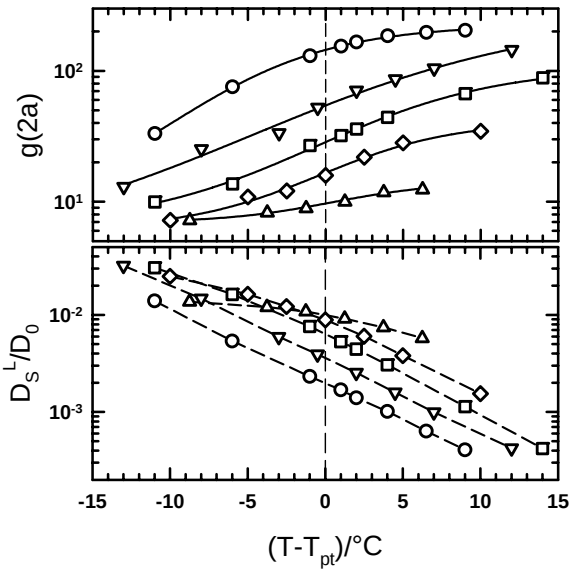

Figure 5.2. Pair distribution function at contact (top) and normalized long time self diffusivity (bottom) for MC simulations of colloids with temperature dependent vdW potentials. Data plotted on temperature scale relative to equivalent AS PT for ϕ_{core}=0.15 (O), 0.20 (∇), 0.25 (□), 0.30 (◊), and 0.38 (Δ). Also shown are fits using eq. (5.1) (—) and lines to guide the eye (--).

conditions. **D** is related to the resistance tensor, **R**, through the generalized Stokes-Einstein relation, $\mathbf{D}=kT\mathbf{R}^{-1}$. Here **R** is computed using the method of Brady and Bossis,[2] where hydrodynamic interactions are separated into far-field, multi-body and a near-field, lubrication contributions as

$$\mathbf{R} = \left(\mathbf{M}^{\infty}\right)^{-1} + \mathbf{R}_{2B} - \mathbf{R}_{2B}^{\infty} \tag{5.3}$$

where $\mathbf{M}^{\infty}$ is the far-field mobility tensor constructed in a pairwise manner. The inverse of $\mathbf{M}^{\infty}$ is a true multi-body, far-field approximation to the resistance tensor. Lubrication

is included by adding the exact two-particle resistance tensor,[88] $\mathbf{R}_{2B}$, and subtracting the two-body, far-field resistance tensor, $\mathbf{R}_{2B}^{\infty}$, to avoid double counting.

To demonstrate the accuracy of eqs. (5.2) and (5.3) for attractive equilibrium colloidal fluids before applying them to all MC simulated configurations, we compare them with mean squared displacements (MSD), $\langle \Delta r^2(\Delta t) \rangle$, obtained from Stokesian Dynamic (SD) simulations. SD simulations were performed using the Langevin equation[74] described in Section 2 as

$$\mathbf{r} = \mathbf{r}^0 + kT\left(\nabla \cdot \mathbf{R}^{-1}\right)\Delta t + \mathbf{R}^{-1} \cdot \mathbf{F}^P \Delta t + \mathbf{X}\left(\Delta t\right) \tag{5.4}$$

where $\mathbf{r}$ is the $3N$ particle coordinate vector, $\mathbf{F}^P$ is the net conservative force vector, and $\mathbf{X}$ is the random Brownian displacement such that $\langle \mathbf{X} \rangle = \mathbf{0}$ and $\langle \mathbf{XX} \rangle = 2kT\mathbf{R}^{-1}\Delta t$. The time step, Δt, was chosen to be larger than the momentum relaxation time, $\tau_B = m/(6\pi\mu a)$, but smaller than the diffusive time, $\tau_D = a^2/D_0$, where $D_0 = kT/(6\pi\mu a)$ is the single particle Stokes-Einstein diffusivity.

Using the final MC simulated configuration at T=70C, ϕ_{core}=0.25 as the initial configuration in an SD simulation, fig. 5.3 shows a solid line for MSD vs. time by averaging over multiple time origins and all particles (N=108). The dashed line intercepting the origin and tangential to the MSD at short times has a slope of $6(D_S^S/D_0)$ where D_S^S was computed using eqs. (5.2) and (5.3) by averaging over all MC simulated configurations at T=70C, ϕ_{core}=0.25. The dashed line tangential to the linear region at long times has a slope of $6(D_S^L/D_0)$ where [81]

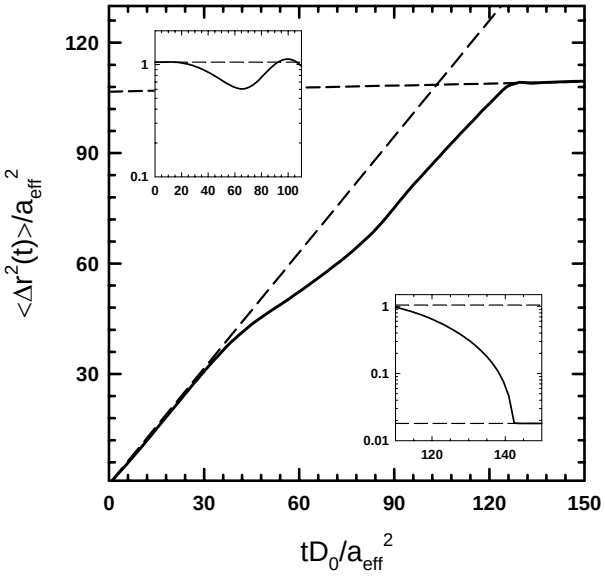

Figure 5.3. MSD and its derivative (insets) vs. time from SD simulations (—) at T=70C, ϕ_{core}=0.25. Short time (eq. (5.2)) and long time (eq. (5.5)) diffusivities predicted from MC simulated configurations (--) at the same conditions.

$$D_S^L = D_S^S \left[1 + 2\phi_{eff}\, g\left(2a_{eff}, \phi_{eff}\right)\right]^{-1} \tag{5.5}$$

and $g(2a, \phi_{eff})$ and $D_S{}^S$ are computed using eqs. (5.1)-(5.3). Insets in fig. 5.3 show derivatives of MSD vs. time as solid lines and values of $6(D_S{}^S/D_0)$ and $6(D_S{}^L/D_0)$ from MC simulations as dashed lines.

Fig. 5.3 displays excellent agreement between $D_S{}^S$ and $D_S{}^L$ obtained from SD simulations and predictions from eqs. (5.1) and (5.5) with MC simulated configurations. The agreement of diffusivities determined independently from MC and SD simulations confirm that equilibrium colloidal fluids are retained beyond the PT and that $D_S{}^S$ and $D_S{}^L$

can be accurately predicted from MC simulations without performing computationally expensive dynamic simulations. D_S^S has a known system size dependence in eq. (5.2) [89] that can be corrected using[90]

$$D_S^S(\infty) = D_S^S(N) + D_0\mu/\eta\left[1.7601(\phi/N)^{1/3} - (\phi/N)\right] \tag{5.6}$$

where $D_S^S(\infty)$ is the infinite system size value, $D_S^S(N)$ is the N-particle value, and μ and η are the medium and dispersion viscosities. Because simulations were performed for N=108 and N=256, $D_S^S(\infty)$ could be obtained without independently determining μ/η.

Using eqs. (5.2), (5.5), and (5.6), D_S^S and D_S^L were computed for MC simulated configurations of vdW particles for all conditions investigated in fig. 5.2. To demonstrate the smooth variation of D_S^L across the PT (similar to molecular fluids), Fig 5.2 shows D_S^L vs. T-T_{pt}. For comparison, fig. 5.4 shows a plot of D_0/D_S^S vs. T for different ϕ_{core}. Each ϕ_{core} set displays a pronounced slope change at temperatures estimated from the intersection of linear fits to high and low temperature regions. The resulting transition temperatures for each ϕ_{core} set (plotted in fig. 5.1) indicate a dynamic transition of vdW particles nearly identical to the equivalent AS PT. As a result, the PT of vdW particles appears to have a dynamic signature determined exclusively by multi-body hydrodynamic interactions contained in D_S^S in eq. (5.2).

An advantage of identifying the PT from changes in D_0/D_S^S is its direct connection to linear viscoelastic properties in attractive colloidal fluids. Because D_0/D_S^S is proportional to the high frequency dynamic viscosity, η_∞/μ,[81] the results in fig. 5.4

predict an abrupt rate of change in η_∞/μ vs. T at the PT of attractive colloidal fluids that can be compared with experimental measurements. This prediction appears to be consistent with the unique high frequency, linear viscoelastic measurements of an attractive colloidal fluid (octadecyl coated silica in benzene) by Woutersen, et al.[32] By fitting a general Maxwell model to their dynamic viscosity measurements in the range 70-250,000 Hz, Woutersen, et. al. found an abrupt change in the dependence of the relaxation time, a^2/D_S^S, vs. T at the PT. Our results in fig. 5.4 suggest the mechanism for their observed transition in a^2/D_S^S vs. T is based on changes in multi-body hydrodynamic interactions as the PT is crossed.

Although D_S^S is a measure of local particle mobility, it is important to note that it critically depends on both near-field, lubrication and far-field, multi-body interactions. In fact, inclusion of multi-body, far field interactions is essential to the proper prediction of D_S^S to obtain even qualitative agreement with experiments.[89] Because D_S^S has a unique multi-body dependence on particle configurations that is distinct from the pairwise dependence of $g(r)$, it is possible to have a dynamic transition determined by dissipative interactions at the PT in fig. 5.1 for conditions where pairwise conservative interactions produce no thermodynamic transition. Values of D_S^S computed by considering only pairwise lubrication interactions between adjacent particles are not expected to capture the transition in fig. 5.4.

It should be noted that the transition in D_0/D_S^S vs. T in fig. 5.4 across the percolation threshold occurs within the single phase fluid region of fig. 5.1 and does not indicate a fluid-solid transition associated with gelation or dynamic arrest.[78-80] Although

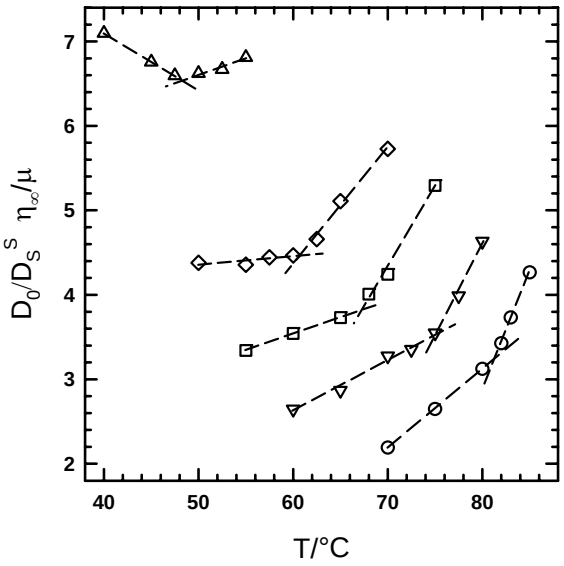

Figure 5.4. Reciprocal of normalized short time self diffusivity vs. temperature for ϕ_{core}=0.15 (O), 0.20 (∇), 0.25 (□), 0.30 (◊), and 0.38 (Δ). Linear fits shown to guide the eye (--).

D_S^S contributes to $\eta(\omega)/\mu$ at all frequencies based on its dominance at the high frequency limit ($D_S^S \sim \eta_\infty^{-1}$) and finite contribution to D_S^L (eq. (5.5)) in the zero frequency limit ($D_S^L \sim \eta_0^{-1}$), the smooth variation of D_S^L across the PT in fig. 5.2 indicates that the low frequency dynamic viscosity, η_0/μ, should not display any discontinuous changes indicative of gelation or dynamic arrest [79,80]. Thus, the discontinuous rate of change in D_S^S vs. T in fig. 5.4 is a dynamic signature of the PT only and does not indicate a fluid-gel transition that is expected beyond the PT.[78]

Although our simulated results in fig. 5.4 are consistent with the high frequency measurements of Woutersen, et. al., it is not obvious how the complete spectrum of

relaxation times varies across the PT. The inverse relationship between dynamic viscosity and self diffusivity should allow prediction of the normalized viscosity, $(\eta(\omega)-\eta_\infty)/(\eta_0-\eta_\infty)$, in terms of the normalized self diffusivity, $(1/D_S(\omega)-1/D_S^S)/(1/D_S^L-1/D_S^S)$, vs. the non-dimensional frequency, $\omega a^2/D_S^S$.[81] Another issue when comparing our results with rheological experiments is the possibility of departures from equilibrium. Our results may be valid for small perturbations to equilibrium structures, but additional multi-body hydrodynamic contributions may be expected to affect relaxation times in non-equilibrium colloidal fluids.[91]

A final issue worth noting is the benefit of identifying the PT using the dynamic criterion based on its applicability to particles with continuous potentials such as the vdW attraction examined here. For the inverse power law decay of vdW potentials, an arbitrary cutoff separation must be specified to identify connectedness, clusters, and the PT in particle configurations. For comparison, particles with discontinuous AS and square well potentials form unambiguous "bonds" for separations within their attractive wells. However, by observing changes in D_0/D_S^S at a locus of T, ϕ_{core} conditions, we recover a PT for vdW particles nearly identical to equivalent AS particles with a clearly identifiable PT. The dynamic signature of the PT provides a means to avoid the connectedness issue. Re-analyzing our data with knowledge of the PT also indicates that a unique cutoff separation does not exist for the vdW potential.

5.5. Conclusions

In conclusion, we report evidence of a dynamic transition at the equilibrium PT

of attractive colloidal fluids based on a discontinuous rate of change in D_0/D_S^S vs. T data for a range of ϕ_{core} values. Our results indicate a dynamic signature for the PT that is consistent with the rheological measurements of Woutersen, et al.[32] Extension of these findings might provide insights into the combined roles of multi-body, dissipative and pairwise, conservative interactions for other colloidal structural transitions, particularly for colloids with different effective thermodynamic and hydrodynamic sizes.

6. SELF-DIFFUSION IN CONCENTRATED INTERFACIAL COLLOIDAL FLUIDS

6.1. Synopsis

This section reports methods to interpret and predict self diffusion in concentrated interfacial colloidal fluids, where particles are confined near surfaces by gravity, but levitated at sub-monolayer coverages. Expressions for self-diffusion in three dimensions are extended to two dimensions, and their validity tested, using Monte Carlo and Stokesian Dynamic simulations. Theoretical expressions, based on multi-body hydrodynamic interactions, pairwise colloidal and surface potentials, and many-particle packing effects, are used to describe short- and long-time self diffusion in quasi two dimensional fluids, for directions both parallel and normal to underlying flat surfaces.

Monte Carlo and Stokesian Dynamic simulations are used to generate equilibrium particle coordinates for interfacial colloidal fluids. Two systems are considered, one where particles interact via screened electrostatic repulsion and another where particles interact via weak van der Waals attraction. For both potentials, we compare short- and long-time self diffusion coefficients as determined for Monte Carlo simulated particle configurations using analytical expressions. We also use dynamic trajectories generated using Stokesian Dynamic simulations to calculate average mean-squared displacements. We show that analytical expressions for calculating self diffusion coefficients from equilibrium particle configurations agree with those determined from mean squared displacements of dynamic particle trajectories. The

theory and simulations reported in this work are expected to be broadly applicable to the interpretation and prediction of self diffusion, in realistic experiments based on the accurate treatment of multi-body hydrodynamic interactions.

Analyses for short-time and long-time self-diffusion in interfacial colloidal fluids are demonstrated, both parallel and normal to the wall, by performing Stokesian Dynamic simulations with accurately modeled multi-body hydrodynamic interactions. Self diffusion coefficients for concentrated fluids are compared with the infinitely dilute (single particle) limit to illustrate the effect of many particles. Our results demonstrate the validity of extending existing expressions for self-diffusion coefficients in three dimensions to interfacial colloidal fluids.

6.2. Introduction

Understanding dynamics of colloidal fluids near an interface is important in several different areas involving colloids near interfaces, ranging from paints and coatings, to self-assembly of photonic crystals on substrates. Novel surface imaging methods such as Diffusing Colloidal Probe Microscopy involve colloidal particles diffusing near an interface. There has been a lot of confusion on the role of dissipative hydrodynamic forces in measuring and interpreting conservative interaction potentials between particles close to a surface. The success of these methods depends on our ability to understand and quantify equilibrium and dynamic behavior of colloidal fluids near an interface. Techniques such as template-directed self-assembly of colloids to make ordered structures are not yet successful, mainly due to the inability to control

dynamics of colloids near a surface. It is therefore crucial to be able to quantify diffusion coefficients of particles interacting via a specific potential near an interface.

Several papers report experiments on dynamics of colloidal particles near interfaces.[92-94] There have also been simulation studies both with and without hydrodynamic interactions to explore equilibrium and dynamic properties of interfacial colloidal dispersions.[42,95] However, there has been no systematic study of applying expressions for short- and long-time self-diffusion based on multi-body hydrodynamic interactions in concentrated interfacial colloidal fluids. It is well known that the dynamics of colloidal dispersions is strongly controlled by multi-body hydrodynamic interactions. Brady and Bossis[2] developed a method called Stokesian Dynamics to describe motion of particles under the influence of hydrodynamic and conservative forces. Pesche and Nagele[42] reported studies of confined colloidal monolayer, using a version of Stokesian Dynamics where hydrodynamic interaction with the wall was treated approximately, by using a Stokeslet description for the far-field hydrodynamics. However, in concentrated dispersions, this formalism is not expected to yield suitable results.

Nott and Brady[24] and Singh and Nott[25] suggested a method, where the wall's far-field contribution to the hydrodynamic resistance tensor was captured by discretizing the wall into an array of touching spheres. This formalism enables accurate prediction of hydrodynamic resistances for particles near an interface. A direct result of this is the ability to calculate the short-time self-diffusion coefficients of an interfacial colloidal fluid. The expression for long-time self-diffusion coefficient has been derived by

Brady[27] by combining hydrodynamics via the short-time self-diffusion coefficient and a thermodynamics, via the radial distribution function.

Although these methods have been reported in literature, there has been no systematic study where these results have been compared with simulations or experiments for the case of diffusion in interfacial colloidal fluids. In this work, we present accurate Stokesian Dynamic simulations for interfacial colloidal fluids and demonstrate the applicability of various expressions for self-diffusion of particles. We strongly feel that this is an important test case before explicitly attempting to use these expressions to analyze experimental data.

In this section, we report analyses of Monte Carlo and Stokesian Dynamic simulated particle configurations to quantify diffusion in interfacial fluids. Monte Carlo (MC) simulations are used to generate equilibrium particle configurations for two interfacial fluids, one where particles interact via screened electrostatic repulsion and another where the particles interact via an attractive van der Waals potential. We also perform Stokesian Dynamic (SD) simulations to generate dynamic particle trajectories, by rigorously incorporating hydrodynamic interactions between all particles and the wall. We report several dynamic tools to quantify the time-dependent self-diffusion coefficients of the particles. We demonstrate the use of accurate simulations and theory to accurately describe dynamics in interfacial colloidal fluids.

6.3. Colloidal, Surface, and External Conservative Forces

Colloidal and external conservative forces are calculated as the gradient of a scalar potential energy function. Conservative forces include colloidal particle-particle and particle-wall interaction potentials and external gravitational potential. All colloidal forces are assumed to be pairwise additive. The forces are expressed as

$$\mathbf{F}^{P} = \mathbf{F}^{pp} + \mathbf{F}^{pw} + \mathbf{F}^{grav} \tag{6.1}$$

where $\mathbf{F}^{pp}$ is the force due to particle-particle interaction, F^{pw} is the force due to particle wall interaction, and $\mathbf{F}^{grav}$ is the buoyant force. The particle-particle and particle-wall forces are calculated as the derivative of their respective potential energy functions $u_{pp}(r)$ and $u_{pw}(h)$, and are given by

$$\begin{aligned} \mathbf{F}^{pp} &= -\nabla u_{pp}\left(r\right) \\ \mathbf{F}^{pw} &= -\nabla u_{pw}\left(h\right) \end{aligned} \tag{6.2}$$

where r is the particle-particle separation and h is the particle-wall separation. The net particle-particle and particle-wall potentials are represented as the superposition of relevant potentials as

$$\begin{aligned} u_{pp}\left(r\right) &= u_{pp}^{elec}\left(r\right) + u_{pp}^{vdw}\left(r\right) + u_{pp}^{steric}\left(r\right) \\ u_{pw}\left(h\right) &= u_{pw}^{elec}\left(h\right) + u_{pw}^{vdw}\left(h\right) + u_{pw}^{steric}\left(h\right) \end{aligned} \tag{6.3}$$

In this study, we consider two different systems, one in which the particles interact via an electrostatic repulsive potential and another where the particles interact via a combination of an attractive van der Waals potential and a hard wall steric repulsion.

For the electrostatic system, the particle-particle and particle-wall pair potentials are well represented by[34]

$$\begin{aligned} u_{pp}(r) &= B_{pp}\exp\left[-\kappa(r-2a)\right] \\ u_{pw}(h) &= B_{pw}\exp\left[-\kappa(h-a)\right] \end{aligned} \tag{6.4}$$

The B parameters are related to the particle size and surface potentials as

$$\begin{aligned} B_{pp} &= 32\pi\varepsilon a\left(\frac{kT}{ze}\right)^2\tanh\left(\frac{ze\psi_p}{4kT}\right)\tanh\left(\frac{ze\psi_p}{4kT}\right) \\ B_{pw} &= 2B_{pp} \end{aligned} \tag{6.5}$$

where ε is the absolute permittivity, z is the charge number of the ions in the solvent, and κ is the Debye screening length given by

$$\kappa = \left(\frac{2CN_Ae^2}{\varepsilon k_BT}\right) \tag{6.6}$$

Here, C is the bulk electrolyte concentration, N_A is Avogadro's constant, and e is the charge on an electron.

For the attractive system, the cumulative potential is a van der Waals attraction due to the core particle and the adsorbed polymer, combined with hard wall repulsion at a separation where the polymer layers come in contact. The particle-particle van der Waals interaction, which arises due to a mismatch in particle and medium dielectric properties is well represented by non-integer power law decay to Lifshitz theory by[44]

$$u_{pp}^{vdw}(r) = -aA(r-2a)^{-p} \tag{6.7}$$

The steric interaction due to adsorbed polymer is reasonably well represented for modeling colloidal fluids by a hard wall interaction given by

$$u^{steric}(x) = \begin{cases} 0 & x > x_{ref} \\ \infty & x \le x_{ref} \end{cases} \tag{6.8}$$

which is suitable for either the particle or the wall by substituting center-to-center separation, r, or center-to-surface separation, h, for x, and x_{ref} is reference for zero surface separation corresponding to hard wall contact. The particle-wall potential in the attractive system is fixed as a hard-wall interaction.

The gravitational body force due to the buoyant particle weight via a density mismatch is given by

$$\mathbf{F}^{grav} = -\frac{4}{3}\pi a^3 \left(\rho_s - \rho_f\right) g \tag{6.9}$$

ρ_s and ρ_f are the densities of the particle and the fluid respectively, and g is the acceleration due to gravity.

6.4. Prediction of Self-Diffusion Coefficients from Equilibrium Particle Configurations

The diffusion coefficient of an isolated colloidal particle undergoing a three dimensional random walk far from any boundaries is given by the Stokes-Einstein equation as,

$$D_0 = \frac{kT}{6\pi\mu a} \tag{6.10}$$

where μ is the surrounding medium viscosity and a is the particle radius. For a single colloidal particle near a planar surface, hydrodynamic interactions between the particle and surface hinder the particle's diffusion both normal and parallel to the surface. The single particle's diffusion coefficients near a planar surface for given separation, h between the particle and surface is given by,

$$\begin{aligned} D_{\parallel}(h) &= D_0 f_{\parallel}(h) \\ D_{\perp}(h) &= D_0 f_{\perp}(h) \end{aligned} \tag{6.11}$$

where the functions $f_{\parallel}(h)$ and $f_{\perp}(h)$ have been calculated in literature by analytically solving the Navier-Stokes equations for a sphere near a plane wall by Goldman et al.[96] and Brenner[97] respectively. These solutions are conveniently represented by rational expressions (with less than ±0.001 relative error) as,

$$\begin{aligned} f_{\parallel}(h) &= \frac{12420\left(\frac{h-a}{a}\right)^2 + 5654\left(\frac{h-a}{a}\right) + 100}{12420\left(\frac{h-a}{a}\right)^2 + 12233\left(\frac{h-a}{a}\right) + 431} \\ f_{\perp}(h) &= \frac{6\left(\frac{h-a}{a}\right)^2 + 2\left(\frac{h-a}{a}\right)}{6\left(\frac{h-a}{a}\right)^2 + 9\left(\frac{h-a}{a}\right) + 2} \end{aligned} \tag{6.12}$$

For a single Brownian levitated particle in equilibrium with the wall under the influence of a particle-wall potential, the average diffusion coefficient is calculated by weighting the diffusion coefficient at each height with its Boltzmann probability. The average diffusion coefficients can be expressed as

$$\left\langle D_{\parallel} \right\rangle = \frac{\int D_{\parallel}(h)\, p(h)\, dh}{\int p(h)\, dh}$$
$$\left\langle D_{\perp} \right\rangle = \frac{\int D_{\perp}(h)\, p(h)\, dh}{\int p(h)\, dh} \tag{6.13}$$

where $\langle D_{\parallel}(h) \rangle$ and $\langle D_{\perp}(h) \rangle$ are ensemble-average lateral and normal diffusion coefficients, and the probability function, $p(h)$ is related to the particle-wall potential, $\underline{u_{pw}}(h)$ by Boltzmann's equation as

$$p(h) = \exp\left[-u_{pw}(h) / kT \right] \tag{6.14}$$

The confinement in the normal direction results in MSD at long times leveling out to an average value about which it shows small fluctuations. The average value about which the MSD fluctuates, h_{∞}^2 is equal to twice the variance of the height distribution of the particle, h, about its mean position, and this is determined by the equilibrium potential energy profile in the normal direction as

$$h_{\infty}^2 = 2 \frac{\int \left(h - \langle h \rangle \right)^2 p(h) dh}{\int p(h) dh} \tag{6.15}$$

where $p(h)$ is the height probability function and the mean height, $\langle h \rangle$ is given by

$$\langle h \rangle = \frac{\int h p(h)\, dh}{\int p(h)\, dh} \tag{6.16}$$

For multiple particles near an interface, the diffusion of a target particle is affected by the presence of the other particles, in addition to the wall. In this case, the

free-particle diffusion is replaced by a quantity called self-diffusion, which is the diffusion coefficient of a particle in the presence of other particles. The self-diffusion coefficients of a particle at short and long times are different and are respectively called short-time and long-time self-diffusion coefficient.

Short-time self diffusion coefficient quantifies the mobility of a particle for displacements much smaller than its radius. Since the small displacements do not perturb the dispersion microstructure, short-time diffusivities can be measured from static snapshots of equilibrium particle configurations.[98] Equilibrium particle configurations from MC simulations are used to compute short-time self diffusion coefficients. The hydrodynamic resistance tensor is constructed using these particle coordinates following the method described earlier. The diffusion tensor for the system of particles is related to the hydrodynamic resistance tensor via the generalized Stokes-Einstein relation as

$$\mathbf{D} = kT\mathbf{R}^{-1} \tag{6.17}$$

where kT is the thermal energy of the bath. The most general way of calculating the short-time self-diffusion coefficient, valid for all concentrations is from the diffusion tensor as

$$\begin{aligned} D^S_{S,\parallel} &= \frac{1}{N_p}\left\langle \sum_{i=1}^{N_p} \frac{D_i^{xx} + D_i^{yy}}{2} \right\rangle \\ D^S_{S,\perp} &= \frac{1}{N_p}\left\langle \sum_{i=1}^{N_p} D_i^{zz} \right\rangle \end{aligned} \tag{6.18}$$

where $D^S_{S,\parallel}$ and $D^S_{S,\perp}$ represent diffusion coefficients lateral and normal to the interface

and the angle brackets denote an ensemble average of the self-terms in the diffusion tensor over all particle configurations.

Long-time diffusion coefficient quantifies the mobility of a particle at displacements much larger than its radius. In order for a particle to make such large displacements, rearrangements within the local structure must occur. The long-time self-diffusion coefficient should thus include a thermodynamic contribution which accounts for the resistance offered by the equilibrium microstructure to rearrange.[27] The long time diffusivity can be calculated as a combination of the short-time diffusivity and a contribution accounting for the perturbation in the equilibrium structure.[27,28] The expression for the long time diffusivity has been approximately derived in literature as[27]

$$D_S^L \approx D_S^S \left[1 + 2\phi g\left(2a;\phi\right)\right]^{-1} \tag{6.19}$$

where the long-time diffusivity is represented as a product of the hydrodynamic and thermodynamic contributions. The thermodynamic contribution is a function of the particle concentration, ϕ and the value of the first peak of the radial distribution function, $g(2a)$. The thermodynamic contribution can be interpreted as an increase in the effective size of the trace particle as it diffuses through the equilibrium structure.[27] For the electrostatic system considered, the particle area fraction in eq. (6.19) is the effective area fraction, based on an effective radius as calculated by the position of the first peak in the radial distribution function.[27] The first peak is obtained from the computed value of the radial distribution functions from MC simulations. For the attractive system, particle area fraction is the true area fraction, but due to the discontinuous nature of the

potential, the absolute value of the first peak of the pair distribution function cannot be obtained from the computed distribution function. The value of the first peak is calculated using the approximation

$$g(2a;\phi) \approx g_{HS}(2a;\phi)\exp\left[-u_{pp}(2a)/kT\right] \tag{6.20}$$

where $g_{HS}(2a)$ is the value of the first peak of a hard-disk radial distribution function at the same concentration as the attractive system and $u_{pp}(2a)$ is the value of the pair potential at $r = 2a$. The hard-disk radial distribution function at contact, for a given particle area fraction, ϕ was calculated using[99]

$$g_{HS}(2a,\phi) = \frac{1-0.436\phi}{(1-\phi)^2} \tag{6.21}$$

6.5. Measurement of Self-Diffusion Coefficients from Dynamic Particle Trajectories

Mean squared-displacement is a fundamental quantity in describing the dynamics of colloidal particles. Particle mean-squared displacement (MSD) was calculated from trajectories obtained by dynamic simulations. MSDs in the x and y directions are equivalent since the system is isotropic in the lateral direction. For each direction, MSD is calculated using

$$W_x(t) = \frac{1}{N_p}\left\langle \sum_{i=1}^{N_p}\left[x_i(t) - x_i(0)\right]^2 \right\rangle \tag{6.22}$$

Here, the angle brackets denote ensemble averages and multiple time origins are used to ensure adequate statistics. The total number of origins is taken to be half the total

number of steps to ensure each step is weighted equally. The lateral mean-squared displacement is reported as a sum of the *x* and *y* mean squared displacements.

Autocorrelation functions were calculated for each particle in the normal direction to obtain information about the dynamics of the colloidal monolayer normal to the interface. Normalized position autocorrelation functions are calculated as an average over all particles as

$$A(t) = \frac{1}{N_p} \sum_{i=1}^{N_p} \frac{\langle h_i(t) h_i(0) \rangle}{\langle h_i^2(0) \rangle} \tag{6.23}$$

The autocorrelation function, $A(t)$ is calculated using eq (6.23) and expressed in a normalized manner as

$$\hat{A}(t) = \frac{A(t) - A(t \to \infty)}{A(0) - A(t \to \infty)} \tag{6.24}$$

and the limits are given by

$$\begin{aligned} A(0) &= \langle h^2 \rangle \\ A(t \to \infty) &= \langle h \rangle^2 \end{aligned} \tag{6.25}$$

where the angle brackets indicate an ensemble average over all particles and all time steps. The normalized autocorrelation function varies between 0 and 1 when plotted according to eq. (6.24). The slope of the autocorrelation function in the limit as $t \to 0$ is the average normal diffusion coefficient.

6.6. Results and Discussion

Fig. 6.1 shows plots of pair correlation functions and height probability distribution functions with particle-particle and particle-wall pair interactions. We consider two different systems for studying interfacial colloidal dynamics. Fig. 6.1a shows pair correlation functions (main) and particle-particle interaction potentials (inset) for two colloidal dispersions, I and II. Fig. 6.1b shows probability distribution functions of particle heights (main) and particle-wall interaction potentials (inset) for I and II. System I is a dispersion of a = 1μm silica (ρ = 1.98 g/cc) negatively charged particles (ψ_p = -75 mV) at a particle area fraction ϕ = 0.35, near a negatively charged wall (ψ_w = -75 mV) in a medium of water (ρ = 1.00 g/cc) with an ionic strength of C = 0.1 mM, corresponding to a Debye length (κ^{-1} = 30 nm). System II is a dispersion of hydrophobic a = 1μm silica (ρ = 1.98 g/cc) particles covered with a tri block copolymer (PEO-PPO-PEO) in a medium of water with ionic strength C = 1M. The large salt concentration effectively screens electrostatic interactions, and the particles interact via an attractive van der Waals potential. The thickness of the polymer layers can be controlled by varying temperature. The particle concentration based on the core silica radius is ϕ_{core} = 0.55. The dispersion is at a temperature of 60 °C, where the exposed van der Waals attraction corresponds to a well depth of 3.4 kT. The particle concentrations for the two systems were chosen so as to be as high as possible, while the dispersion still remained an equilibrium fluid. The electrostatic system crystallizes at about $\phi \approx 0.35$, while the attractive van der Walls fluid reaches the percolation threshold at $\phi \approx 0.60$ for a well

depth of 3.4 *kT*.

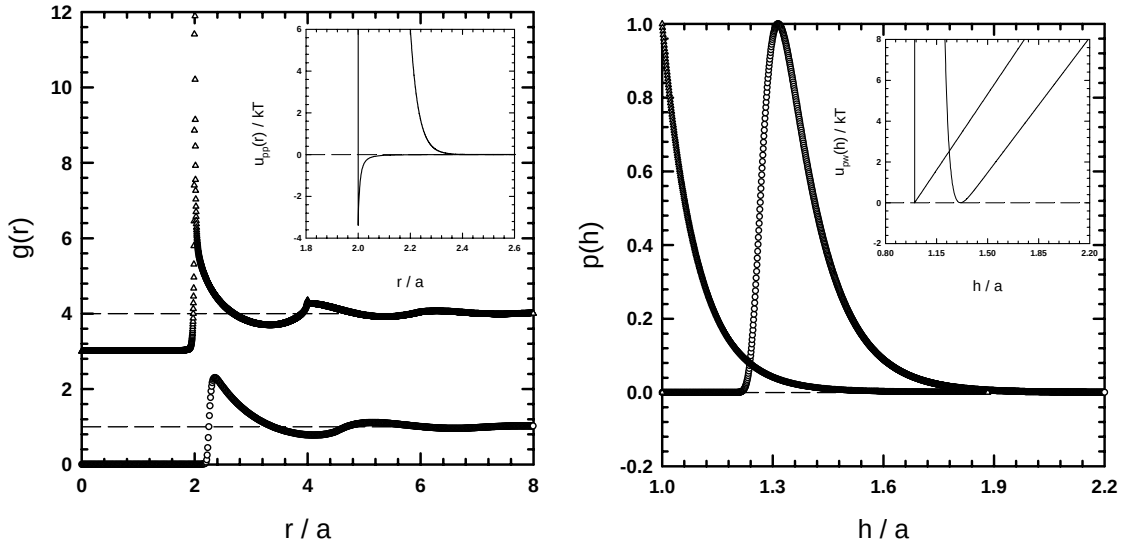

(a) (b)

Figure 6.1. Particle-particle pair interaction potential (inset) and pair correlation function (main) for repulsive electrostatic (O) and attractive van der Waals (Δ) potentials. (b) Particle-wall interaction potentials (inset) and probability distribution functions for electrostatic (O) and hard wall (Δ) potentials.

Equilibrium NVT Monte Carlo (MC) simulations were performed for systems I and II with N_p=36 and N_p=46 respectively with particles interacting via potentials described earlier. Simulations were performed for about 10^6 steps after an initial equilibration period. Two-dimensional pair correlation functions were calculated using particle configurations and normalized by the average particle density. Fig. 6.1a shows two-dimensional radial distribution functions calculated using particle coordinates in dimensions lateral to the wall for system I (circles) and system II (triangles) plotted as a function of center-center separation normalized by the particle radius. The plot for

system II has been offset for clarity. The pair correlation function shows no particle overlaps, and at large particle-particle separations, the normalized radial distribution function decays to 1, implying that the particles are effectively restricted to only small normal displacements and can be effectively treated as a two-dimensional fluid for thermodynamic calculations at these conditions. This is also evident from the height distribution functions (Fig. 6.1b).

The dynamics of colloidal fluids can be measured by a plot of the average mean-squared displacement (MSD) as a function of time. MSDs are reported for displacements in both lateral and normal directions. We used Stokesian Dynamics (SD) simulations to obtain trajectories for particles interacting via potentials described earlier. Configurations from equilibrium MC simulations we used as the starting point for SD runs. The simulations were run for N_p=36 (system I) and N_p=46 (system II) particles. For calculating the hydrodynamic resistance tensor, the wall is discretized into an array of touching particles, having the same size as the diffusing particles. The number of wall particles for systems I and II are N_w=81 and N_w=64 respectively. The Stokesian Dynamics (SD) simulations were performed for both systems using the method described in the theory section. MSDs were calculated as averages over all the free particles (N_p), and over multiple time origins to reduce statistical noise. Care was taken to equally weigh displacements for all time steps from all time origins.

Fig. 6.2 shows particle MSDs for systems I (circles) and II (triangles) with time. The points are calculated as the sum of MSD values in the two lateral directions. MSDs are normalized by a^2 and time is normalized by the diffusive time scale, $\tau = a^2/D_0$. The

MSD data shows the typical behavior for Brownian particles diffusing in a viscous medium. At short times, ($t << \tau$), the particles diffuse over distances much smaller than the particle size and thus do not perturb the equilibrium structure. The MSD in this region varies linearly with time, with a slope equal to $4D_{S,||}^{S}$, where $D_{S,||}^{S}$ is the short-time self diffusion coefficient parallel to the wall. The short-time diffusion corresponds to localized displacements much smaller than the particle size, the particle configuration is largely unchanged, and hence, for a given particle size and solvent viscosity, only depends on the equilibrium configuration.[98] Thus, it can be calculated from particle coordinates generated using MC simulations. The dashed lines in Fig. 6.2, which coincide with the MSD points at short times ($t \rightarrow 0$) are $4D_{S,||}^{S}t$, where $D_{S,||}^{S}$, is calculated from the hydrodynamic resistance tensor constructed using MC particle coordinates. Fig. 6.2b shows the MSD curve at short times where the agreement between the two curves is clearly seen. For comparison, single-particle lateral diffusion coefficients are represented by solid lines for the two systems.

The single-particle lateral diffusion coefficient predictions are shown by the solid lines in Fig. 6.2. It can be seen that the single particle and the multi-particle short time diffusivities are almost equal for the electrostatic system. The hydrodynamic interactions of the particles are small due to the relatively large interparticle surface separation. The total hydrodynamic resistance is thus dominated by the wall, resulting in the single-particle and the dispersion diffusion coefficients being very close to each other. In contrast, there is considerable difference between the single particle and the multi-particle short time diffusion coefficients for the attractive system, where the higher

particle density and attractive potential result in small particle-particle separations.

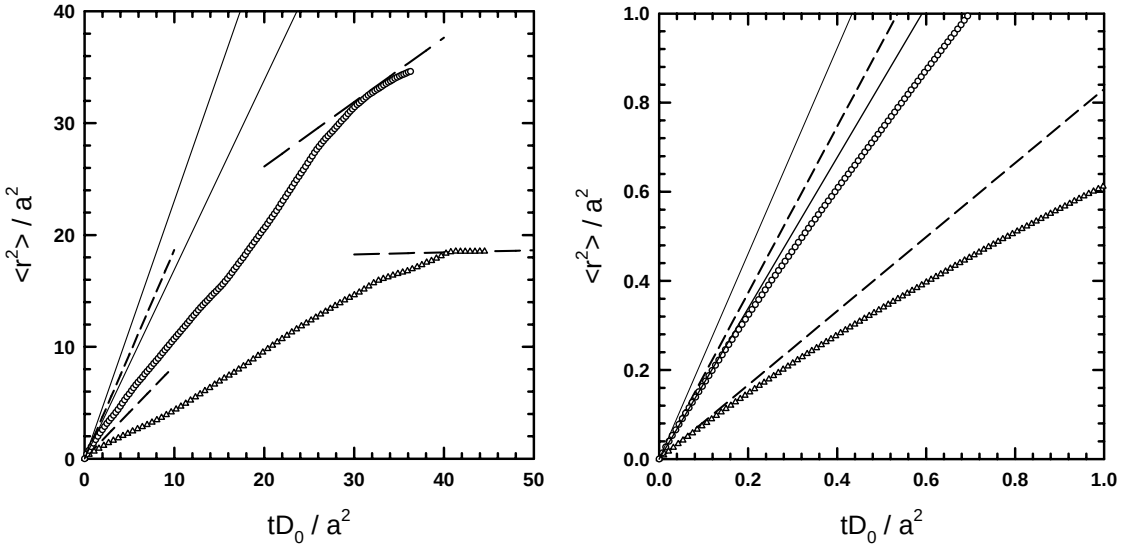

(a) (b)

Figure 6.2. (a) Lateral mean squared displacements from Stokesian Dynamic simulations of interfacial colloidal fluids with repulsive electrostatic (O) and attractive van der Waals (Δ) potentials shown in fig. 6.1a. Short and long time diffusive limits computed from Monte Carlo simulated particle coordinates (- -) using eqs. (6.18) and (6.19). Height averaged single particle lateral diffusion coefficients (—) computed using eq. (6.13). (b) Enlarged view of same curves reported in (a) to show the short time regime.

At times $t > \tau$, the particle diffuses over a distance larger than its radius, and starts to encounter other particles in the dispersion. In this intermediate regime, where the probe particle encounters the equilibrium structure, rearrangements must occur within the equilibrium structure for the particle to move past its neighbors. The MSD is non-linear with time, and hence the particle is non-diffusive in this regime. Beyond this, at $t >> \tau$, after the particle has diffused a considerable distance and sampled the

equilibrium structure, the MSD is again linear with time, with a slope equal to $4D_S^L$, where D_S^L is the long-time self diffusion coefficient, D_S^L. Diffusion coefficients are also calculated from MC particle configurations using equations (6.18) and (6.19). Dashed lines in fig. 6.2 coinciding with the MSD curve at long times are calculated values of $4D_S^L$t, with D_S^L calculated from MC particle configurations. The MC calculated diffusion coefficients show excellent agreement with the actual dynamics, thereby enabling us to use equilibrium MC simulations to predict diffusion coefficients of interfacial fluids.

Fig. 6.3 shows average particle MSDs normal to the surface as a function of time. Normal diffusion is different from lateral diffusion since the particles are confined within a potential well in the normal direction. At short times ($t << \tau$), the particle dynamics is similar to lateral diffusion, where the slope of the MSD is proportional to the average normal short-time self-diffusion coefficient, $D_{S,\perp}^S$. $D_{S,\perp}^S$ calculated from MC particle configurations using Eq. (6.18) is used to plot the dashed lines, which are equal to $2D_{S,\perp}^S t$. The short-time limit is magnified in fig. 6.3b. Again, the agreement between diffusion coefficients calculated from MC and SD particle configurations is excellent. For comparison, we also plot the infinite dilution limit (including the effect of single particle wall hydrodynamic interactions),

The long-time dynamics ($t >> \tau$) is different in the normal direction when compared to the lateral direction. At long times, the particle cannot diffuse beyond a certain value in the z-direction due to confinement induced by the wall and gravity. This

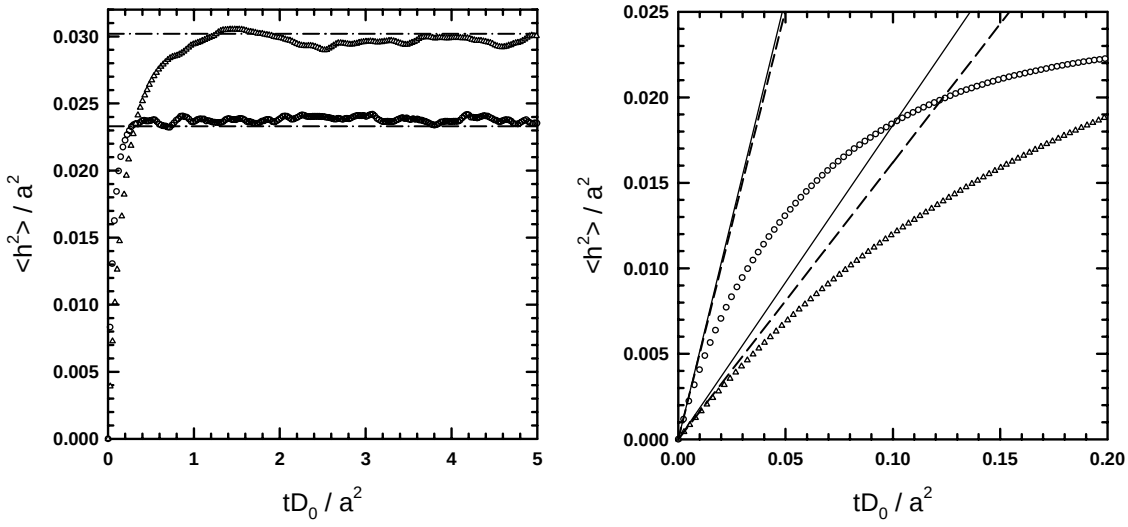

(a) (b)

Figure 6.3. (a) Mean squared displacements in the *z*-direction from Stokesian Dynamic simulations of interfacial colloidal fluids with repulsive electrostatic (O) and attractive van der Waals (Δ) potentials. Long time diffusive plateaus (— ·) computed using eq. (6.15). (b) Enlarged view of same curves reported in (a) to show the short time regime. Short time diffusive limits computed from Monte Carlo simulated particle coordinates (- -) using eq. (6.18). Height averaged single particle normal diffusion coefficients (—) computed using eq. (6.13).

long-time limit for a single particle diffusing in a potential well can be calculated using eq. (6.15). These limits are plotted in fig. 6.3a as shown by the dot-dashed lines. The long time limit of MSD for the two systems calculated from dynamic simulations agrees with the calculated limits, implying that the single-particle approximation is sufficient to capture the long-time diffusive limit in the normal direction.

Another characteristic quantity to study dynamics in the normal direction is the height autocorrelation function.[55] This has been calculated and experimentally

determined for the case of a single particle near an interface[55]. In this study, we apply the analysis to a colloidal fluid next to an interface. The position autocorrelation function describes in an average sense, how the height of a particle at two different times is correlated. The rate at which this correlation decays is a measure of the diffusion coefficient, and is equal to the ensemble averaged normal diffusion coefficient. At t=0, the particle heights are totally correlated, and the autocorrelation function, in a normalized sense is unity. At short times, the particles start loosing correlation, and hence the autocorrelation function starts to decay. At sufficiently long times, the particle looses its correlation completely. Fig. 6.4 shows height autocorrelation functions averaged over all particles and over multiple time origins, paralleling the MSD analysis.

The dashed lines are calculated using average normal diffusion coefficients from MC particle coordinates (eq. (6.18)). For comparison, average normal diffusion coefficients for single particles next to a wall (infinite dilution), calculated using eq.. (6.13) are plotted as solid lines. Again, the single-particle and the true multi-particle short time self diffusion coefficients are almost similar for the electrostatic system, but noticeably different for the attractive particles. This is a result of the interparticle spacing being smaller in the attractive system as compared to the electrostatic system. The short-time limit is magnified in fig. 6.4b, where the agreement between the MC and SD diffusion coefficients can be seen more clearly. This agreement shows that the single-particle result can be extended without loss of generality to multi-particle systems, with the single-particle normal diffusion coefficient being replaced by the ensemble averaged normal self-diffusion coefficient.

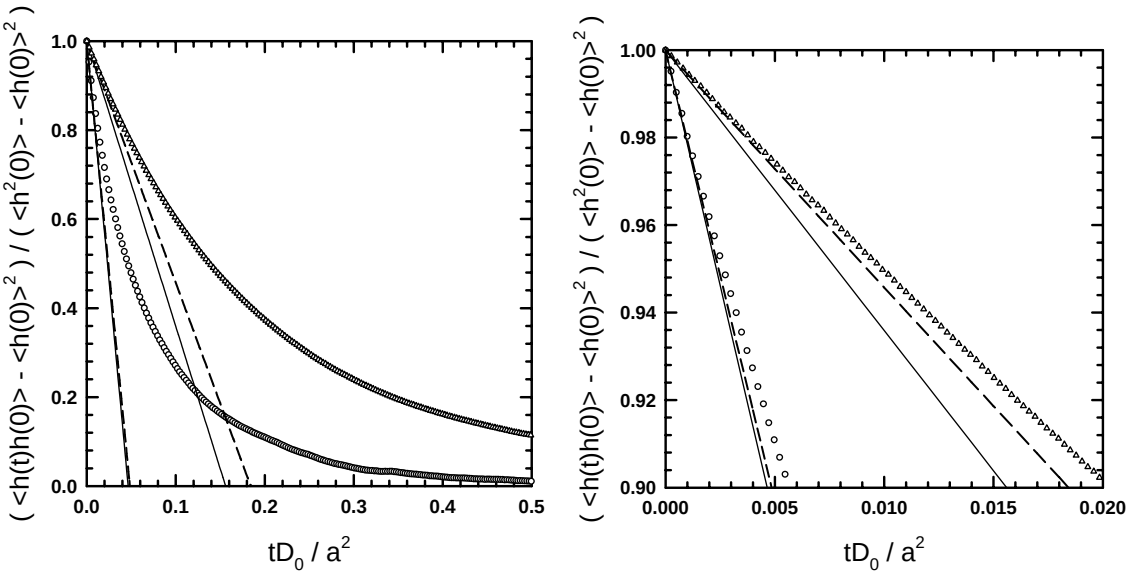

Figure 6.4. (a) Normalized height autocorrelation functions from Stokesian Dynamic simulations of interfacial colloidal fluids with repulsive electrostatic (O) and attractive van der Waals (Δ) potentials. Short time diffusive limits computed from Monte Carlo simulated particle coordinates (- -) using eq. (6.18). Height averaged single particle normal diffusion coefficients (—) computed using eq. (6.13). (b) Enlarged view of same curves reported in (a) to show the short time regime.

Our results demonstrate the validity of expressions for calculating particle diffusion coefficients using expressions discussed earlier. Particle trajectories obtained in experiments can be used to calculate MSDs, from which diffusion coefficients can be obtained. Alternatively, equilibrium particle coordinates can be used to construct the hydrodynamic resistance tensor, from which average diffusivities can be computed. The autocorrelation function and the MSD in the normal direction are more sensitive to the time interval between two consecutive particle configurations. The short-time self-diffusion coefficient also has a strong system size dependency,[90,98] the effect of which is

avoided in this work by selecting equal system sizes for both MC and SD simulations. For bulk (three-dimensional) dispersions, a correction for system-size has been developed,[90] but the same is not applicable for interfacial fluids. The effect of system size can be minimized by having a fairly large number of particles (>100).

6.7. Conclusions

In this work, we have used Stokesian Dynamic simulations to analyze dynamics of colloidal fluids near a solid interface. We have studied two systems, one with particles interacting via a screened repulsive potential and another where particles interact via an attractive van der Waals well. We also calculate average lateral and normal particle diffusion coefficients, both from rigorous Stokesian Dynamic as well as equilibrium Monte Carlo simulations. The short-time self-diffusion coefficient was predicted from equilibrium MC particle configurations and shown to agree with the short-time slope of the mean-squared displacement curve, as calculated from SD particle trajectories. The long-time diffusion coefficient was determined using an expression which combined the short-time self diffusion coefficient with a thermo dynamic term, both calculated from MC particle coordinates. The predicted long-time self-diffusion coefficient was shown to match the long-time slope of the mean-squared displacement curve. This implies that average particle diffusion coefficients for equilibrium fluids can be calculated using equilibrium particle coordinates, without resorting to expensive dynamic simulations. The single-particle (infinite dilution) diffusion coefficients are also compared to the calculated dispersion diffusion coefficients. From results on the

electrostatic system, it can be concluded that the presence of many particles affect the lateral diffusion coefficient more than the normal diffusion coefficient. However, for attractive particles, the dispersion diffusion coefficients are considerably smaller than the single-particle diffusion coefficients. Height autocorrelation functions and mean-squared displacements in the normal direction were used to quantify the dynamics in the normal direction. Diffusion coefficients calculated from MC particle coordinates agree with both the mean-squared displacement and the autocorrelation function results.

While the simulation methods and analyses we have used are well-established in literature, a systematic study of particle diffusion near an interface using rigorous dynamic simulations has not been undertaken. An approximate hydrodynamic treatment of the wall might give reasonable estimates of particle diffusivities, concentrated dispersions or dispersions with attractive particles warrants the use of an exhaustive treatment of the wall-induced hydrodynamic interactions. To the authors' knowledge this is the first work where mean-squared displacements of an interfacial fluid have been compared to short and long time self-diffusion coefficients calculated from equilibrium particle coordinates. This work will be used for analyzing dynamics of interfacial colloidal fluids, which is crucial for template-directed colloidal crystallization. The simulations establish a solid test case for testing the analyses, which can now be directly applied to real experiments. Several experimental observations in interfacial colloidal fluids are due to complex multi-body hydrodynamic forces, which can be accurately described by using the tools presented in this work.

7. CONCLUSIONS

7.1. Summary of Conclusions

Understanding the effect of particle-particle and particle-wall potentials on the dynamics of colloidal dispersions is important for several applications ranging from particle depositions in coatings such as inks and paints to growing colloidal crystals on patterned substrates for creating photonic bandgap materials. This dissertation describes the use of Monte Carlo and Stokesian Dynamic simulations to model colloidal dispersions and the development of theoretical expressions, to quantify and predict dynamics of the system. The emphasis is on accurately incorporating conservative, Brownian, and hydrodynamic forces to capture the dynamic behavior of a colloidal dispersion. In particular, the long-range multi-body hydrodynamic forces are accurately modeled using Stokesian Dynamics. The conservative potentials were obtained from direct measurements using Total Internal Reflection Microscopy (TIRM), or from rigorous theoretical predictions. This accurate treatment of the forces at the microscale can yield accurate estimates of the dynamics of both single particles and ensembles of particles.

The initial effort of this dissertation was in applying Stoesian Dynamics to small, finite systems to test its predictive capabilities. The perfect test problem for this was the somewhat controversial set of experiments[29,30] in which anomalous attraction was measured between two like-charged particles near one or two like-charged surface(s). Although previous a simulation study[31] using Brownian dynamics had shown that the

experimental observation was due to the influence of the wall, there was a lack of complete quantitative agreement between simulation and experiment, which can be attributed to the approximate treatment of hydrodynamic interactions. This presented a perfect opportunity to test the predictive capabilities of Stokesian Dynamics. Our results demonstrated that complete quantitative agreement could be realized by capturing the hydrodynamic interactions accurately. In addition, we demonstrated that a purely hydrodynamic contribution from the wall was sufficient to induce an apparent anomalous attraction between the particles. We also showed the importance of statistics while calculating potentials from distribution functions. These simulations emphasize the utility of simulations in aiding the interpretation of experimental data.[100]

To extend simulation from an interpretive to a predictive tool, we used Stokesian Dynamics to explore the equilibrium percolation threshold in attractive colloidal fluids.[101] In order to realize the dream of robust colloidal crystals, there needs to be an attractive force to hold the particles together, similar to atomic and molecular crystals. The thermodynamic phase diagram for attractive colloids shows a small region for the solid (crystal) phase and a remaining fluid phase. The vast majority of the phase diagram is a fluid phase with smoothly varying thermodynamic functions. Kinetically irreversible structures such as gels and glasses can be observed at large attraction and high concentration.

In the equilibrium fluid phase, however, there is a single region, where the particles undergo a structural transition. This region corresponds to the percolation transition and is important as being the only identifiable feature in the equilibrium fluid

phase. Using a combination of Monte Carlo and Stokesian Dynamics, we showed that the percolation threshold corresponds to a dynamic transition involving a sharp change in the short time self-diffusion coefficient. This result gives a physical picture of the percolation threshold since the short time self-diffusion coefficient is related to viscoelastic properties, while providing an unambiguous criterion to identify the percolation threshold. This approach is being extended to analyzing electrostatic crystals (see Section 8).

Finally, one of the requirements of experiments involving colloidal fluids near an interface is the ability to quantify the dynamics, primarily self-diffusion. While there are well-established theoretical and simulation methods for measuring the short and long time self-diffusive limits for a colloidal fluid in the bulk, these have not been extended to interfacial colloidal fluids. Since most important involving colloidal fluids, including colloidal deposition on patterned substrates require an underlying substrate, it becomes important to be able to quantify diffusion in these systems. For this reason, we extend theoretical expressions for self-diffusion in three dimensions to interfacial colloidal fluids, and verify their validity for use in these systems.[102] We also compare self-diffusion coefficients calculated from equilibrium configurations and dynamics trajectories and show their excellent agreement.

To finally summarize, Monte Carlo and Stokesian Dynamic simulations, along with analytical theory have been used to model dynamics of colloidal dispersions under different conditions. We have demonstrated both the interpretive and predictive capabilities of Stokesian Dynamics, along with the importance of multi-body

hydrodynamic interactions in colloidal dispersions.

8. FUTURE RESEARCH

8.1. Synopsis

This section briefly summarizes current and future work which has not been presented in this dissertation. The ideas discussed below are closely related to Sections 4-6 and are in tune with the general theme of using simulations for predicting dynamic properties of colloidal dispersions.

8.2. Self-Diffusion on Patterned Substrates

Understanding lateral diffusion of colloids near a patterned surface is important for template-directed colloidal assembly. The "pattern" may be physical or chemical in nature. The key physics here is how the particle-particle and varying particle-wall interaction affects the lateral self-diffusion of the colloidal dispersion. Thermodynamically, the pattern introduces the dispersion to a free energy landscape, which creates density gradients in the lateral direction. This affects the short-time and long-time self-diffusion coefficients of the dispersion. Some of the ongoing work in this area is to develop generalized expressions for predicting self-diffusion coefficients on patterned substrates. We are also using Stokesian Dynamics to simulate particles diffusing over a patterned substrate. These tools should enable us to explain observations made in experiments.

Fig. 8.1a shows an example of silica colloids diffusing over a glass surface with gold patterns.[103] Fig. 8.1b shows average mean-squared displacements (MSDs) for

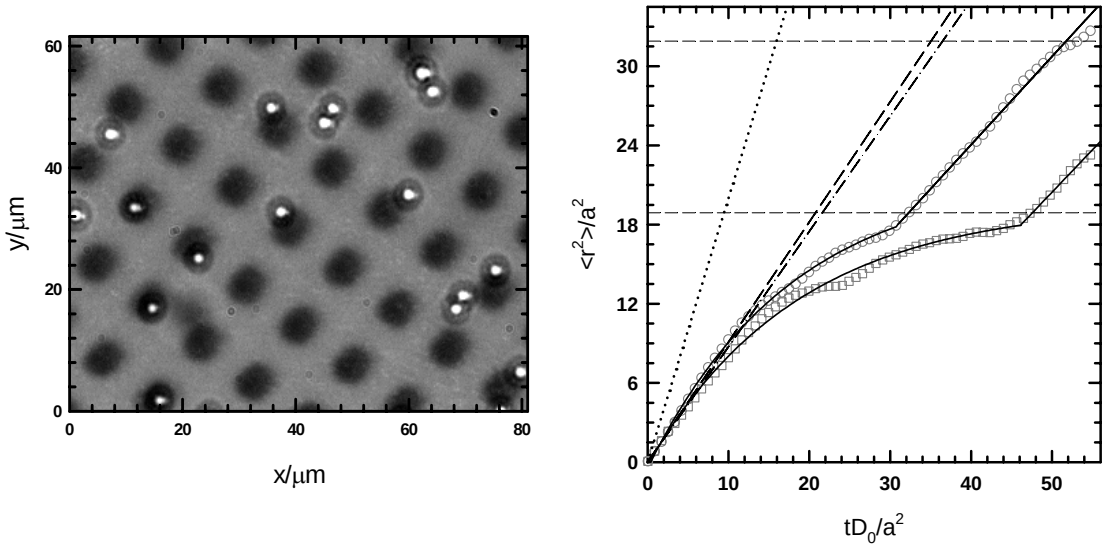

(a) (b)

Figure 8.1.[103] (a) Transmitted light CCD image of 2.34 μm silica colloids electrostatically levitated in aqueous 1mM KNO_3/HNO_3 above 5 μm × 5 μm × 15 nm (*l* × *w* × *h*) Au square films separated by 6 μm regions with 5 nm Au films (all on glass substrates). 15 nm Au films appear darker than 5 nm Au films. (b) Lateral mean squared displacements in *x*(o) and *y*(□) directions. Reference lines are shown for bulk diffusion (···) and lateral surface diffusion on 5 nm (--) and 15 nm (- · -). Solid lines (—) are theoretical fits.[104]

particles in fig. 8.1a. The MSD dramatically shows the effect of the pattern. The plateau seen in the curve is due to the particles being attracted to the small patterns. The MSD data has been fit with an expression for diffusion in a confined area.[104] We are in the process of trying to gain a fundamental understanding of this diffusive process. It is useful to be able to quantify how the pattern influences the short- and long-time diffusion coefficients. This finds direct application in realizing a kinetic pathway for template-directed colloidal assembly.

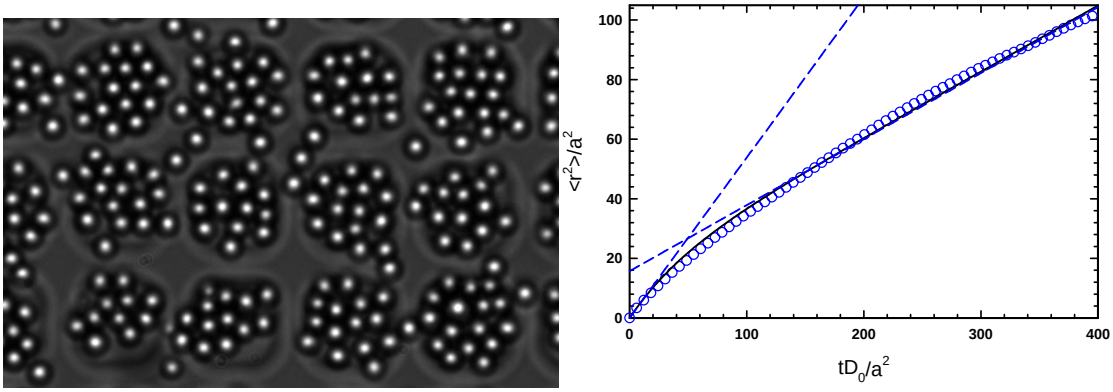

(a) (b)

Figure 8.2.[105] (a) Transmitted light CCD image of 2.20μm silica colloids above 13μm × 13μm × 800nm (*l* × *w* × *h*) features separated by 4μm. (b) Average Lateral mean squared displacements (□). Dashed lines show short- and long-time diffusive limits. Solid lines (—) are theoretical curve fits.[104]

Fig. 8.2a[105] shows an another example of silica 2.20μm colloids diffusing over a glass substrate with 13μm × 13μm × 800nm physical features, with the corresponding particle mean-squared displacement plotted in Fig. 8.2b. The dispersion in this experiment has a higher density than in Fig. 8.1a, giving rise to more complex thermodynamic behavior. The system behaves as an inhomogeneous fluid modulated by the underlying potential energy landscape. To quantify the long-time dynamics, we would need to incorporate the observed density partitioning into the expression for the long-time self-diffusion coefficient. The inhomogeneity of the surface is reflected in the long-time diffusive limit shown in the MSD plot in Fig. 8.2b. Stokesian Dynamics can be used to generate test data for analyzing diffusivities. The high-density problem is unavoidable since the solid (crystal) phase is at the highest density possible.

8.3. Percolation in Interfacial Attractive Colloidal Fluids

It has earlier been shown (Section 5, Anekal et al.[101]) that the equilibrium percolation threshold in attractive colloidal fluids is associated with a dynamic transition corresponding to a sharp change in the short-time self-diffusion coefficient. Since the same percolation phenomenon also exists in two-dimensional fluids, it is tempting to try to extend this concept to an interfacial colloidal fluid. The motivation is similar to the three dimensional case in that, the percolation threshold is a rare structural feature in the fluid phase. Two-dimensional percolation is important to interfacial rheological properties, phase separation kinetics, and self-assembly processes in interfacial colloidal dispersions. Two-dimensional percolation is also important to making conducting films using colloidal precursors. Percolation in attractive 2D fluids is very poorly understood when compared to the vast body of literature in 3D percolation. We are studying percolation in interfacial colloidal fluids by calculating lateral diffusion coefficients of particles confined between two walls, which is thermodynamically equivalent to a two-dimensional fluid. Changing the amount of attraction changes the two-dimensional configuration, which changes the short-time self-diffusion coefficient of the fluid. We are currently investigating if this change across the percolation threshold is consistent with what is seen in the bulk dispersion.

8.4. Self-Diffusion in Shrinking Electrostatic Colloidal Crystals

Unlike hard-sphere or attractive colloidal crystals, large, single-domain electrostatic colloidal crystals form quite effortlessly. One of the main reasons for this is

the large spacing between particles in an electrostatic crystal, which allows them to diffuse and form ordered structures. By adding small amounts of salt to an electrostatically stabilized crystal, it is possible to shrink the crystal by decreasing the Debye length. However, attempting to shrink the ordered structure beyond a certain limit, results in the formation of a gel.

The difference between electrostatic, hard-sphere, and attractive systems can be expressed by the ratio of the thermodynamic size to the hydrodynamic size, $\xi = a_T / a_H$. The thermodynamic size can be thought of as half the separation of the first peak in the particle pair correlation function. The hydrodynamic size is half the separation where the particle-particle lubrication force becomes singular, which is merely equal to the actual particle radius. For electrostatic systems, the thermodynamic radius includes a part of the Debye screening length, and hence $\xi > 1$. For hard-spheres, $\xi = 1$, and for attractive systems, $\xi < 1$. The higher the ratio, the more ease with which crystals can form. In a shrinking electrostatic crystal, the different equilibrium states are all solid (crystal) phases, and all these states have the same osmotic pressure. That is, $\Pi(\phi, \kappa)$ is a constant, where Π is the osmotic pressure, ϕ is the particle concentration, and κ is the Debye length.

We are currently calculating the effective size ratios and self-diffusion coefficients as a function of ϕ and κ along the path where $\Pi(\phi, \kappa)$ is a constant, to mimic the equilibrium stages of a shrinking electrostatic crystal experiment to quantify when a shrinking electrostatic crystal begins to loose order. This approach is similar to the

consistent treatment of thermodynamics and hydrodynamics in our analysis of percolation in attractive colloidal fluids. Crystallization is an important thermodynamic transition, and its kinetics is important for self-assembly processes. This method can also be directly compared to published results on shrinking electrostatic crystals.[57]

REFERENCES

[1]Y. A. Vlasov, X. Z. Bo, J. C. Sturm, and D. J. Norris, Nature **414** (6861), 289 (2001).

[2]J. F. Brady and G. Bossis, Annu. Rev. Fluid Mech. **20**, 111 (1988).

[3]A. Einstein, Ann. Phys. **17**, 549 (1905).

[4]M. V. Smoluchowski, Ann. Phys. **48**, 1103 (1915).

[5]M. V. Smoluchowski, Ann. Phys. **21**, 756 (1966).

[6]P. Langevin, C. Acad. Sci. **146**, 530 (1908).

[7]A. D. Fokker, Ann. Phys.-Berlin **43** (5), 810 (1914).

[8]A. D. Fokker, Phys. Z. **15**, 96 (1914).

[9]M. Planck, Sitzungsber. Preuss. Akad. Wiss. Phys. Math. K1. **23**, 234 (1917).

[10]D. L. Ermak and J. A. Mccammon, J. Chem. Phys. **69** (4), 1352 (1978).

[11]C. W. Oseen, *Neuere Methoden und Ergebnisse in der Hydrodynamik* (Akademische Verlagsgesellschaft, Leipzig, 1927).

[12]J. Rotne and S. Prager, J. Chem. Phys. **50** (11), 4831 (1969).

[13]G. C. Ansell and E. Dickinson, J. Colloid Interf. Sci. **110** (1), 73 (1986).

[14]G. C. Ansell and E. Dickinson, Faraday Discuss. **83**, 167 (1987).

[15]G. C. Ansell, E. Dickinson, and M. Ludvigsen, J. Chem. Soc. Farad. T. 2 **81** (AUG), 1269 (1985).

[16]J. Bacon, E. Dickinson, R. Parker, N. Anastasiou, and M. Lal, J. Chem. Soc. Farad. T. 2 **79**, 91 (1983).

[17]E. Dickinson, S. A. Allison, and J. A. Mccammon, J. Chem. Soc. Farad. T. 2 **81** (APR), 591 (1985).

[18]G. Bossis and J. F. Brady, J. Chem. Phys. **80** (10), 5141 (1984).

[19]L. Durlofsky, J. F. Brady, and G. Bossis, J. Fluid Mech. **180**, 21 (1987).

[20]J. F. Brady, R. J. Phillips, J. C. Lester, and G. Bossis, J. Fluid Mech. **195**, 257 (1988).

[21]C. W. J. Beenakker, J. Chem. Phys. **85** (3), 1581 (1986).

[22]G. Bossis, A. Meunier, and J. D. Sherwood, Phys. Fluids A **3** (8), 1853 (1991).

[23]J. R. Blake, Proc. Camb. Philos. S-M **70** (SEP), 303 (1971).

[24]P. R. Nott and J. F. Brady, J. Fluid Mech. **275**, 157 (1994).

[25]A. Singh and P. R. Nott, J. Fluid Mech. **412**, 279 (2000).

[26]G. Bossis and J. F. Brady, J. Chem. Phys. **87** (9), 5437 (1987).

[27]J. F. Brady, J. Fluid Mech. **272**, 109 (1994).

[28]M. Medina-Noyola, Phys. Rev. Lett. **60** (26), 2705 (1988).

[29]A. E. Larsen and D. G. Grier, Nature **385** (6613), 230 (1997).

[30]J. C. Crocker and D. G. Grier, Phys. Rev. Lett. **77** (9), 1897 (1996).

[31]T. M. Squires and M. P. Brenner, Phys. Rev. Lett. **85** (23), 4976 (2000).

[32]A. T. J. M. Woutersen, J. Mellema, C. Blom, and C. G. Dekruif, J. Chem. Phys. **101** (1), 542 (1994).

[33]J. Happel and H. Brenner, *Low Reynolds Number Hydrodynamics* (Prentice-Hall, Englewood Cliffs, NJ, 1965).

[34]W. B. Russel, D. A. Saville, and W. R. Schowalter, *Colloidal Dispersions* (Cambridge University Press, New York, 1989).

[35]H. Lamb, *Hydrodynamics* (Cambridge University Press, Cambridge, 1932).

[36]O. A. Ladyzhenskaya, *The Mathematical Theory of Viscous Incompressible Flow*, 2nd ed (Gordon and Breach, New York, 1969).

[37]L. G. Leal, *Laminar Flow and Convective Transport Processes* (Butterworth-Heinemann, Newton, MA, 1992).

[38]C. Pozrikidis, *Boundary Integral and Singularity Methods for Linearized Viscous Flow* (Cambridge University Press, Cambridge, 1992).

[39]D. J. Jeffrey and Y. Onishi, J. Fluid Mech. **139** (FEB), 261 (1984).

[40]G. K. Batchelor, J. Fluid Mech. **74** (MAR9), 1 (1976).

[41]H. Brenner, Chem. Eng. Sci. **16** (3-4), 242 (1961).

[42]R. Pesche and G. Nagele, Phys. Rev. E **62** (4), 5432 (2000).

[43]T. N. Phung, J. F. Brady, and G. Bossis, J. Fluid Mech. **313**, 181 (1996).

[44]M. A. Bevan and D. C. Prieve, Langmuir **15** (23), 7925 (1999).

[45]A. J. Banchio and J. F. Brady, J. Chem. Phys. **118** (22), 10323 (2003).

[46]M. Fixman, J. Chem. Phys. **69** (4), 1527 (1978).

[47]P. S. Grassia, E. J. Hinch, and L. C. Nitsche, J. Fluid Mech. **282**, 373 (1995).

[48]M. P. Allen and D. J. Tildesley, *Computer Simulation of Liquids* (Oxford Science, New York, 1987).

[49]W. H. Press, B. P. Flannery, S. A. Teukolsky, and W. T. Vetterling, *Numerical Recipes in Fortran: The Art of Scientific Computing*, 2nd ed (Cambridge University Press, New York, 1992).

[50]A. E. Larsen and D. G. Grier, Nature **385**, 230 (1997).

[51]E. J. W. Verwey and J. T. G. Overbeek, *Theory of the Stability of Lyophobic Colloids* (Elsevier, Amsterdam, 1948).

[52]J. C. Crocker and D. G. Grier, Phys. Rev. Lett. **73** (2), 352 (1994).

[53]T. M. Squires, J. Fluid Mech. **443**, 403 (2001).

[54]D. C. Prieve, Adv. Colloid Interfac. **82** (1-3), 93 (1999).

[55]M. A. Bevan and D. C. Prieve, J. Chem. Phys. **113** (3), 1228 (2000).

[56]H. J. Wu and M. A. Bevan, Langmuir **21** (4), 1244 (2005).

[57]M. A. Bevan, J. A. Lewis, P. V. Braun, and P. Wiltzius, Langmuir **20** (17), 7045 (2004).

[58]A. van Blaaderen, R. Ruel, and P. Wiltzius, Nature **385** (23), 321 (1997).

[59]W. Lee, A. Chan, M. A. Bevan, J. A. Lewis, and P. V. Braun, Langmuir **20** (13), 5262 (2004).

[60]A. F. Routh and W. B. Russel, Langmuir **15**, 7762 (1999).

[61]N. Ise, T. Okubo, M. Sugimura, K. Ito, and H. N. Nolte, J. Chem. Phys. **78** (1), 536 (1983).

[62]G. M. Kepler and S. Farden, Phys. Rev. Lett. **73** (2), 356 (1994).

[63]Y. Han and D. G. Grier, Phys. Rev. Lett. **91** (3), 038302 (2003).

[64]R. Klein, H. H. von Grunberg, C. Bechinger, M. Brunner, and V. Lobaskin, J. Phys.-Condens. Mat. **14** (33), 7631 (2002).

[65]C. P. Royall, M. E. Leunissen, and A. van Blaaderen, J. Phys.-Condens. Mat. **15** (48), S3581 (2003).

[66]T. J. Murphy and J. L. Aguirre, J. Chem. Phys. **57** (5), 2098 (1972).

[67]J. M. Sancho, M. S. Miguel, and D. Durr, J. Stat. Phys. **28** (2), 291 (1982).

[68]S. H. Behrens, J. Plewa, and D. G. Grier, Eur. Phys. J. E **10**, 115 (2003).

[69]M. A. Bevan, Ph.D. Dissertation, Carnegie Mellon University, 1999.

[70]D. S. Sholl, M. K. Fenwick, E. Atman, and D. C. Prieve, J. Chem. Phys. **113** (20) (2000).

[71]J. C. Crocker and D. G. Grier, J. Colloid Interf. Sci. **179** (1), 298 (1996).

[72]J. M. Sancho, M. S. Miguel, and D. Durr, Journal of Statistical Physics **28** (2), 291 (1982).

[73]D. A. McQuarrie, *Statistical Mechanics* (University Science Books, Sausalito, CA, 1976).

[74]D. L. Ermak and J. A. McCammon, J. Chem. Phys. **69** (4), 1352 (1978).

[75]E. R. Dufresne, T. M. Squires, M. P. Brenner, and D. G. Grier, Phys. Rev. Lett. **85**, 3317 (2000).

[76]D. G. Grier, J. Phys.-Condens. Mat. **12** (8A), A85 (2000).

[77]L. Fabbian, W. Gotze, F. Sciortino, P. Tartaglia, and F. Thiery, Phys. Rev. E **59** (2), R1347 (1999).

[78]M. C. Grant and W. B. Russel, Phys. Rev. E **47** (4), 2606 (1993).

[79]C. J. Rueb and C. F. Zukoski, J. Rheol. **42** (6), 1451 (1998).

[80]S. A. Shah, Y. L. Chen, K. S. Schweizer, and C. F. Zukoski, J. Chem. Phys. **119** (16), 8747 (2003).

[81]J. F. Brady, J. Fluid Mech. **272**, 109 (1994).

[82]M. A. Bevan, S. N. Petris, and D. Y. C. Chan, Langmuir **18** (21), 7845 (2002).

[83]M. A. Bevan and D. C. Prieve, Langmuir **16** (24), 9274 (2000).

[84]D. W. Marr and A. P. Gast, J. Chem. Phys. **99** (3), 2024 (1993).

[85]S. B. Lee, J. Chem. Phys. **114** (5), 2304 (2001).

[86]Y. C. Chiew and E. D. Glandt, J. Phys. A **16**, 2599 (1983).

[87]N. F. Carnahan and K. E. Starling, J. Chem. Phys. **51** (2), 635 (1969).

[88]D. J. Jeffrey and Y. Onishi, J. Fluid Mech. **139** (FEB), 261 (1984).

[89]R. J. Phillips, J. F. Brady, and G. Bossis, Phys. Fluids **31** (12), 3462 (1988).

[90]A. J. C. Ladd, J. Chem. Phys. **93** (5), 3484 (1990).

[91]J. F. Brady, J. Chem. Phys. **98** (4), 3335 (1993).

[92]B. X. Cui, B. H. Lin, and S. A. Rice, J. Chem. Phys. **114** (20), 9142 (2001).

[93]A. H. Marcus, B. H. Lin, and S. A. Rice, Phys. Rev. E **53** (2), 1765 (1996).

[94]H. Diamant, B. Cui, B. Lin, and H. Diamant', J. Phys.-Condens. Mat. **17** (31), S2787 (2005).

[95]R. Pesche, M. Kollmann, and G. Nagele, J. Chem. Phys. **114** (19), 8701 (2001).

[96]A. J. Goldman, R. G. Cox, and H. Brenner, Chem. Eng. Sci. **21** (12), 1151 (1966).

[97]H. Brenner, Chem. Eng. Sci. **16** (3-4), 242 (1961).

[98]R. J. Phillips, J. F. Brady, and G. Bossis, Phys. Fluids **31** (12), 3462 (1988).

[99]S. B. Yuste and A. Santos, J. Stat. Phys. **72** (3-4), 703 (1993).

[100]S. G. Anekal and M. A. Bevan, J. Chem. Phys. **122** (3) (2005).

[101]S. G. Anekal, P. Bahukudumbi, and M. A. Bevan, Phys. Rev. E **73**, 020403 (2006).

[102]S. G. Anekal and M. A. Bevan, The Journal of Chemical Physics (Submitted) (2006).

[103]H.-J. Wu, W. N. Everett, S. G. Anekal, and M. A. Bevan, Langmuir (Submitted) (2006).

[104]A. Kusumi, Y. Sako, and M. Yamamoto, Biophys. J. **65** (5), 2021 (1993).

[105]P. Bahukudumbi and M. A. Bevan, (In preparation) (2006).

VITA

Samartha Guha Anekal received his Bachelor of Engineering degree in chemical engineering from the National Institute of Technology, Karnataka, India (formerly Karnataka Regional Engineering College, affiliated to Mangalore University). He entered the doctoral program in chemical engineering at Texas A&M University in August 2001. His research interests are in the field of dynamics of colloidal fluids.

Mr. Anekal may be reached at Department of Chemical Engineering (c/o Dr. Michael Bevan), Texas A&M University, College Station, TX 77843-3122. His email address is sanekal@gmail.com.